Control and Simulation of Power Electronic Dominated Power Systems

Ciaran Roberts

Electrical Engineering and Computer Sciences
University of California, Berkeley

Technical Report No. UCB/EECS-2023-154
http://www2.eecs.berkeley.edu/Pubs/TechRpts/2023/EECS-2023-154.html

May 12, 2023

Control and Simulation of Power Electronic Dominated Power Systems

by

Ciaran Martin Roberts

A dissertation submitted in partial satisfaction of the

requirements for the degree of

Doctor of Philosophy

in

Engineering – Electrical Engineering and Computer Sciences

in the

Graduate Division

of the

University of California, Berkeley

Committee in charge:

Professor Duncan Callaway, Co-chair
Professor Seth Sanders, Co-chair
Professor Robert Pilawa-Podgurski
Professor Sairaj Dhople

Spring 2023

Control and Simulation of Power Electronic Dominated Power Systems

Abstract

Control and Simulation of Power Electronic Dominated Power Systems

by

Ciaran Martin Roberts

Doctor of Philosophy in Engineering – Electrical Engineering and Computer Sciences

University of California, Berkeley

Professor Duncan Callaway, Co-chair

Professor Seth Sanders, Co-chair

This dissertation is focused on how the integration of inverter-based resources into our power grids are forcing a re-examination of the fundamental principles upon which we operate and analyze these complex systems. Increased electrification and decarbonization of our energy sources are critical if we are to mitigate the impacts of climate change.

Chapter 1 presents a high-level overview of why inverter-based resources are such a transformative technology for large-scale power systems. We discuss how our current power system operational practices are designed around the inherent physical properties of synchronous machines and how we may need to re-visit some of these practices moving forward.

Chapter 2 considers a model of a battery energy storage system and tries to understand, for the voltage source inverter control scheme considered, the importance of modeling the DC side dynamics on the overall behavior of the inverter. We show that, for the controllers considered in this dissertation, we can model the DC side as a fixed voltage source without any loss in accuracy.

Chapter 3 examines how the cyber-physical attack surface of our power systems is changing with the inclusion of inverter-based resources. These dynamical devices perform active control across timescales with their multi-layered digital control loops, whose interaction through the network can result in unexpected system level dynamics. We consider the case of an adversary seeking to control a power electronic load to induce an instability in the system. We demonstrate how the outer-control loop and the phase-locked loop on inverter-based resources might be most vulnerable to attack and what, if any, signatures might appear at the system level during such an attack.

Chapter 4 considers how me might defend the system against the de-stabilizing attack considered in Chapter 3. We propose an adaptive controller that monitors the integrator state of the phase-locked loop for any abnormal sustained oscillatory behavior. In the event that this is present in the signal, we introduce a small amount of stochastic behavior into the control logic of the inverter to invalidate the model of the system that the adversary used in

controller design. We show the performance of the proposed controller through simulation on a small microgrid system.

Chapter 5 explores how we might proactively increase the damping ratio of underdamped system modes by using subspace identification to build a reduced-order model that captures the interaction between a local inverter-based resource and the external grid. We show that, by perturbing the reactive power channel of the inverter, we can build a reduced-order model that we can use for controller design to improve the dynamical response of the inverter. We compare the response of inverter-based resources with and without the proposed damping controller in simulation and show improved dynamical response following the tripping of a transmission line.

Chapter 6 moves from control to simulation of large-scale power electronic dominated power systems and explores how the growing field of scientific machine learning might offer opportunities to accelerate time-domain simulations of these systems. Due to the high control bandwidth of inverter-based resources, and their power rating relative to synchronous machines, the number of differential equations needed to analyze these systems is significantly increasing. We show how echo-state networks, trained at the same timestep as was used by an implicit adaptive ODE solver to solve the system, can rapidly, and accurately, predict the system response for parameters outside the training set. We discuss how this approach could be adapted by system operators today as well as some interesting future research directions.

Finally, this dissertation concludes with a brief summary and directions for future research.

To my parents, Margaret and Billy, whose support and sacrifices continue to amaze me.
And to my wife, Ramnique, the love of my life.

Contents

List of Figures

List of Tables

List of Acronyms

AL active load

AVR automatic voltage regulator

BESS battery energy storage system

CIG converter interfaced generation

CTESN continuous time echo-state network

DER distributed energy resources

ESN echo-state network

Gfl grid following

GFM grid forming

IBR inverter-based resource

LSTM long short-term memory

PINN physics informed neural network

PL passive load

PLL phase-locked loop

POD power oscillation damping

PSO particle swarm optimization

PSS power system stabilizer

PWM pulse-width modulation

RBF radial basis function

RHP right-half plane

RNN recurrent neural network

ROM reduced order model

SciML scientific machine learning

SID subspace identification

SISO single input single output

SG synchronous generator

SRF synchronous reference frame

SSO sub-synchronous oscillations

SVC singular value criterion

VSC voltage source converter

Acknowledgments

First, I'd like to thank my primary advisor, Professor Duncan Callaway. I first connected with Duncan when I was on a semester long exchange at UC Berkeley from University College Dublin as an undergraduate student. From our very first meeting, Duncan was eager to listen to, and encourage, my ideas. At the time, I had not considered pursuing a PhD. It was the experience of working within his research group that summer that sparked my passion for research and led me to where I am today. His consistent mentorship, advocating on my behalf, and unique ability to consider many angles to a research question I would pose, has been an invaluable asset to me throughout my research career so far.

I would also like to thank Professor Seth Sanders, whose class on power electronics equipped me a much deeper understanding of the unique capabilities of inverter-based resources and their impact on the power system. His willingness to meet with me to help advance my understanding, and participation on my dissertation committee, was invaluable. I would also like to thank Professor Sairaj Dhople and Professor Robert Pilawa-Podgurski for their insights and guidance as members of my dissertation committee. Additionally, I would like to thank Professor Federico Milano, who gave me an incredible education in power system modeling, stability and control during my time in University College Dublin. Our early conversations on the dynamics of inverter-dominated power systems would go on to shape my research directions and interests for years to come.

To the EECS support staff, particularly Shirley Salanio, who have been an invaluable resource in helping navigating this process. Their patience and care in answering all my questions and concerns was incredible. I want to thank all my colleagues in the power and energy on campus, Rodrigo Henriques-Auba, Jonny Lee, Keith Moffet, Laurel Dunn, Phillippe Phanivong, Jaimie Swartz, Mohini Bariya, Jose Daniel Lara, Ruth Kravis, Sunash Sharma, Gabriel Colon-Reyes and Kyle Brady. The conversations and random chats I've shared with you all have shaped my research and enriched my experience in the program in countless ways.

In addition to my advisors on campus, I was incredibly fortunate to be surrounded by some incredible researchers at Lawrence Berkeley National Laboratory (LBNL). A special thanks for Sila Kiliccote, Spyros Chatzivasileiadis, Daniel Olsen and Emre Can Kara who made my initial internship at LBNL such a intellectually, and professionally, enjoyable experience. To Emma Stewart who, as my supervisor, emboldened me to pursue my own research ideas and championed my career at every turn. To Sean Peisert, whose research philosophy has always been a source of inspiration for me. To Jason MacDonald, Migeul Helano, Gonçalo Cardoso, Doug Black, Sam Fernandes, Sy-Toan Ngo, from whom I have learned so much, both intellectually and professionally. To Professor Sascha von Meier and Professor Anna Scaglione, who as collaborators, went above and beyond to offer mentorship and intellectual insights into my research. Thanks to Joe Eto whom I have had the privilege to learn so much from. Joe's breadth of knowledge, and ability to distill the most complex of engineering ideas into core digestible concepts, has been one of the rarest skill sets I've witnessed. And finally, to Dan Arnold, who I first worked with all those years

ago during my semester exchange as an undergraduate. I have been incredibly lucky to work alongside such a supportive supervisor, incredible researcher and genuine friend. I will always treasure our many lunches in downtown Berkeley, our white board sessions working through proofs, and our general life conversations. I have taken so much from our interactions.

Lastly, I would like to thank my family. Without the support of my parents, Billy and Margaret, I would not be here today. The sacrifices they have made throughout their lives never cease to amaze me. They have unconditionally supported my hopes and dreams, even when it led me away from home. Their morals and principles have always served as a guiding light for me throughout these years. To my brothers, Joe, Padhraic, Liam, Gearoid and Ronan, who have always lent a supportive ear when things have gotten difficult. I appreciate that no matter how far away we live from each other, you're always a phone call away and willing to drop everything for me at a moments notice. To the wonderful family I've married into, the Sroa's, I am eternally grateful for the warmth you've shown me and how you've made me feel at home again so far away from Ireland. I look forward to a lifetime of adventures and new memories together. And finally to my wife, Ramnique. You have given me unwavering love and support throughout this process. Your presence in my life has spurred my passion for my work and your infectious drive and ambition inspires me everyday. I couldn't be more grateful to have such an incredible life partner.

Chapter 1

Introduction

Electrical power systems have grown to form the backbone of modern-day society. From charging electric vehicles, to running heat pumps, electricity has permeated every aspect of our daily lives. The reliability of these networks has been one of the greatest engineering achievements of the 20^{th} century. Maintaining this reliability, however, in the face of increasing electrification and a changing generation fleet, is a new engineering challenge that we must rapidly face in order to mitigate the impacts of climate change. This dissertation is motivated by these challenges, and is focused on the increased control and modeling complexity of synchronously connected power systems as we continue to increase the deployment inverter-based resources (IBRs) onto our networks. The dynamics of IBRs are so disparate from fossil fuel generators that they are forcing a re-examination of the fundamental principles upon which we operate our power systems.

Before we dive into the details, it is useful to take a step back and, at a high level, understand why IBRs are such a transformative technology for power system operation. In the late 1800's, after a period knows as the war of the currents, AC power grids became the accepted means of transmitting electricity. The capability to easily step-up, and step-down, AC voltages through the laws of electromagnetism is what allowed us to transmit electricity over very long distances. The subsequent interconnected AC power networks built during the 20^{th} century transformed people's lives and revolutionized the economy. [1] During this period, researchers and system operators would coalesce around a set of power system control and operational practices based on the physical characteristics of synchronous machines.

Synchronous machines are electrical machines that convert rotational mechanical energy to electrical power at a particular voltage and frequency. One of the key attributes of a synchronous machine is an electromechanical coupling between the rotational speed of its mechanical shaft and the frequency of the electricity it generates. This electromechanical coupling was the cornerstone upon which power system control and operation was designed. By measuring the speed of a synchronous mechanical machine's shaft, we can

[1] A thorough exploration of the evolution of the power systems in North America can be found in [22].

sense if there is an imbalance between supply and demand of electricity across the power system, and take control accordingly. Additionally, generators also have an energy storage element, in the form of rotational inertia, that ensures instantaneous balance between supply and demand of electricity during any control action delay. The key point to note here is that frequency became the most important signal within a power system. Furthermore, as a control signal for synchronous machines, it is a very well defined and stable signal, i.e., the rotational speed of a synchronous machine's mechanical shaft. Due to the physical characteristics of a synchronous machine, its rotational speed cannot experience any discontinuities. This is advantageous in that we can reliably measure its rotational speed. On the flip-side, however, it does mean than any control action to change this rotational speed will be slow. [2]

These aforementioned system properties, i.e., large inherent energy buffer, stable and well-defined control signals, and slow control characteristics, allowed a number of important approximations and assumptions for analyzing these interconnected dynamical systems, primarily based on singular perturbation theory [56]. Specifically, as shown in Fig. 1.2, in power systems dominated by synchronous machines, there is a distinct timescale separation between electromagnetic phenomena and electromechanical phenomena. This timescale separation, and the fact that the electromagnetic dynamics were inherently stable, allowed us neglect these fast timescale dynamics and instead approximate them by a set of algebraic constraints. This, in turn, reduced the number of differential equations describing the dynamical response of the system. This simplification, along with the rated power of synchronous machines, in the range of 100's of MVA, admitted a much more computationally tractable system model for controller design and time-domain simulations. The importance of the latter point, i.e., the ability to quickly perform time-domain simulations, cannot be overstated. System operators perform countless of these simulations every day to ensure that the system is capable of withstanding, and recovering from contingencies, e.g., loss of transmission lines, loss of generation and faults. It is critical that operators continue to be able to carry out these simulations in order to retain the level of reliability we have come to expect from our power systems.

IBRs are a distinctly different class of device to synchronous machines and do not inherently have some of the properties outlined earlier. The most obvious of these differences is that frequency does not have the same physical meaning for IBRs. An IBR can, in theory, control the frequency of its locally modulated voltage completely independent of what is happening on the network.[3] This is in contrast to synchronous machines, whose mechanical frequency is physically coupled to its local electrical frequency. Additionally, for the purpose of control, an IBR does not easily have local access to a continuous stable frequency

[2]Another key attribute of synchronous machines is their ability to supply abnormally high levels of current during a fault on the power system. Broadly speaking, the topic of protection and fault current will not be explored within this dissertation, but it is worth noting as one of the other key features of a synchronous machine that we have designed our power systems around.

[3]There are reasons why it may not want to do this. But for the purpose of understanding the differences, it is possible.

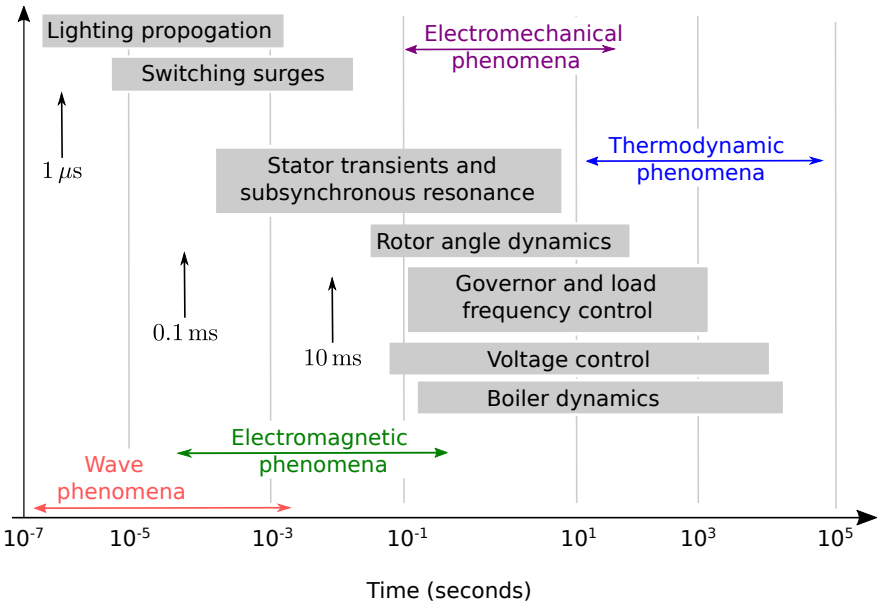

Figure 1.1: Historical time scale of power system dynamics [42]

measurement. Instead, it must estimate the frequency based on locally measured electrical quantities. This can be very difficult during system disturbances, e.g. phase jumps due to fault conditions [1]. Furthermore, and more importantly for the purpose of this work, IBRs have a much higher control bandwidth as shown in Fig. 1.2. Consequently, the timescale separation that historically allowed us to significantly simplify large-scale power systems for analysis and simulation, is no longer *inherently* satisfied [68]. We may be able to design IBR controllers to satisfy the requirements of singular perturbation theory, and continue to use historical assumptions, but this may be difficult and network dependent, and is still an open research question. One possible approach is to define performance requirements through standards, e.g., [48], but it very difficult to sufficiently cover all possible system conditions while not being too prescriptive such that it prohibits innovation. Therefore, at least in the near term, we may need to model these previously neglected electromagnetic dynamics.

Consideration of these electromagnetic dynamics increases the number of equations required to model the system dynamics. This increase in the number of equations is compounded by the relative size of synchronous machine to IBRs, i.e., for each synchronous machine that is displaced, we are adding 10's or 100's of IBRs. This increase in equations can result in unreasonable computation times for system analysis with very high penetrations of IBRs [98] and/or unexpected oscillatory behavior at the system level due to models used for controller design being unable to accurately capture the complex interactions through the network [21].

This dissertation seeks to circumvent this increased system complexity on two fronts.

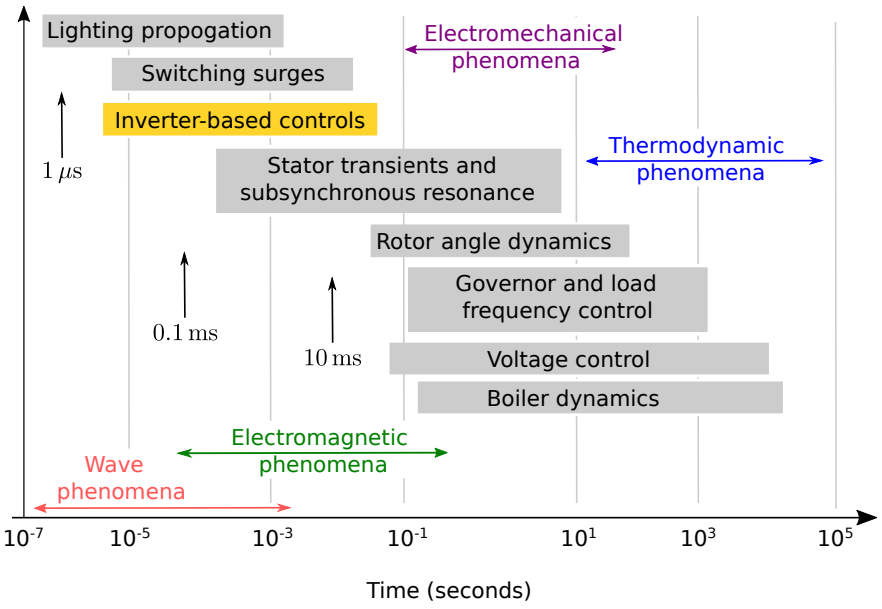

Figure 1.2: Time scale of power system dynamics with IBRs[42]

Firstly, we examine how supplementary control loops, that do not require information about the system or communication, can improve the dynamical response of IBRs. These types of controllers can be broadly categorized as model-free approaches, although we do assume that each IBR has detailed information about its own control scheme. Tuning a set of control gains on IBRs can be challenging. As system strength changes, both temporally and spatially, and inverter manufacturers perform firmware upgrades, the system dynamics, and subsequently the dynamic response of an IBR with fixed control gains, might vary considerably. The supplementary controllers proposed in this dissertation are meant to minimize system oscillatory behavior due to adverse controller interactions among devices and/or the network. Secondly, we examine ways of reducing the number of time-domain simulations that operators have to carry-out on a daily basis to ensure the reliable operation of their system. Specifically, we want to extract as much information from the minimum number of simulations we can to rapidly, and accurately, predict the response of the system under different conditions.

In summary, this dissertation first focuses on modeling of voltage-source converters coupled with an electrochemical battery in Chapter 2, and uses these models for control and simulation in Chapters 3-6. The core contribution in Chapter 2 is to show that, for the particular IBR control scheme considered, the DC-side can be modeled as an ideal voltage source. Chapter 3 considers the case where we have a collection of power electronics devices connected through a microgrid and how a malicious actor might try to destabilize IBRs on the network. We show how the multiple layered digital control loops that control IBRs introduce a new attack vector for malicious actors seeking to disrupt the grid. Chapter

4 continues at the microgrid level and proposes a local adaptive controller that seeks to de-sensitize the IBR to attack vector proposed in Chapter 3. Specifically, we propose to stochastically adjust the outer-loop controller bandwidth to nullify any controller resonance and/or coupling that the adversary could exploit. This proposed defensive controller is designed to remain inactive during normal operation and only be activated during sustained abnormal operation.

Chapter 5 takes us up to the transmission grid and seeks to design a power oscillation damping (POD) controller that is periodically tuned online to improve the dynamic response of IBRs. The wide range of operating conditions an IBR experiences, as the online generation fleet changes throughout the day, complicates the tuning process. This is particularly challenging for grid following (Gfl) inverters, whose phase-locked loop (PLL) is typically tuned assuming a sufficiently strong external grid. Depending on temporal and spatial factors, this assumption may not be valid at times. The proposed controller first builds a reduced order model (ROM) of the IBR and its interaction with the grid. Following this, it designs a POD controller to improve the eigenvalues of this ROM. We show how the proposed controller improves the response of the IBRs and minimizes undesirable system oscillations following a disturbance. Chapter 6 moves away from control to simulation and explores how recent advancements in the field of scientific machine learning (SciML) can help us accelerate the process of simulating these large-scale complex systems. As we replace large synchronous machine with hundreds and thousands of IBRs, the computational complexity of simulating these systems significantly increases. SciML is a rapidly growing cross-disciplinary research area that aims to blend the principles of scientific computing with state-of-the-art machine learning techniques to achieve insights and performance unattainable by either approach individually. Our work in Chapter 6 focuses on using SciML to predict the response of a large interconnected power system following a large loss of generation for different penetration of grid forming (GFM) & Gfl IBRs.

Finally, we conclude with some summarizing comments, key findings, and notes on exciting research questions and directions. As described earlier, power systems are undergoing the largest transition since their inception. Not only is this a critical societal challenge we must succeed in to decarbonize, it is also an incredibly interesting area of research and one that is ripe for cross-disciplinary innovation. Power systems are truly one of the most complex systems we have designed as humans. From millisecond distributed non-linear control, to privacy preserving spatial and temporal optimization, to policy and behavioral science, we need innovation and breakthroughs at all levels to succeed in decarbonizing our world.

Chapter 2

Modeling of Battery Driven Voltage Source Converters

This chapter was co-authored with Jose Daniel Lara and Rodrigo Henriquez-Auba, both PhD students at UC Berkeley at the time, Bala Kameshwar Poolla, then a Postdoc at UC Berkeley, and Prof. Duncan Callaway, Associate Professor of Energy and Resources at the University of California, Berkeley. The text was previously published 2020 IEEE international conference on communications, control, and computing technologies for smart grids (SmartGridComm); see [87] for the full citation. The text has been reformatted for inclusion in this dissertation.

Abstract

With the increasing interest in converter-fed islanded microgrids, particularly for resilience, it is becoming more critical to understand the dynamical behavior of these systems. This paper takes a holistic view of grid-forming converters and considers control approaches for both modeling and regulating the DC-link voltage when the DC-source is a battery energy storage system. We are specifically interested in understanding the performance of these controllers, subject to large load changes, for decreasing values of the DC-side capacitance. We consider a fourth, second, and zero-order model of the battery; and establish that the zero-order model captures the dynamics of interest for the timescales of the examined disturbances. Additionally, we adapt a grid search for optimizing the controller parameters of the DC/DC controller and show how the inclusion of AC-side measurements into the DC/DC controller can improve its dynamic performance by predicting the evolution of the DC-side dynamics. This improvement in performance allows for a reduction in transient voltage deviations across the DC-link capacitor and, consequently, potentially reducing the risk of premature failure.

2.1 Introduction

As synchronously connected power systems shift towards systems with high penetration of converter interfaced generation (CIG), it becomes more critical to understand the dynamical and transient behavior of these systems. These converter-dominated power systems are already prevalent in the form of microgrids [54], motivated by increased resilience to natural disasters [16]. Recent work has explored the small-signal stability of the DC/AC converter and its interaction with the grid. A common approach when analyzing voltage source converter (VSC) behavior is to model the DC-side of the converter as an ideal voltage source [25, 68]. On the other hand, when studying the dynamics of the DC-side, the grid is often simplified as a resistive load [12, 11]. From a small-signal perspective, an independent analysis of each subsystem may be adequate due to the minimal interaction of their control loops. However, this approach gives little insight into the dynamical behavior of these coupled systems during grid-scale transient events, particularly faults or large load steps and when the operating conditions differ substantially from the steady-state operating point used in the linearization.

This paper examines the DC-side dynamics of a battery energy storage system (BESS), subject to AC-side disturbances, under different DC-side control strategies. The objective of these controllers is to tightly regulate the voltage across a DC-link capacitor. DC-link capacitors act as energy buffers and supports a constant voltage on the DC-side of a VSC. A tight regulation of this voltage is critical to the operation of the VSC, as momentary drops may restrict the VSC's power production capabilities [11]. Therefore, large electrolytic capacitors are used in order to have a substantial buffer to minimize the DC voltage deviations during disturbances. These capacitors being typically bulky, expensive and unreliable are one of the most common modes of failure in power electronic systems [103]- with system transients and overloading identified as two of the primary causes of failure [110].

One proposed improvement in converter design is to replace these electrolytic capacitors with small film capacitors that are more robust and reliable [60]. As the DC-link capacitance is reduced, voltage fluctuations during transients increase as there is a momentary mismatch between the power injected into the grid and the power supplied from the DC source e.g., a battery. In order to deploy these small film capacitors, the DC-side control must rapidly correct power mismatch to ensure adequate AC-side operation and minimize transient over-voltages on the capacitor.

In this work, we examine different control approaches for minimizing the required DC-link capacitance of a BESS. Specifically, we consider the case of a grid-forming inverter supporting an islanded microgrid with a BESS as its DC source. Grid-forming inverters differ from grid-following inverters–the dominant mode of operation today, in that the former behave as a controllable voltage source behind a coupling reactance [32]. Consequently, they do not directly control their power injection into the grid but rather control the frequency and amplitude of their output voltage [68]. Their power injections, therefore, inherently increase or decrease to balance any changes in load. When choosing a DC-link capacitor for a grid-forming inverter, adequate care must be taken that it is appropriately

sized to ensure satisfactory behavior under the largest expected load change and/or fault conditions. This work considers the existing measurements used in the control loop of grid-forming converters as inputs into the DC/DC controller to predict the evolution of DC-link capacitance dynamics and, consequently, improve the regulation of the DC bus voltage.

For modeling our DC source, we consider a Li-ion battery as the BESS. In comparison to previous work, which modeled the battery as an ideal voltage behind a resistor [12, 11], we employ a model of the battery which captures the dynamics of the electrochemical processes as we increase/decrease the current drawn from the battery. As we reduce the DC-link capacitance, and the dynamics on the DC-side become faster, it may become more important to model the underlying battery dynamics to accurately capture the dynamical response of the DC source [35].

The contributions of this paper are as follows:

1. we develop a full-order dynamical model for a battery-driven voltage source converter,
2. we examine the impact of battery chemistry dynamics on overall DC-side dynamical response and establish that a zero-order model captures the dynamics of interest for the disturbances considered,
3. we improve upon the DC-side controller in [11] by the inclusion of AC-side measured quantities to predict evolution of DC-side dynamics to compensate for the DC/DC controller dead-time and DC/DC inductor dynamics,
4. we show that, for particular parameterizations of inner-control loops, the behavior of the VSC can help reduce the risk of saturation of the VSC modulation index.

2.2 Methodology

In this section we outline a methodology for choosing the control gains of the DC/DC converter in order to understand and improve the dynamical behavior of the DC-side of the CIG. To this end, we use a linearized model of our system, presented in Section 2.2, and identify a set of gains that result in stable operating points. Subsequently, in Section 2.2, we determine the gains from this set which optimize the dynamical performance of the DC/DC controller under large disturbances. To account for the discrete nature of the DC/DC controller we utilize a Pade approximation of the associated dead-time delay. The average output performance for a step input of a 2^{nd} and 3^{rd}-order approximation is used to model the dead-time of the DC/DC controller.

Small-signal tuning

We express the non-linear differential equations (2.6)-(2.14) as

$$\dot{\boldsymbol{x}} = \boldsymbol{f}(\boldsymbol{x}, \boldsymbol{u}, \boldsymbol{w}), \tag{2.1}$$

where $\boldsymbol{x}, \boldsymbol{u}, \boldsymbol{w}$ correspond to the states, inputs, and external disturbances (loads), respectively. For the purpose of analysis, we linearize this system around an equilibrium point $(\boldsymbol{x}_{eq}, \boldsymbol{u}_{eq}, \boldsymbol{w}_{eq})$ to obtain a resultant linear system

$$\Delta \dot{x} = A\Delta x + B\Delta u + G\Delta w, \tag{2.2}$$

The task of small-signal tuning involves finding a set of DC-side control gains

$$K^{\text{DC}} = [K_p^{v_{\text{DC}}}, K_i^{v_{\text{DC}}}, K_p^{i_{\text{DC}}}, K_i^{i_{\text{DC}}}, K_{\text{pred}}] \tag{2.3}$$

which satisfy some pre-specified design requirements, e.g.,

$$\Re[\lambda_i(A(K^{\text{DC}}))] \leq \lambda_{\text{crit}} \quad \forall i, \tag{2.4a}$$

$$\zeta_i \geq \zeta_{\text{crit}} \quad \forall i, \tag{2.4b}$$

$$K^{\text{DC}}_{\text{min}} \leq K^{\text{DC}} \leq K^{\text{DC}}_{\text{max}}, \tag{2.4c}$$

where λ and ζ correspond to the eigenvalues and the damping ratio of the linearized model respectively, λ_{crit} and ζ_{crit} are design requirements, and $K^{\text{DC}}_{\text{max}}$ and $K^{\text{DC}}_{\text{min}}$ represent some pre-specified limits on the control gains. We denote this set of all permissible gains by the set Γ. The limits on the gains were chosen based on empirical observations of the stable region for the specific use case, the considered objective, and encompass the gains from [12]. Larger values for these gains can result in improved speed of response from the controller. However, if these gains are too high the system becomes internally unstable and/or results in large oscillatory behavior.

Large-signal tuning

On identifying a set of suitable small-signal gains Γ, an exhaustive search over this set is performed to optimize the dynamical performance of the full non-linear system when it is subject to large disturbances, e.g., large load step changes. In particular, we seek to identify the set of gains that minimize the DC voltage deviation from its set point. This can be expressed mathematically as minimizing the ℓ_2-norm

$$\begin{aligned} &\min_{K^{\text{DC}} \in \Gamma} \; ||v^*_{\text{DC}} - v_{\text{DC}}(t)||_2^2 \\ &\text{subject to } (2.6) - (2.14), \\ &\qquad p_l(t_0) = p_l, \\ &\qquad p_l(t) = p_l + \Delta p_l, \end{aligned} \tag{2.5}$$

where p_l is the nominal active power load and Δp_l represents a disturbance in the form of a step-change increase in the load. We first optimize the DC/DC control gains with $K_{\text{pred}} = 0$ and then benchmark the improved dynamical performance for cases where $K_{\text{pred}} \neq 0$. Section 2.4 discusses the design requirements and disturbance used in (2.4) and (2.5) respectively.

2.3 System Modeling and Control Implementation

Grid Forming VSC Control Scheme

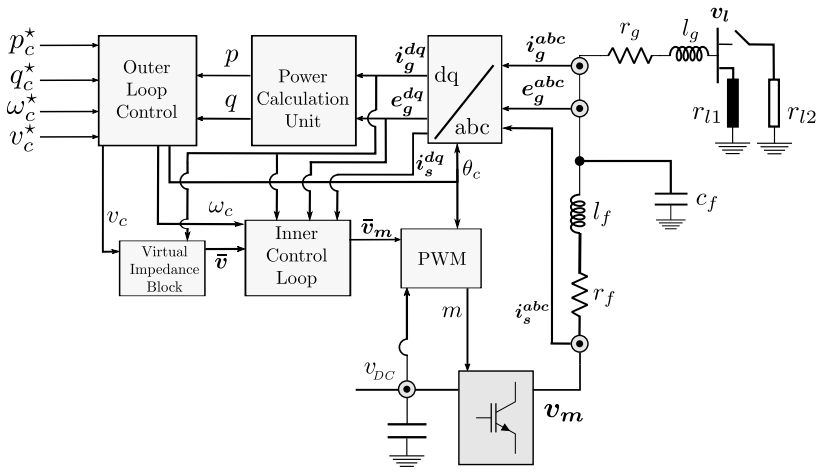

Figure 2.1: Grid-forming VSC control scheme.

The modeling and simulation of the AC-side, including the VSC, is implemented in a synchronous reference frame (SRF), with the mathematical model defined in per unit. The (dq)-frame quantities are represented in bold, lower-case complex space vectors of the form: $\boldsymbol{x} = x^d + jx^q$. The proposed control model depicted in Fig. 2.1 is based on a state-of-the-art VSC control scheme described in [23, 66, 74]. The power calculation unit computes the active and reactive quantities given by $p_c + jq_c = \boldsymbol{e}_g\bar{\boldsymbol{i}}_g$ where $(\bar{\cdot})$ denotes the complex conjugate. This is followed by an outer control loop that consists of active and reactive power controllers providing the output voltage magnitude v_c and frequency ω_c references by adjusting the predefined set points $(x^\star)$ according to a measured power imbalance:

$$\omega_c = \omega_c^\star + R_c^p\,(p_c^\star - \tilde{p}_c), \quad v_c = v_c^\star + R_c^q\,(q_c^\star - \tilde{q}_c), \tag{2.6}$$

where R_c^p, R_c^q denote the active and reactive power droop gains and $\tilde{p}_c$, $\tilde{q}_c$ represent the low-pass filtered active and reactive power measurements of the form:

$$\dot{\tilde{p}}_c = \omega_z\,(p_c - \tilde{p}_c), \quad \dot{\tilde{q}}_c = \omega_z\,(q_c - \tilde{q}_c), \tag{2.7}$$

where ω_z is the filtering frequency. The outer-loop voltage set point may be passed through a virtual impedance block (r_v, l_v), resulting in a cross-coupling between the d- and q-components via a terminal current measurement $\boldsymbol{i}_g$ as

$$\bar{\boldsymbol{v}} = v_c - (r_v + j\omega_c\,l_v)\,\boldsymbol{i}_g. \tag{2.8}$$

This new voltage vector set point and the frequency set point are then fed to the inner control loop consisting of cascaded voltage and current controllers operating in a SRF

$$\bar{\boldsymbol{i}}_s = K_p^v\,(\bar{\boldsymbol{v}} - \boldsymbol{e}_g) + K_i^v\,\boldsymbol{\xi} + j\omega_c\,c_f\,\boldsymbol{e}_g + K_f^i\,\boldsymbol{i}_g, \tag{2.9a}$$

$$\bar{\boldsymbol{v}}_m = K_p^i\,(\bar{\boldsymbol{i}}_s - \boldsymbol{i}_s) + K_i^i\,\boldsymbol{\gamma} + j\omega_c\,l_f\,\boldsymbol{i}_s + K_f^v\,\boldsymbol{e}_g, \tag{2.9b}$$

where $\dot{\boldsymbol{\xi}} = \bar{\boldsymbol{v}} - \boldsymbol{e}_g$ and $\dot{\boldsymbol{\gamma}} = \bar{\boldsymbol{i}}_s - \boldsymbol{i}_s$ denote the respective integrator states; $\bar{\boldsymbol{i}}_s$ and $\bar{\boldsymbol{v}}_m$ represent the internally computed current and voltage references, $\boldsymbol{e}_g$ is the voltage measurement across the filter capacitance, $\boldsymbol{i}_s$ is the switching current, K_p, K_i, and K_f are the proportional, integral, and feed-forward gains respectively, and superscripts v and i denote the voltage and current SRF controllers. The output voltage reference $\bar{\boldsymbol{v}}_m$ combined with the DC-side voltage v_{DC} generates the pulse-width modulation (PWM) signal $\boldsymbol{m}$.

The electrical interface to the microgrid includes an RLC filter (r_f, l_f, c_f) and an equivalent impedance (r_g, l_g) modeled in SRF and defined by the angular converter frequency

$$\dot{\boldsymbol{i}}_s = \frac{\omega_b}{l_f}(\boldsymbol{v}_m - \boldsymbol{e}_g) - \left(\frac{r_f}{l_f}\,\omega_b + j\omega_b\,\omega_c\right)\boldsymbol{i}_s, \tag{2.10a}$$

$$\dot{\boldsymbol{i}}_g = \frac{\omega_b}{l_g}(\boldsymbol{e}_g - \boldsymbol{v}_l) - \left(\frac{r_g}{l_g}\,\omega_b + j\omega_b\,\omega_c\right)\boldsymbol{i}_g, \tag{2.10b}$$

$$\dot{\boldsymbol{e}}_g = \frac{\omega_b}{c_f}(\boldsymbol{i}_s - \boldsymbol{i}_g) - j\omega_c\,\omega_b\,\boldsymbol{e}_g, \tag{2.10c}$$

with $\boldsymbol{v}_m$ representing the modulation voltage and $\boldsymbol{v}_l$ denoting the nodal voltage at the load bus. The system base frequency is represented by ω_b and equals the nominal frequency. The complete state-space representation of a single grid-forming inverter, therefore, comprises 13 states of the form

$$\hat{x}_{\text{vsc}} = \left[\boldsymbol{e}_g^{\text{dq}},\, \boldsymbol{i}_g^{\text{dq}},\, \boldsymbol{i}_s^{\text{dq}},\, \boldsymbol{\xi}^{\text{dq}},\, \boldsymbol{\gamma}^{\text{dq}},\, \theta_c,\, \tilde{p}_c,\, \tilde{q}_c\right]^\top. \tag{2.11}$$

The control input vector $u_{\text{vsc}} = [p_c^\star,\, q_c^\star,\, v_c^\star, \omega_c^\star]^\top$ provides operator set points. More details on the overall converter control structure and employed parametrization can be found in [74, 66, 68].

DC-side model

The model of the DC-side consists of a BESS, an idealized DC/DC buck/boost converter with an appropriately sized inductor, and a DC-link capacitor. This interconnected system is then interfaced to the VSC as shown in Fig. 2.2.

DC/DC Controller

For the DC/DC controller in Fig. 2.2, we investigate the improved dynamical performance with the inclusion of the measured AC-side quantities into the control logic. A dual-loop PI

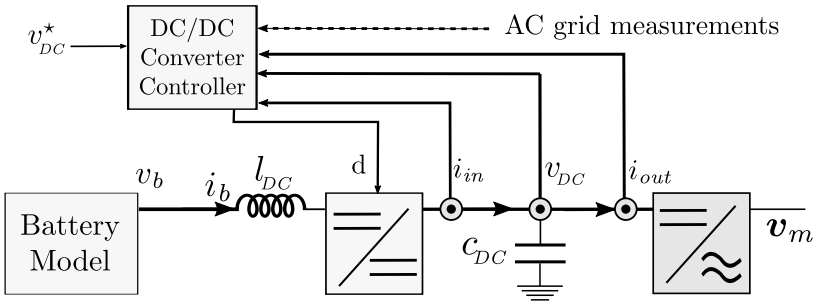

Figure 2.2: DC-side model.

DC/DC controller is shown in Fig. 2.3 and modeled as

$$\dot{\eta} = v^{\star}_{\text{DC}} - v_{\text{DC}} \tag{2.12a}$$
$$i_{\text{ref}} = K_p^{v_{\text{DC}}} \left(v^{\star}_{\text{DC}} - v_{\text{DC}}\right) + K_i^{v_{\text{DC}}} \eta, \tag{2.12b}$$
$$\dot{\zeta} = i_{\text{ref}} + i_{\text{out}} - i_{\text{in}}, \tag{2.12c}$$
$$d = K_p^{i_{\text{DC}}} \left(i_{\text{ref}} + i_{\text{out}} - i_{\text{in}}\right) + K_i^{i_{\text{DC}}} \zeta + K_{\text{pred}} \Delta i_{\text{out}}. \tag{2.12d}$$

The outer-loop (2.12a)-(2.12b), maintains a constant DC bus voltage while the inner loop (2.12c)-(2.12d), is for current tracking. The inclusion of a feed-forward term, i_{out}, in the internal PI control loop is for improving the controller performance by the addition of information about the disturbance. This disturbance was primarily a set-point change of the VSC in previous works [12]. For the case of a grid-forming VSC, however, this disturbance includes unexpected load changes where the additional required power will be inherently drawn from the DC-link capacitor.

The addition of the term $K_{\text{pred}}\,\Delta i_{\text{out}}$ in (2.12d) is motivated by [37], where the authors sought to minimize the required DC-link capacitance for a converter-interfaced three-phase load. In [37] the authors note that the inclusion of a feed-forward term alone is inadequate to instantaneously balance the current flow across the capacitor due to inherent system response time delays, mainly due to inductor dynamics. To offset these delays, we use a one-step predictor based on the forward Euler method to predict the evolution of system dynamics. The feed-forward predicted current, Δi_{out} value is approximated by (2.13)

$$\Delta i_{\text{out}} \approx \frac{\Delta P}{\Delta v_{\text{DC}}} \approx \frac{T_s(v_m^d\, \dot{i}_s^d + v_m^q\, \dot{i}_s^q)}{v_{\text{DC}}}, \tag{2.13}$$

where T_s is the switching period of the DC/DC converter, and $\dot{i}_s^d$ and $\dot{i}_s^q$ are calculated using (2.10a). We benchmark the improvement in dynamical performance for a non-zero K_{pred} against the controller in [11]. The advantage of a one-step predictor over derivative control in a PID controller is that we can predict the evolution of the DC-side dynamics before they begin to manifest and minimize noise amplification in estimating the rate of change of the

current. The duty-cycle d of the DC/DC converter in this work has a maximum value of 0.9 to mimic the behavior of a practical converter [113].

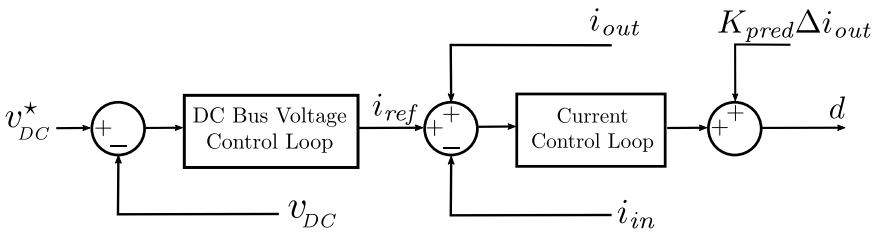

Figure 2.3: Structure of the DC-side controller

Battery Model

As previously outlined, prior work on this topic modeled the electrochemical battery as an ideal voltage source behind a resistor [12, 11]. In the presence of a large DC-link capacitance, and consequently a large energy buffer, this is a reasonable modeling assumption. However, as we reduce the DC-link capacitance, the dynamics of the electrochemical storage may become more important to model. A common method for parameterizing an equivalent circuit model for batteries is electrochemical impedance spectroscopy [35, 97]. This method measures the voltage response to harmonic current input across a frequency range of interest (3 kHz to 30 kHz [82]) and an equivalent circuit is adapted to this data. These experimental data show that at high frequencies ($\geq 250 - 400$ Hz) the battery exhibits inductive behavior while lower frequencies ($\leq 250 - 400$ Hz) have a more capacitive response [101, 35, 82]. A generalized battery is shown in Fig. 2.4 where the high frequency behavior is modeled by a series of 2 RL parallel branches and the low frequency behavior is modeled by a series of 2 RC parallel branches.

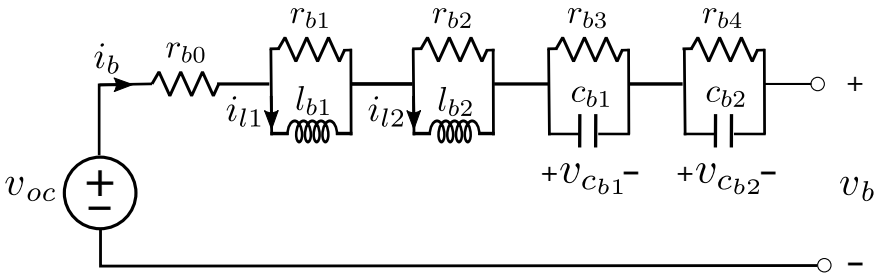

Figure 2.4: A generalized 4^{th}-order battery model.

Within this work we combine the two-time constant RC battery model from [40] with the two-time constant RL model from [82] as shown in Fig. 2.2. Both of these batteries'

chemistries are based on Lithium-ion and offer reasonable initial parameterization of a dynamic BESS model.

DC-side Electrical Model

In practice, the DC/DC converter is a buck/boost converter capable of both charging and discharging the battery. Here, we focus on the case when the converter is operating in the boost mode, i.e., supplying power to the grid. A similar analysis holds for the buck mode of operation. The per-unit averaged equations governing the electrical behavior on the DC-side with the converter operating in continuous mode, similar to [102], are then given by

$$\dot{i}_{l1} = \frac{\omega_b}{l_{b1}}(r_{b1}(i_b - i_{l1})), \quad \dot{i}_{l2} = \frac{\omega_b}{l_{b2}}(r_{b2}(i_b - i_{l2})), \tag{2.14a}$$

$$\dot{v}_{c_{b1}} = \frac{\omega_b}{c_{b1}}\left(i_b - \frac{v_{c_{b1}}}{r_{b3}}\right), \quad \dot{v}_{c_{b2}} = \frac{\omega_b}{c_{b2}}\left(i_b - \frac{v_{c_{b2}}}{r_{b4}}\right), \tag{2.14b}$$

$$\begin{aligned} v_b = v_{oc} - i_b\, r_{b0} - r_{b1}(i_b - i_{l1}) - r_{b2}(i_b - i_{l2}) \\ - v_{c_{b1}} - v_{c_{b2}} \end{aligned} \tag{2.14c}$$

$$\dot{i}_b = \frac{\omega_b}{l_{\text{DC}}}(v_b - (1-d)\, v_{\text{DC}}), \tag{2.14d}$$

$$\dot{v}_{\text{DC}} = \frac{\omega_b}{c_{\text{DC}}}(i_{\text{in}} - i_{\text{out}}), \tag{2.14e}$$

$$v_{\text{DC}}\, i_{\text{in}} = v_b\, i_b, \tag{2.14f}$$

where ω_b is the AC base frequency, d is the duty-cycle of the DC/DC converter, further discussed in Section 2.3, and i_{out} is the current flowing into the AC grid and given by

$$i_{\text{out}} = \frac{p_{\text{inv}}}{v_{\text{DC}}} = \frac{v_m^d\, i_s^d + v_m^q\, i_s^q}{v_{\text{DC}}}. \tag{2.15}$$

The full state-space model of the DC-side with a 4^{th}-order dynamic BESS model, denoted by $\hat{x}_{\text{DC}}^{4^{\text{th}}}$, is given by

$$\hat{x}_{\text{DC}}^{4^{\text{th}}} = [i_{l1},\, i_{l2},\, v_{c_{b1}},\, v_{c_{b2}},\, i_b,\, v_{\text{DC}},\, \eta,\, \zeta]^\top, \tag{2.16}$$

with the control input $u_{\text{DC}} = v_{\text{DC}}^\star$. The 2^{nd}-order model of the DC-side neglects the inductor dynamics of the battery (i.e., retains only the 2 RC branches in Fig. 2.4), while the 0^{th}-order model further neglects the dynamics of the capacitor and simply represents the battery as a voltage source behind a resistor, as in [12].

In the per unit case, the DC-side base power is the same the AC-side. The DC-side base voltage, however, is two times the AC-side peak line-to-neutral base voltage. This is done to obtain an AC-side voltage of 1.0 p.u. from the a DC-side voltage of 1.0 p.u. at unity modulation ratio [111]. The saturation of the PWM modulation index is implemented

similar to [75] as

$$\boldsymbol{v}_m = \frac{\min\{||\bar{\boldsymbol{v}}_m||_2, v_{\text{DC}}\}}{||\bar{\boldsymbol{v}}_m||_2}\bar{\boldsymbol{v}}_m, \tag{2.17}$$

where $\bar{\boldsymbol{v}}_m$ is given by (2.9b) and $||\bar{\boldsymbol{v}}_m||_2$ is

$$||\bar{\boldsymbol{v}}_m||_2 = \sqrt{\bar{v_m^d}^2 + \bar{v_m^q}^2}. \tag{2.18}$$

2.4 Results

The simulations are performed using the Julia programming language. The ModelingToolkit.jl package is used to construct the non-linear system and perform the Jacobian evaluations. The power rating of the VSC is 200 kVA and the parameters are taken from [23] while parameters for the DC-side are presented in Appendix 2.6. The controller design parameters used for both the small-signal and large-signal tuning are shown in Table 2.1. The small-signal parameter search is carried out by a grid search with step size 0.5. All the analysis presented here, including a description of all variables, is available on Github[1].

Table 2.1: Controller tuning parameters

Specification	λ_{crit}	ζ_{crit}	$K^{\text{DC}}_{\text{max}}$	$K^{\text{DC}}_{\text{min}}$	Δp_l
Value	-3	0.35	10	0	0.5 p.u.

Comparing BESS Models

In Fig. 2.5, we compare the DC-side voltage of the three BESS models, i.e., 4^{th}, 2^{nd}, and 0^{th}-orders for non-optimized controller gains under a load step change of $\Delta p_l = 0.5$ p.u. We observe that all models are in agreement regarding the dynamical response (also true for different controller gains). Further, we note that the results here only apply to a Lithium-ion based BESS for the parameters from [40, 82]. For the case of compressed air storage with associated mechanical dynamics and redox flow batteries, with different underlying chemistry; a higher order model representation may be necessary.

Impact of one-step predictor

In order to examine the improvement in controller performance by inclusion of the AC-side measurements, we examine the response of the system to a load step change of $\Delta p_l = 0.5$ p.u. for varying values of K_{pred}. A non-zero value of K_{pred} introduces a predictive term into

[1] https://github.com/Energy-MAC/DCSideBatteryModeling

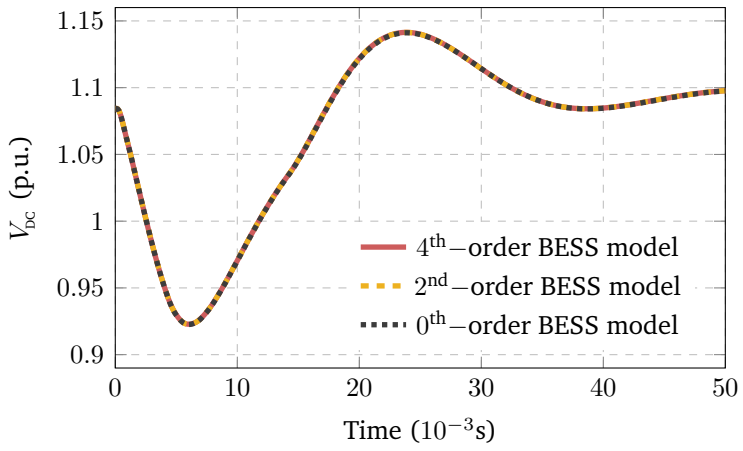

Figure 2.5: BESS response comparison for non-optimized gains for 0.5 p.u. active power load step.

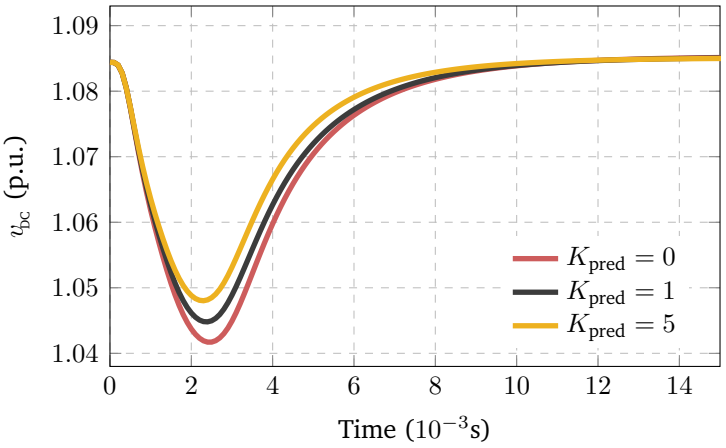

Figure 2.6: Optimized controller performance with one-step predictor for a 0.5 p.u. active power load step.

the DC/DC controller to achieve better regulation of the DC voltage. Fig. 2.6 shows the DC voltage for three different values of K_{pred}. Note that for increasing values of K_{pred} we achieve a better DC voltage regulation, albeit with diminishing returns. We achieve up to a $\sim 10\%$ reduction in the maximum DC voltage error after including the AC measurements. This reduction, achieved using existing measurements readily available in the VSC control loop, offers a means to reduce the severity of transients across the DC-link capacitor and reduce overloading in the event of over-voltage, two of the dominant reasons for premature failure [110].

Fig. 2.7 further explores the performance of the optimized controller for varying DC-

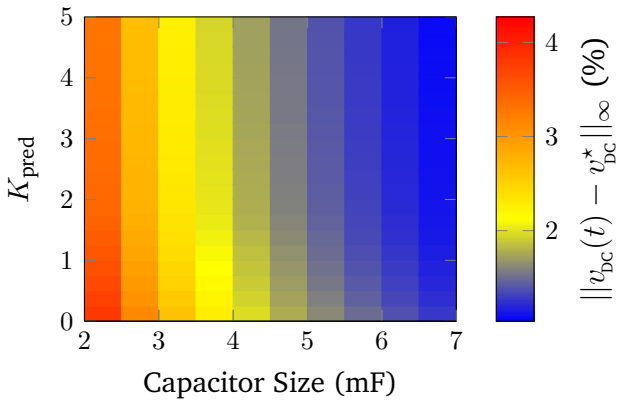

Figure 2.7: Comparing maximum v_{DC} deviation for varying DC-link capacitor sizing.

link capacitor sizing. We see that the inclusion of AC-side measurements does offer some improvement, however, due to the saturation behavior of the DC/DC boost converter, this improvement is upper-bounded. Therefore, while inclusion of the AC-side measurement improves the dynamical performance and reduces transient behavior across the capacitor, it only offers a modest reduction in DC-link capacitor sizing for a pre-specified ℓ_2 norm performance requirement.

In order to understand the limiting factor in the response of the BESS to regulate the DC voltage, we examine the battery current, i_b, shown in Fig. 2.8. We can see that the dead-time of the DC/DC controller only accounts for a small proportion of the delay in the response. Although a non-zero value of K_{pred} improves the response of the system, we see that the majority of the delay is due to the dynamics of the DC/DC inductor, in this case 3 mH. While this is a physical design limitation and there exist approaches to minimize the required inductance to improve dynamic response, e.g., increasing the switching frequency [40] or operating in discontinuous conduction mode [12], these design questions are beyond the scope of this work.

Examining VSC behavior

One additional benefit of including the AC-side measurements, and consequently, better regulation of the DC voltage, is the opportunity to reduce the DC-link capacitor size without saturating the PWM converter.

For the simulations considered in this paper with grid-forming inverter control gains from [23], the saturation of the PWM converter was avoided in all the examined cases. Fig. 2.9 shows both the DC voltage, V_{DC}, and magnitude of the modulated AC-side voltage, $||\boldsymbol{v}_m||$, for the case of $K_{\text{pred}} = 2$. The inner control loops of the grid-forming VSC respond on a faster timescale and significantly reduce the risk of saturating the modulation index of the VSC. The outer control loops of the VSC then re-adjust the set points to restore the

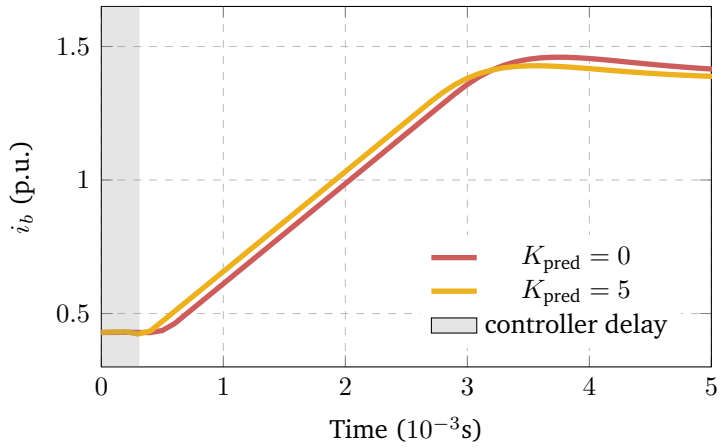

Figure 2.8: Battery current profile with one-step predictor.

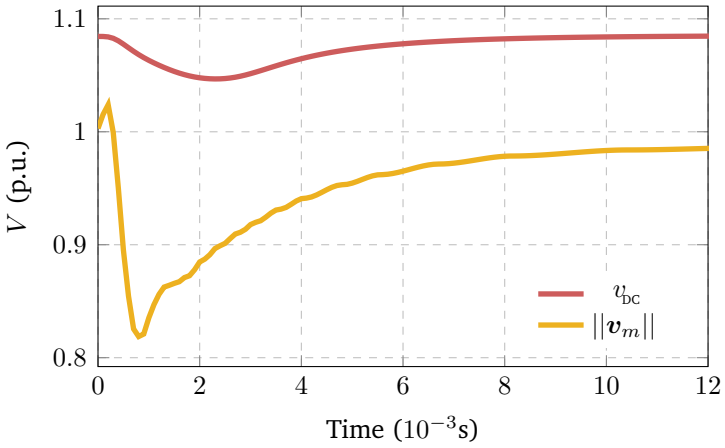

Figure 2.9: DC voltage and AC modulated voltage for $K_{\text{pred}} = 2$.

voltage to an acceptable operating level. While saturation was not an issue in this set up, it may be an issue for different parameterizations and/or disturbances.

2.5 Conclusion

This work focused on modeling and control of a BESS DC-source grid forming VSC. On the modeling side the DC/DC inductor was observed to be the dominant component dictating the dynamical behavior. A 4^{th}, 2^{nd}, and 0^{th}-order model of a BESS was examined and it was found that all three models were in agreement for the considered disturbances. For the DC/DC controller, it was found that the inclusion of readily available AC-side measurements

into the DC/DC converter control loop could reduce DC voltage deviations by up to $\sim 10\%$ during large step changes, thereby potentially reducing the risk of premature failure of the DC-link capacitor. Future work will focus on the behavior of these controllers under asymmetrical gird faults, additional DC-source technologies as well as further consideration of how fast inner-control loops of the VSC which may help alleviate the potential for saturation of the VSC modulation index.

2.6 Appendix

Table 2.2 lists the parameter values used for the DC-side model for simulations [40, 82]

Table 2.2: DC-side parameters

$f^s_{\text{DC/DC}}$	c_{DC}	l_{DC}	r_{b0}	r_{b1}	r_{b2}
3.2 kHz	2 mF	3 mH	1.5 mΩ	95 mΩ	0.4 mΩ

r_{b3}	r_{b4}	l_{b1}	l_{b2}	c_{b1}	c_{b2}
2.2 mΩ	0.55 mΩ	35 nH	15 nH	0.55 F	22.7 kF

Chapter 3

Malicious Control of an Active Load in a Mixed-Source Microgrid

This chapter was co-authored with Daniel Arnold, a research scientist at LBNL, Uros Markovic, then a Postdoc at ETH Zurich, and Prof. Duncan Callaway, Associate Professor of Energy and Resources at the University of California, Berkeley. The text was previously published at 2021 IEEE Madrid PowerTech; see [85] for the full citation. The text has been reformatted for inclusion in this dissertation.

Abstract

Power-electronic connected resources are slowly shifting power system dynamics from being dominated by the physics of synchronous machines to being determined by human-designed control loops within power electronic converters. This transition offers new flexibility in control design which, consequently, also increases the cyber-physical attack surface. Within this work we consider the use of eigenstructure assignment, i.e. both eigenvalue and eigenvector design, for the purpose of designing a destabilizing linear state-feedback controller for an active load. To this end, we show that at high levels of converter penetration there may exist an electromagnetic mode, in addition to the electromechanical mode reported in prior literature, that an adversary might seek to destabilize. In addition, we consider two levels of controllability that an adversary may have for an active load and show that, dependent on the mode the adversary is seeking to destabilize, the resulting manifestation of the attack on the grid may be different.

3.1 Introduction

Historically, the dynamics of power systems have been dominated by the inherent physical characteristics of synchronous machines. The behavior of an islanded microgrid can, however, be substantially different due to high penetration of converter-based resources, whose dynamics are almost entirely attributable to human-designed digital control loops. This

increased prevalence of human-designed control loops increases the cyber-physical attack surface. In this paper, we examine the vulnerability of an isolated mixed-source microgrid to a cyber-physical attack through malicious control of an active load.

There is a small body of work investigating the potential to destabilize power system dynamics through malicious control of connected physical devices. DeMarco and colleagues, [28] and [27], explored attacks purposefully introduced by malicious control of synchronous machines. In particular, they consider a simplified linearized model of an interconnected power system and design a linear state-feedback controller to cause a pair of complex conjugate eigenvalues to cross over into the right-half plane. In both papers the authors divide machines into a control group, under the control of an adversary, and a target group, which the adversary seeks to destabilize. In [28] the authors designate a sacrificial machine within the control group and permit it to have unconstrained participation in the resulting unstable system mode. The authors argue that, in the case considered, the machines in the target group would disconnect to protect themselves before the sacrificial machine damages itself. This requirement of a sacrificial machine is relaxed in the authors' subsequent paper [27], where an optimization approach is adopted to maximize the participation of the target group, relative to the control group, in the unstable mode. This approach was recently extended to examine cyber-physical attacks though aggregations of customer loads with emulated inertia control [14].

In addition to [28, 27], several recent papers have explored whether dynamic *loads* can deliberately destabilize power system dynamics. More specifically, the authors in [2] explore how an adversary could manipulate aggregate electric vehicle active power charging to destabilize the bulk power system. They adopt a partial eigenvalue placement and seek to minimize a state feedback matrix, K, such that the resulting closed-loop system is unstable. The work in [3] explores a similar question with generic controllable loads, e.g. demand response, at pre-defined vulnerable buses in the system. The attack considered in [108, 38, 39] studies discrete switching loads and how they can be controlled in order to cause resonance in inter-area oscillations.

This prior literature focuses on destabilizing inter-area modes in bulk power systems dominated by synchronous machines. However, we are unaware of any work focusing on systems with either high penetration of power electronic converters or the unique characteristics of microgrids. We focus on isolated microgrids for three key reasons: 1) the size of an individual load relative to generation capacity may make it easier for adversaries to gain sufficient control to initiate a cyber-physical attack; 2) these microgrids are among the first systems to experience significant levels of converter-based generation, whose human-designed control loops may offer additional flexibility in system destabilization; and 3) focusing on a small test system permits the use of full-order models, including network dynamics, while maintaining computational tractability.

We explore an approach that uses eigenstructure assignment to design a destabilizing state feedback controller for an active load. Eigenstructure assignment permits the use of feedback control in order to alter the eigenvalues and/or eigenvectors of a system. This approach has already been used in power systems for excitation control [47], control design

for doubly-fed induction generators [57] and predatory generation control [27].

We will examine its application in destabilizing an isolated mixed-source microgrid in as stealthy a manner as possible. Within this work we define a stealth attack as an attack where the destabilizing device is not easily identified and defeated before achieving its objective, e.g. forcing generation to trip offline to protect itself and/or damaging sensitive loads. This work is intended to better characterize the set of adversarial attacks, as well as their associated physical manifestation on the grid. Understanding these attacks will allow us to harden microgrids against them and develop adaptive defensive mechanisms to nullify their impact.

The primary contributions of this paper are twofold. Firstly, we identify an electromagnetic mode that is vulnerable to destabilization at high converter penetration. Secondly, we demonstrate the increased threat of a cyber-physical attack from an adversary gaining full access to converter control loops rather than simply adjusting active power demand.

3.2 Methodology

We follow the approach from [27] to design a destabilizing state-feedback controller. In this work the control group is the active load and the target group contains the synchronous generator and the grid-following converter. We begin by describing the system in Fig. 3.1 with a set of nonlinear differential equations

$$\dot{\boldsymbol{x}} = \boldsymbol{f}(\boldsymbol{x}, \boldsymbol{u}), \tag{3.1}$$

where $\boldsymbol{x}$ and $\boldsymbol{u}$ correspond to the states and inputs respectively. For the purpose of analysis, we linearize this system around an equilibrium point $(\boldsymbol{x}_{\mathrm{eq}}, \boldsymbol{u}_{\mathrm{eq}})$ to obtain a linear system:

$$\Delta\dot{\boldsymbol{x}} = \boldsymbol{A}\Delta\boldsymbol{x} + \boldsymbol{B}\Delta\boldsymbol{u}, \tag{3.2}$$

with $\boldsymbol{x} \in \mathbb{R}^n$, $\boldsymbol{A} \in \mathbb{R}^{n\times n}$, $\boldsymbol{B} \in \mathbb{R}^{n\times m}$ and $\boldsymbol{u} \in \mathbb{R}^m$. In order to design a destabilizing feedback controller, we first identify a suitable mode of the linearized matrix $\boldsymbol{A}$ to destabilize. We perform an eigenvalue decomposition and choose a mode that is already close to the right-half plane and in which the target group has high participation. Let us denote by V and W the right and left eigenvector matrices of matrix A respectively, such that $\boldsymbol{\Lambda} = \boldsymbol{W}\,\boldsymbol{A}\,\boldsymbol{V}$, where $\boldsymbol{\Lambda}$ is a diagonal matrix whose diagonal entries are the eigenvalues of $\boldsymbol{A}$. Then, according to [90], the participation of state i in mode j can be defined as

$$p_{ij} = \frac{w_{ij}v_{ji}}{\boldsymbol{w}_j^T\boldsymbol{v}_j}, \tag{3.3}$$

where w_{ij} and v_{ji} are the elements of W and V respectively. Once we have identified a candidate mode to destabilize, we seek to design a feedback controller that achieves a desired closed-loop unstable eigenvalue $\hat{\lambda}$. In addition to meeting the eigenvalue specification

criteria, we seek to design the corresponding eigenvector $\hat{\boldsymbol{v}}$ in order to minimize the participation of the states of the control group in the unstable mode. Recalling the definition of participation of state i in mode j in (3.3), the ideal case for an adversary is an eigenvector $\hat{v}$, with zero entries for the indices of the control group states and non-zero elements for the indices of the target group states. This would result in the control group having zero participation in the unstable mode and the target group having non-zero participation. In general, however, such an eigenvector will not exist [6]. Instead, we seek to design an eigenvector $\hat{v}$ that maximizes the participation of the target group (relative to the control group) in the unstable mode.

Once we have identified a candidate mode to be destabilized with a desired eigenvalue $\hat{\lambda}$, we begin by constructing the corresponding Hautus matrix $\boldsymbol{S}_{\hat{\lambda}}$ given by

$$\boldsymbol{S}_{\hat{\lambda}} = [(\hat{\lambda}\boldsymbol{I} - \boldsymbol{A}) \quad \boldsymbol{B}] \tag{3.4}$$

where $\boldsymbol{I}$ is the identity matrix. We then determine the matrix $\boldsymbol{K}_{\hat{\lambda}}$ of the form

$$\boldsymbol{K}_{\hat{\lambda}} = \begin{bmatrix} \boldsymbol{N}_{\hat{\lambda}} \\ \boldsymbol{M}_{\hat{\lambda}} \end{bmatrix}, \tag{3.5}$$

whose columns form a basis for nullspace of $\boldsymbol{S}_{\hat{\lambda}}$. Note that the rows of $\boldsymbol{K}_{\hat{\lambda}} \in \mathbb{R}^{(n+m)\times m}$ are partitioned in a similar manner to the columns of $\boldsymbol{S}_{\hat{\lambda}}$, i.e. $\boldsymbol{N}_{\hat{\lambda}} \in \mathbb{R}^{n\times m}$ and $\boldsymbol{M}_{\hat{\lambda}} \in \mathbb{R}^{m\times m}$. The dimension, m, of the input vector, u, will determine the dimension of the nullspace and consequently the degree of flexibility in designing the eigenvector $\hat{\boldsymbol{v}}$, expressed as

$$\hat{\boldsymbol{v}} = \boldsymbol{N}_{\hat{\lambda}}\boldsymbol{k} \tag{3.6}$$

for some $\boldsymbol{k} \in \mathbb{R}^{m\times 1}$. The i^{th} entry of $\hat{\boldsymbol{v}}$, therefore, is given by

$$\hat{v}_i = \sum_{j=1}^{m} [N_{\hat{\lambda}}]_{i,j} k_j. \tag{3.7}$$

Here, we let $\boldsymbol{N}_{\hat{\lambda}T}$ and $\boldsymbol{N}_{\hat{\lambda}C}$ denote the rows of $\boldsymbol{N}_{\hat{\lambda}}$ whose indices correspond to the states of the target and control group, respectively. We then seek to determine the optimal design vector $\boldsymbol{k}^\star$ for maximizing the ratio of ℓ_2-norm of the eigenvector entries corresponding to the target states and the ℓ_2-norm of the eigenvector entries corresponding to the control group. Similar to [27], we mathematically express this optimization problem as

$$\begin{aligned} \max_{\boldsymbol{k}} \quad & \frac{\boldsymbol{k}'[\boldsymbol{N}_{\hat{\lambda}T}]'\boldsymbol{N}_{\hat{\lambda}T}\boldsymbol{k}}{\boldsymbol{k}'[\boldsymbol{N}_{\hat{\lambda}C}]'\boldsymbol{N}_{\hat{\lambda}C}\boldsymbol{k}} \\ \text{s.t.} \quad & \boldsymbol{k}'\boldsymbol{k} = 1, \end{aligned} \tag{3.8}$$

where $[.]'$ denotes the transpose operator. Defining the matrices $\boldsymbol{G}$ and $\boldsymbol{H}$ as

$$\boldsymbol{G} = [\boldsymbol{N}_{\hat{\lambda}T}]'\boldsymbol{N}_{\hat{\lambda}T} \quad \boldsymbol{H} = [\boldsymbol{N}_{\hat{\lambda}C}]'\boldsymbol{N}_{\hat{\lambda}C}, \tag{3.9}$$

we rewrite this optimization as

$$\begin{aligned} \max_{\boldsymbol{k}} \quad & \frac{\boldsymbol{k}'\boldsymbol{G}\boldsymbol{k}}{\boldsymbol{k}'\boldsymbol{H}\boldsymbol{k}} \\ \text{s.t.} \quad & \boldsymbol{k}'\boldsymbol{k} = 1. \end{aligned} \tag{3.10}$$

Note that we assume that the matrix $\boldsymbol{H}$ is positive definite. Otherwise, we could choose the optimal design vector $\boldsymbol{k}^\star$ such that the control group would have zero participation in the unstable mode, i.e. $\boldsymbol{N}_{\hat{\lambda}C}\boldsymbol{k}^\star = \boldsymbol{0}$, which would be the best case for the adversary. As noted earlier, generally this will not be possible [6].

Having $\boldsymbol{H}$ as positive definite, we can safely assume that it has a well-defined square root. We now introduce a linear transformation given by

$$\boldsymbol{k} = \boldsymbol{H}^{-1/2}\boldsymbol{\nu}, \tag{3.11}$$

and substitute this into (3.10), which yields

$$\max_{\boldsymbol{\nu}} \frac{\boldsymbol{\nu}'(\boldsymbol{H}^{-1/2})^T\boldsymbol{G}\boldsymbol{H}^{-1/2}\boldsymbol{\nu}}{\boldsymbol{\nu}'\boldsymbol{\nu}}. \tag{3.12}$$

Note that (3.12) takes the form of the Rayleigh quotient and is therefore easily solvable. The optimal design vector $\boldsymbol{k}^\star$ is constructed using the eigenvector $\boldsymbol{\nu}_{max}$ corresponding to the largest eigenvalue of (3.12), and is given by

$$\boldsymbol{k}^\star = \boldsymbol{H}^{-1/2}\boldsymbol{\nu}_{max}. \tag{3.13}$$

We then construct the feedback matrix $\boldsymbol{F}$ follows. Let us define

$$\hat{\boldsymbol{w}} = \boldsymbol{M}_{\hat{\lambda}}\boldsymbol{k}^\star\,,\ \hat{\boldsymbol{v}} = \boldsymbol{N}_{\hat{\lambda}}\boldsymbol{k}^\star, \tag{3.14}$$

and construct the real matrices $\boldsymbol{W}$ and $\boldsymbol{V}$ of the form

$$\boldsymbol{W} = [Re\{\hat{\boldsymbol{w}}\}\, Im\{\hat{\boldsymbol{w}}\}\, \boldsymbol{0}\, \ldots\, \boldsymbol{0}], \tag{3.15a}$$

$$\boldsymbol{V} = [Re\{\hat{\boldsymbol{v}}\}\, Im\{\hat{\boldsymbol{v}}\}\, Re\{\boldsymbol{v}_3\}\, Im\{\boldsymbol{v}_3\}\, \ldots\, \boldsymbol{v}_{n-1}\, \boldsymbol{v}_n], \tag{3.15b}$$

where $[\boldsymbol{v}_3, \ldots.\boldsymbol{v}_{n-1}, \boldsymbol{v}_n]$ are the remaining original eigenvectors from the state-space matrix $\boldsymbol{A}$ given in (3.2). The feedback matrix $\boldsymbol{F}$ is then given by

$$F = \boldsymbol{W}\boldsymbol{V}^{-1}. \tag{3.16}$$

Provided that the columns in (3.15b) are linearly independent, the matrix $\boldsymbol{F}$ given by (3.16) exists and is unique (see Theorem 1 in the Appendix).

3.3 Microgrid Model

The microgrid considered in this work is shown in Fig. 3.1. It comprises a synchronous generator (SG), a Gfl inverter, an active load (AL) and a passive load (PL) characterized by its resistance and inductance, r_L and l_L respectively. The synchronous machine model adopted from [96, 68], encompassing a two-pole machine with a governor, an automatic voltage regulator (AVR) and power system stabilizer (PSS), yields a 13^{th}-order model including transformer dynamics. The grid-following inverter is represented using a 15^{th}-order model (see [66, 24]) while the active load comprises 12 states with the inclusion of filter dynamics [13]. Finally, similar to [77], we model the current dynamics of both the line and the constant impedance load, and include a large virtual shunt resistor, $R_v >> 1\,\text{p.u.}$, to ensure that nodal voltages are well defined. Therefore, the dimension of the entire model is $x \in \mathbb{R}^{46}$. Full details about specific models and parameters are available online[1].

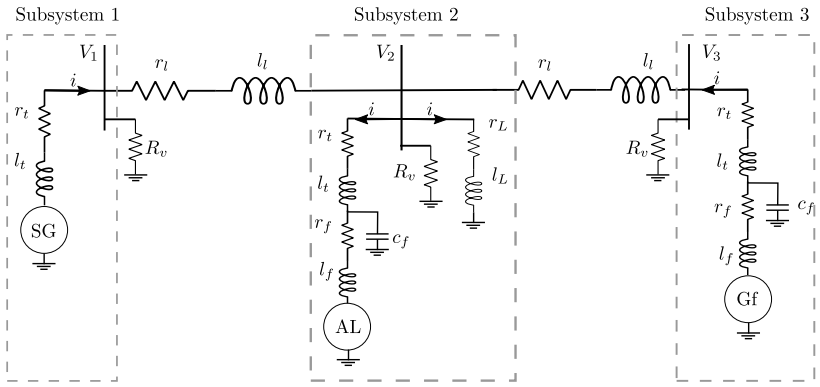

Figure 3.1: Microgrid Test Case.

A uniform (dq) SRF is used to model the test case, with quantities defined in per unit. The (dq)-frame quantities are represented in bold lower-case complex space vectors of the form: $\boldsymbol{x}_{dq} = x^d + jx^q$. For generation sources, positive current is defined as flowing from the source into the grid as shown in Fig. 3.1, while for loads we denote positive current as current flowing from the grid to the load.

The active load considered in this work, shown in Fig. 3.2, is adopted from [13]. It consists of three different PI control loops: PLL, a DC voltage controller and a current controller.

We use a Type-2 PLL, described in (3.17), for estimating the grid frequency and aligning the $d-$axis of the internal SRF with the measured grid voltage.

$$\omega_{pll} = \omega_n + K_p^{pll} e_g^q + K_i^{pll} \epsilon, \tag{3.17a}$$

[1] https://github.com/Energy-MAC

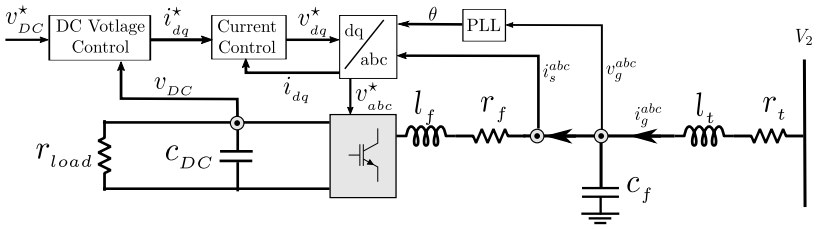

Figure 3.2: Active Load

$$\dot{\epsilon} = e_g^q, \tag{3.17b}$$
$$\dot{\theta}_{pll} = \omega_{pll}\omega_b. \tag{3.17c}$$

The outer-loop voltage controller, given by (3.18a)-(3.18b), maintains a constant DC bus voltage, whereas the inner loop controller, (3.18c)-(3.18d), tracks current reference:

$$\dot{\eta} = v^\star_{\text{DC}} - v_{\text{DC}}, \tag{3.18a}$$
$$\boldsymbol{i}^\star_{dq} = K_p^v\,(v^\star_{\text{DC}} - v_{\text{DC}}) + K_i^v\,\eta, \tag{3.18b}$$
$$\dot{\boldsymbol{\zeta}}_{dq} = \boldsymbol{i}^\star_{dq} - \boldsymbol{i}_{dq}, \tag{3.18c}$$
$$\boldsymbol{v}^\star_{dq} = K_p^i\,(\boldsymbol{i}^\star_{dq} - \boldsymbol{i}_{dq}) + K_i^i\,\boldsymbol{\zeta} + j\omega_{pll}\,l_f\,\boldsymbol{i}_{dq}. \tag{3.18d}$$

We will consider two cases of malicious state feedback for the active load. The first case is setpoint control, where the adversary only has the ability to change the DC voltage setpoint. In this case, we have that the input $u \in \mathbb{R}$, chosen based on the fact that it requires the least customization of the power electronics. The second case is full control, where the adversary has full access to the inner control loops and can inject control inputs into all proportional and integral control loops independently and, therefore, $u \in \mathbb{R}^5$. This case assumes the adversary either possess a power electronic converter that is heavily customizable or has introduced their own additional device into the network. These two cases are shown in Fig. 3.3 in blue and red respectively.

The dimension, m, of the input vector, u, will determine the flexibility in designing the eigenvector(s), discussed in Section 3.2, corresponding to the desired unstable eigenvalue(s).

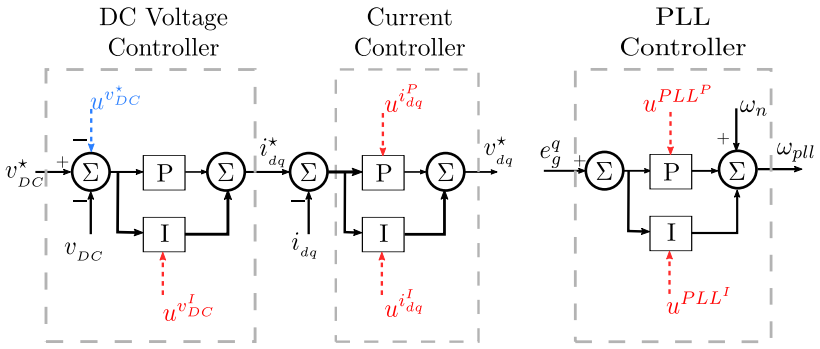

Figure 3.3: State feedback controllers considered

3.4 Results

For our analysis we consider the microgrid in Fig. 3.1 with a nominal loading of $1\,\text{p.u.}$ The synchronous machine and grid-following converter have installed system capacity of $0.4\,\text{p.u.}$ and $1.6\,\text{p.u.}$, respectively, and both have an active power setpoint of $0.5\,\text{p.u.}$ with respect to their internal base power. Initially, we consider the case where the adversary has control over an AL with nominal active power demand of $0.05\,\text{p.u.}$. We assume the adversary has access to both a model of the system as well as state measurements, or sufficient observability to reconstruct the state, for controller design.

Eigenstructure Analysis

Fig. 3.4 shows the eigenvalues closest to the right-half plane for the base case in green, i.e. the case with no cyber-physical attack. For both cases, i.e. setpoint control and full control introduced in Section 3.3, we seek to design a feedback controller to move a pair of complex eigenvalues close to the right-half plane (RHP) across the stability boundary and, consequently, destabilize the system. We consider two separate attacks. The first attack, shown in blue in Fig. 3.4, mirrors a pair of stable complex eigenvalues at $\lambda = -0.29 \pm 1.279j$ about the imaginary axis, i.e. $\hat{\lambda} = 0.29 \pm 1.279j$. The second attack, shown in orange, mirrors a pair of poorly damped eigenvalues at $\lambda = -0.45 \pm 16.16j$ about the imaginary axis, i.e. $\hat{\lambda} = 0.45 \pm 16.16j$. Within this work, the placement of the unstable eigenvalue is arbitrarily chosen and both eigenvalues could be pushed further into the RHP, although this would require larger gains in the feedback matrix $\boldsymbol{F}$. Both levels of control, i.e. setpoint control and full control, only differ in their eigenvectors. Their eigenvalues are the same for each attack. In addition, for both attacks considered, the remaining $n-2$ eigenvalues of the linearized model remain unaffected by the feedback matrix $\boldsymbol{F}$.

The participation of states in the unstable mode for each of the attacks are shown in Fig. 3.5. We see that the first attack is predominantly an electromechanical instability with

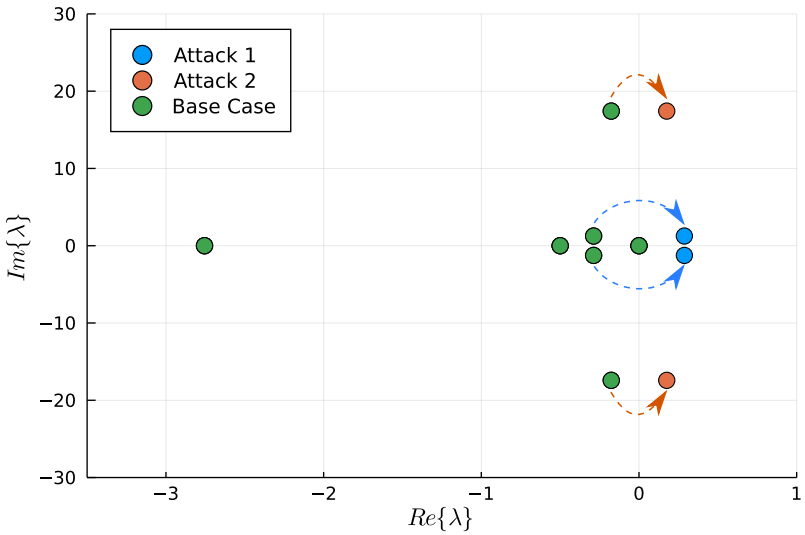

Figure 3.4: Truncated eigenvalue spectrum with and without malicious feedback controller

high participation from both the mechanical power, p_m, and angular frequency, ω_s, of the synchronous machine. The converter also has some, albeit significantly less, participation in the instability through the angle of its active power controller, θ_c, and the angle of the phase-lock loop, θ_{pll}. This electromechanical instability closely resembles the behavior in previous work [28, 27, 14] with the only minor difference being the participation of the converter.

The second attack considered, however, is novel. We see that this mode is primarily an electromagnetic instability with high participation of the grid-following converter filtered active power, $\tilde{p}_c$, the angle of its active power controller, θ_c, the angle of the phase-lock loop, θ_{pll}, and the integrator state of the phase locked-loop, ϵ_{pll}. These converter states interact with the flux linkage dynamics of the synchronous machine in this case.

The participation factors in the unstable mode shown in Fig. 3.5 correspond to the case of setpoint control. Due to the dimension of the input for setpoint control, i.e. $m = 1$, there is no flexibility in designing the eigenvector and it is simply given by $\hat{\boldsymbol{v}} = \boldsymbol{N}_{\hat{\lambda}}$. The question was then whether the additional flexibility in eigenvector assignment offered by the full control case would result in meaningful differences in the resulting eigenvectors. In this case, the state participation was very similar for both attacks considered, with full control marginally lowering the participation of the active load. The time domain behavior, however, was significantly different as will be shown in Section 3.4 and Section 3.4 for attack 1 and attack 2 respectively.

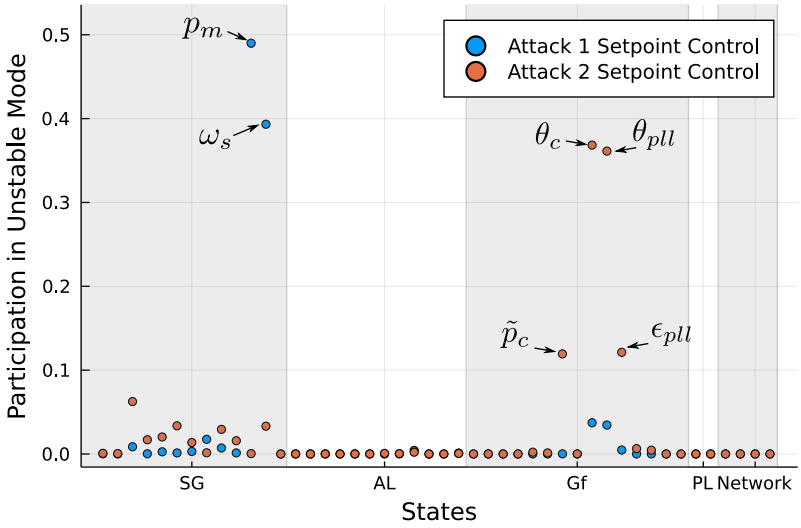

Figure 3.5: State participation in the unstable mode for both attacks considered

Time-domain simulations

Attack 1 - Electromechanical Instability

We examine the time-domain response of the system to better understand any differences between the resulting destabilizing state-feedback controllers. In each case the system is initially operating around a stable equilibrium and, at $t = 0s$, an adversary activates a destabilizing feedback controller. Fig. 3.6 and 3.7 show the active power and reactive power demand of the active load respectively. We see that the active power demand in Fig. 3.6 for setpoint control and full control are very similar with setpoint control exhibiting slightly larger oscillatory behavior. The reactive power in Fig. 3.7, however, is very different. We see that for setpoint control the reactive power demand is constant. This is due to the inability of setpoint control to affect the reactive power demand. For full control, however, the additional flexibility in state-feedback has allowed the resulting destabilizing controller to also change the reactive power demand of the AL and it also exhibits an oscillatory behavior.

Fig 3.8 shows the time series of the synchronous machine mechanical power, p_m. We see that both destabilizing controllers result in similar oscillatory behavior with the case of full control producing slightly larger oscillations.

This increase in oscillation amplitude may be attributable to the oscillatory reactive power of the AL exploiting the voltage dependency of the passive load, i.e. the AL is injecting/consuming reactive power in order to increase/decrease the active power consumption of the constant impedance load. We see the active and reactive power oscillatory time series in Fig. 3.6 and 3.7 respectively are 180^o out of phase with each other. Therefore, the active load appears capacitive, and consequently raising the nodal voltage, when maximizing its

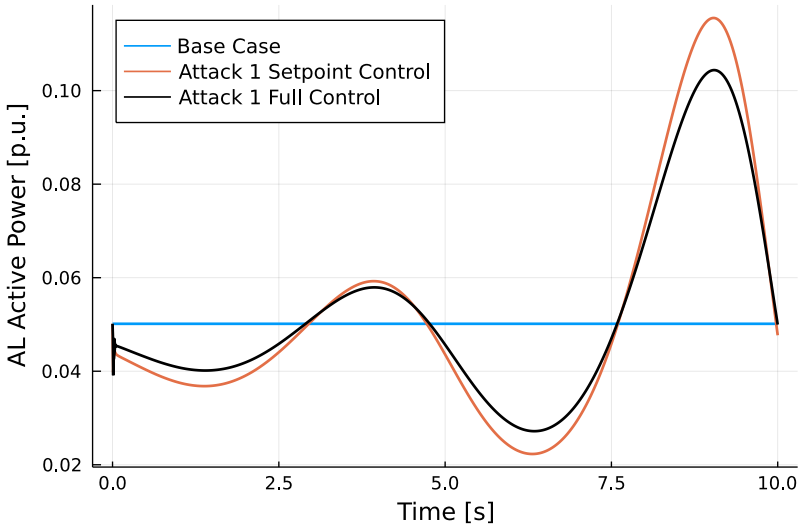

Figure 3.6: Time series of AL active power for both setpoint control and full control for attack 1.

active power consumption. This behavior is not present for the case of setpoint control.

Attack 2 - Electromagnetic Instability

Fig. 3.9 shows the time series behavior of the angle of grid-following converter active power controller, θ_c. For this particular attack, we see a larger difference between the case of setpoint control and full control. The amplitude of the oscillation for the full control grows at a much faster rate while the oscillations for the case of setpoint control appear only marginally unstable.

While the difference in behavior in active power behavior in Fig. 3.10 is more pronounced than in Fig. 3.6, Fig. 3.11 again shows the main difference between setpoint control and full control; the ability to control the reactive power demand independent of the active power demand. We also observe a large initial transient behavior from the AL load in both Fig. 3.6 and Fig. 3.11 when the malicious feedback controller is initially activated.

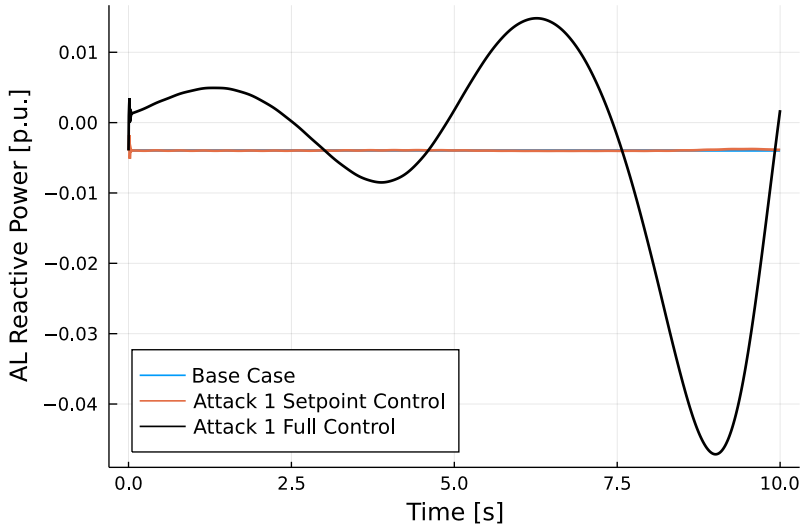

Figure 3.7: Time series of AL reactive power for both setpoint control and full control for attack 1.

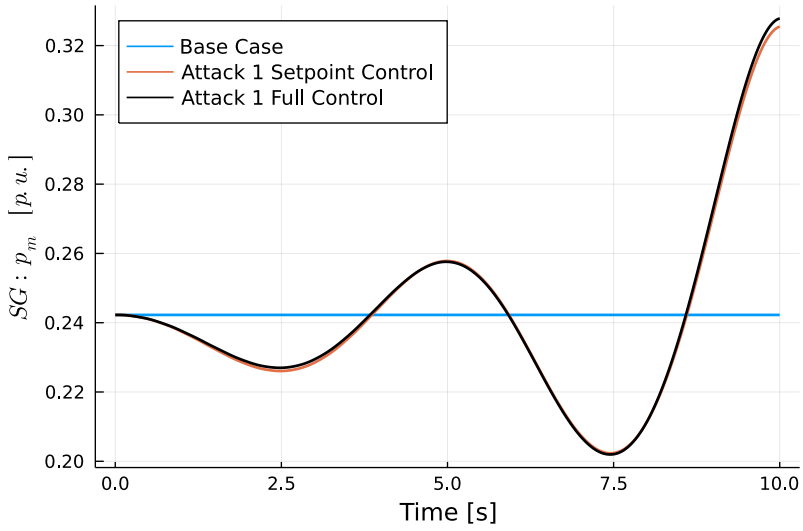

Figure 3.8: Time series of synchronous machine mechanical power, p_m, for attack 1.

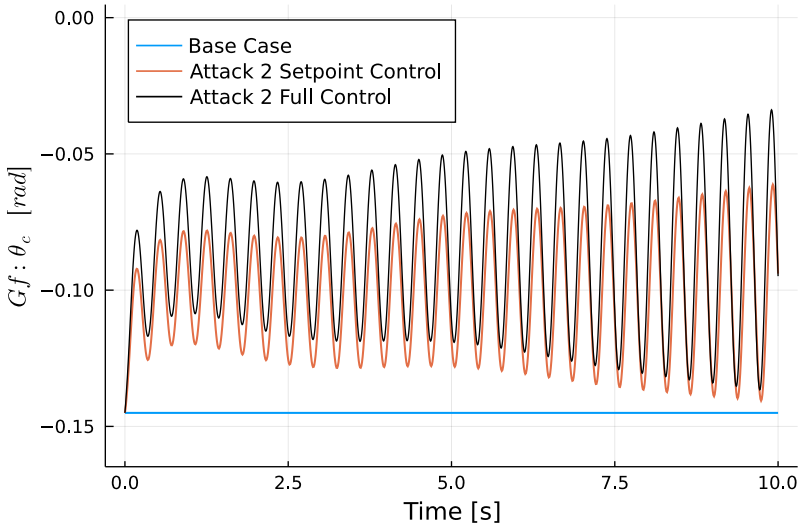

Figure 3.9: Time series behavior of the angle of Gf converter active power controller for attack 2.

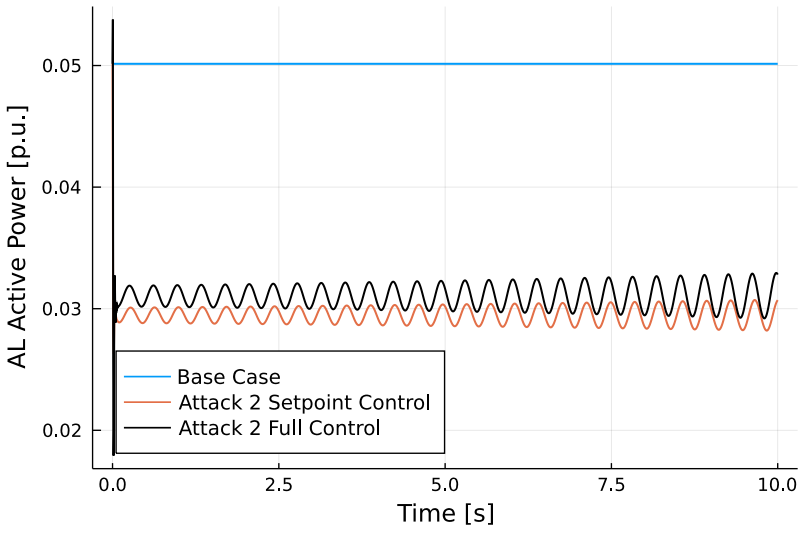

Figure 3.10: Time series of AL active power for both setpoint control and full control for attack 2.

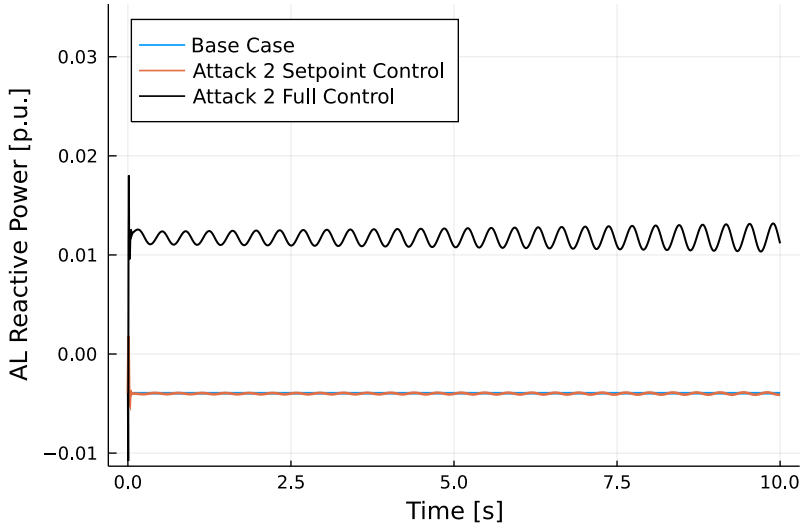

Figure 3.11: Time series of AL reactive power for both setpoint control and full control for attack 2.

3.5 Conclusions

Within this work, we sought to examine the vulnerability of mixed-source microgrids, with high converter penetration, to cyber-physical attacks through manipulation of an active load. For the specific controller design considered, the analysis represented a worst-case scenario for the operator. We assumed the adversary had access to both a model of the system as well as state measurements, or sufficient observability to reconstruct the state, for state-feedback. For the two levels of AL access assumed, setpoint control vs full control, we observed similar behavior for attack 1, the electromechanical instability, but more pronounced differences for attack 2, the electromagnetic instability.

Future work will consider more advanced adversarial de-stabilizing controllers to continue to build-up a library of attacks to better inform defensive mechanisms. Additionally we will consider how the mode of converter operation, i.e. grid following/forming, affects the cyber-physical security resiliency of a mixed-source microgrid as well as how these systems can be hardened, e.g. online adaptive parameterization of controllers.

3.6 Appendix

Theorem 1 *Let $\{\lambda_i, ..\lambda_n\}$ be a self conjugate set of complex numbers. There exists a feedback matrix F such that $(A + BF)v_i = \lambda_i v_i$ if and only if the following conditions are satisfied for all $i \in n$*

1. *the set of vectors v_i form a linearly independent basis in $\mathbb{C}^n$*
2. *$v_i = v_j^*$ whenever $\lambda_i = \lambda_j^*$*
3. *$v_i \in$ span$\{N_{\lambda_i}\}$*

If F exists, and B has full column rank, then F is unique[73].

Chapter 4

Outer-loop Adaptive Control of Converter-Interfaced Generation for Cyber-Physical Security

This chapter was co-authored with Daniel Arnold, a research scientist at LBNL, and Prof. Duncan Callaway, Associate Professor of Energy and Resources at the University of California, Berkeley. The text was previously published at the 2022 Hawaii International Conference on System Sciences (HICSS); see [84] for the full citation. The text has been reformatted for inclusion in this dissertation.

Abstract

The integration of converter-interfaced generation into our power systems is changing how we control and operate these networks. While these fast-acting resources are more controllable than conventional synchronous machines, this additional controllability presents some challenges. One of these challenges is the increased cyber-physical attack surface arising from interactions among the numerous digital control loops of these devices. In this work, we present a supervisory adaptive controller that temporarily increases the outer-loop controller bandwidth of these devices in the event of sustained oscillatory behavior. We design this controller to inherently remain inactive during normal operation and only become active during sustained abnormal operating conditions. We show how this proposed controller can mitigate a cyber-physical attack, even when the attacker has full knowledge of the network model and access to real-time state information for state-feedback control.

4.1 Introduction

As our power systems shift from centralized synchronous machine-based systems to more geographically dispersed CIG networks, the stability properties and dynamical response of these systems are also changing. These fast-acting power electronic connected resources,

and their multiple layered digital control loops, have a significantly larger control bandwidth relative to conventional synchronous machines [42]. This increase in controllability allows us greater flexibility in shaping the dynamical response of these resources. However, it also brings new challenges and vulnerabilities, for example, in cyber-physical security [89].

Traditionally, cyber-physical security for power systems has been primarily focused on protecting individual devices against attacks by securing communication channels, ensuring data integrity, and restricting access, both physical and remote, to these devices. While these approaches are critical, they are not exhaustive. These devices are connected through a dynamical network which can result in unexpected controller coupling, particularly with CIG [21]. This unexpected dynamic controller coupling can be coincidental or can result from malicious control of a device by an adversary.

Malicious control of dynamical devices in power systems is a research area which has received some attention over the years. Some of the early work in this space studied the potential for a malicious actor to control a subset of synchronous generators to destabilize other generators on the system [26, 27]. This work was motivated by considering the potential competitive advantage of such an approach in a market environment. More recent work examined how an aggregation of loads providing emulated inertia as a system service might be maliciously controlled to cause unstable oscillatory modes in the system [14]. Similarly, the introduction of electric vehicles, and manipulation of their charging behavior, has also been considered as a destabilizing resource in [2]. Other works have considered discrete switching loads and how they may be maliciously controlled [38, 108, 39]. In each of these cases, the resource under the control of the adversary was being controlled to cause an electromechanical instability, i.e., the adversary was causing synchronous machines to oscillate against each other.

The continual integration of CIG into our networks requires a revisiting of these types of malicious attacks. These resources are introducing new dynamical modes into the system that are currently significantly less well understood [21] and invalidating classical timescale separation assumptions we have used to understand these systems [68]. These new modes have been observed as abnormal sustained oscillations in weak grid conditions [21] and have been shown to be vulnerable to attack at high CIG penetration, assuming sufficient knowledge of the system [85].

In this work, we consider an isolated microgrid where an adversary controls an active load, i.e., a load connected to the grid through power electronics. These loads introduce additional dynamics into the system that can destabilize an otherwise stable network [13]. We adapt the attack vector from [85] and target the CIG by destabilizing an electromagnetic mode in which the CIG participates. We propose a local supervisory controller that observes the states of the CIG and adaptively changes the control logic of the converter to desensitize it against the malicious attack while continuing to deliver its normal grid services. Specifically, we adaptively increase the filter frequency of the low-pass filter in the CIG outer-loop control block. This rate of increase is sampled from a pre-defined normal distribution and, consequently, helps mitigate the adversarial attack by invalidating any

deterministic state-space model used to design the destabilizing controller. The proposed controller is designed to inherently remain inactive during normal operation and only alter the converters control logic in the event of sustained abnormal oscillatory behavior. Similar approaches have already been shown to mitigate oscillatory behavior due to poorly designed distributed energy resources (DER) volt-var droop curves [8]. In this work we focus on a much more severe attack where we assume the adversary has access to both a system model and real-time state information to carry out their attack. We show how our proposed controller can introduce a minimal amount of stochastic behavior to invalidate the state-space model used by the attacker, and ultimately, mitigate the impact of the attack.

4.2 Methodology

Prior to introducing the proposed defensive controller in Section 4.2, we first begin with a brief overview of the attack model. Understanding the attack methodology of the adversary, and how they develop a destabilizing controller, is necessary to motivate the formulation of the proposed defensive controller.

Attack model

Our model of the adversary follows the approach of [85] and is summarized here. We assume that the adversary has access to both 1) a detailed model of the system and 2) real-time state information to build a state-feedback controller. During the attack, this real-time state information can come directly from measurements or can be estimated using a state-observer, assuming sufficient observability of the system, i.e., the adversary has access to high-rate current and voltage data.

Under these assumptions, the goal of the adversary is to design a destabilizing state-feedback controller such that an eigenvalue of the linearized state-space model is in the right-half plane, i.e., the system is unstable. That is, given a linearized model of the system in (4.1)

$$\Delta\dot{x} = A\Delta x + B\Delta u, \tag{4.1}$$

the adversary seeks to design a controller of the form $u = -F\Delta x$ such that the closed loop system in (4.2) has at least one eigenvalue whose real part is positive.

$$\Delta\dot{x} = (A - BF)\Delta x \tag{4.2}$$

Additionally, we assume the adversary minimizes its own participation in this unstable mode. Simply put, the adversary seeks to excite the system to cause other devices on the grid to oscillate against each other. The measure of participation of a state i in a system mode j is given by (4.3)

$$p_{ij} = \frac{w_{ij} v_{ij}}{w_j^T v_j}, \tag{4.3}$$

where w_{ij} and v_{ij} are the i^{th} elements in the left and right eigenvector respectively associated with the j^{th} eigenvalue. This adversarial destabilizing controller design is mathematically expressed in (4.4) and admits a closed form solution [85]:

$$\min_{F} \quad \sum p_{ij} \quad \forall i \in \Gamma \tag{4.4a}$$

$$\text{s.t.} \quad \exists \quad \Re(\lambda_j) > 0 \tag{4.4b}$$

$$(A - BF)v_j = \lambda_j v_j \tag{4.4c}$$

where v_j is the eigenvector associated with λ_j and Γ denotes the set of states indices for the active load under control of the adversary. This closed form solution is summarized in Appendix A for the reader. In [85], the authors identified both an electromechanical and electromagnetic mode that the adversary could seek to destabilize. In this work, we focus on the attack that destabilizes the electromagnetic mode, as this is the most damaging attack for CIG.

The proposed attack model assumes a significant level of system knowledge to carry-out. An alternative attack model is a data-driven approach that estimates vulnerable system modes based on measurement data during disturbances [38, 39], e.g., measurement data during faults. The adversary then designs a local controller to try to destabilize these estimated modes. In both cases, model-based or measurement-based, the adversary seeks to design a destabilizing controller based on their understanding of the system. Our proposed approach is motivated by invalidating their understanding of the system during sustained abnormal oscillatory behavior. Therefore, the proposed controller is not tailored to mitigate the specific attack vector considered here, but rather any attack vector that relies on a fixed understanding of the system. Due to the stochastic nature of our controller, designed to remain inactive during inherent system transients, the proposed approach will remain effective in mitigating the severity of the attack for both model and measurement-based attacks.

Defensive controller

One commonality across all prior work that has considered destabilizing adversarial attacks is the requirement of a deterministic state-space model to build a state-feedback controller [85, 27, 14, 2]. This state-space model allows the adversary to identify vulnerable system modes to destabilize with state-feedback control. As a last line of defense against these types of attacks, we propose a non-linear supervisory controller that introduces a small amount of stochastic behavior into the system to invalidate the state-space model the adversary used in its controller design. This controller, in (4.5), is designed to inherently remain inactive during normal operation and only become activated during sustained abnormal oscillatory

behavior. Therefore, the CIG will respond as expected to normal grid disturbances, e.g., faults, line trips and frequency events.

The proposed controller uses an observer, shown in Fig. 4.1, to estimate the energy of the observed oscillation, similar to [8]. It monitors the integrator state of the PLL, ε, and uses a high-pass filter in (4.5a) to remove any DC offset, or low-frequency behavior, in the signal. We choose the integrator state of the PLL based on analysis in [85] and due to the PLL being identified as being a major cause of instability in real-world observed oscillations [21]. Once the low frequency behavior has been removed, we multiply the resultant signal, ε_h, by a normalization constant, c, then square it and pass it through a low-pass filter in (4.5b) to obtain a stable control signal. This low-pass filter also desensitizes the proposed controller to naturally occurring system transients, e.g., faults and line trips. By first removing the low-frequency content and then squaring the signal, we are estimating the energy of the oscillation in the PLL integrator state, ε. We then use this measure of energy to increase the outer-control loop filter frequency, ω_z, in (4.5c) where $\alpha \sim \mathcal{N}(\mu, \sigma^2)$.

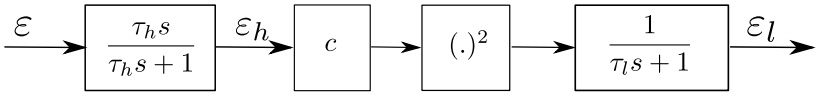

Figure 4.1: Estimating energy of oscillation.

$$\dot{\varepsilon}_h = \frac{\tau_h \dot{\varepsilon} - \varepsilon_h}{\tau_h} \tag{4.5a}$$

$$\dot{\varepsilon}_l = \frac{(c\varepsilon_h)^2 - \varepsilon_l}{\tau_l} \tag{4.5b}$$

$$\dot{\omega}_z = \omega_z^\star - \omega_z + \alpha\varepsilon_l \tag{4.5c}$$

This proposed controller runs continuously on the CIG. It is not threshold activated but instead uses the high- and low-pass filters to reject normally occurring disturbances on the external grid.

As previously discussed, this filter frequency, ω_z, determines the bandwidth of the outer-control loops of the CIG. By temporarily increasing the controller bandwidth of the outer-loop, we are breaking any controller coupling that the adversary is seeking to exploit. The structure of (4.5c) also ensures that when the oscillation is mitigated, the filter frequency returns to its normal operating point, $\omega_z^\star$. The stochastic nature of α, not remotely accessible via communication and updated at a low frequency, e.g., seconds or minutes, ensures that the adversary never has access to a deterministic state-space model to build a state-feedback controller.

Fig. 4.2 shows how increasing the outer-loop bandwidth can temporarily move a pair of system eigenvalues, and consequently, mitigate any attack that specifically targets these eigenvalues based on a model or measurement data. The specific eigenvalues highlighted

in Fig. 4.2 have high state-participation from both the PLL and outer-loop controls and can move towards the right-half plane during weak grid conditions and/or because of inter-IBR controller coupling.

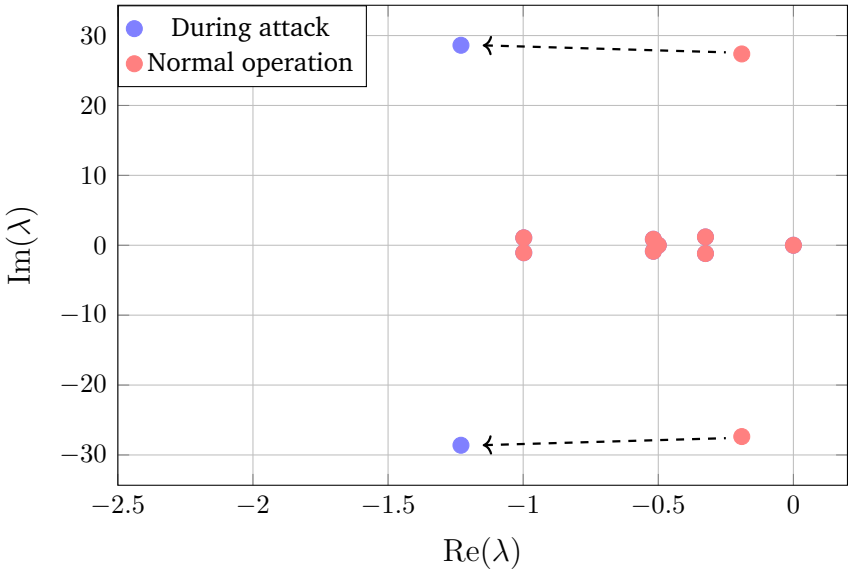

Figure 4.2: Changing eigenspectrum during attack

The proposed adaptive control loop, shown in Fig. 4.3, should be parameterized to ensure sufficient timescale separation between the proposed controller and existing control loops of the CIG. This will help ensure that the controller does not increase the oscillations during the attacks considered here.

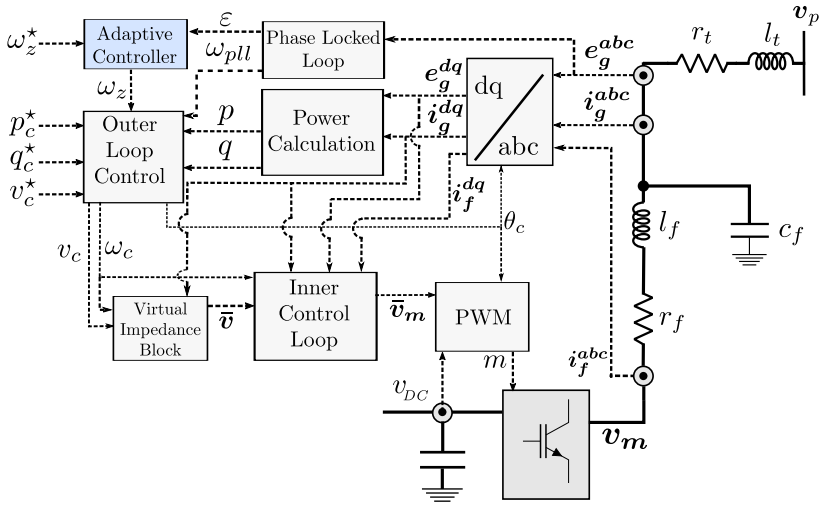

Figure 4.3: Grid-following control structure with proposed control loop

4.3 Power System Models

We consider a CIG plant, in Fig. 4.4, with its active power controller operating in grid-following mode and its reactive power controller in droop mode. Grid-following mode is commonly associated with real-world recorded oscillatory behavior when operating under weak grid conditions, primarily due to the PLL [21].

All control loops in Fig. 4.4 operate in the dq frame, which is achieved by a linear transformation, T_{dq} in (4.6), from the 3-phase instantaneous voltage and current values, where θ_c is an internal state of the converter, discussed in Section 4.3.

$$T_{dq} = \sqrt{\frac{2}{3}} \begin{bmatrix} \cos(\theta_c) & \cos(\theta_c - 2\pi/3) & \cos(\theta_c + 2\pi/3) \\ \sin(\theta_c) & \sin(\theta_c - 2\pi/3) & \sin(\theta_c + 2\pi/3) \end{bmatrix} \tag{4.6}$$

In this work, our analysis will be carried out in the dq reference frame. We denote complex vectors using bold lowercase symbols as in (4.7).

$$x = x^{dq} = x^d + jx^q \tag{4.7}$$

Electrical Interface and Power Calculation

The CIG is interfaced to the grid in Fig. 4.4 through an RLC filter (r_f, l_f, c_f) for harmonic filtering, and a transformer, with resistance and inductance r_t and l_t respectively. The differential equations describing its electrical variables are given by (4.8):

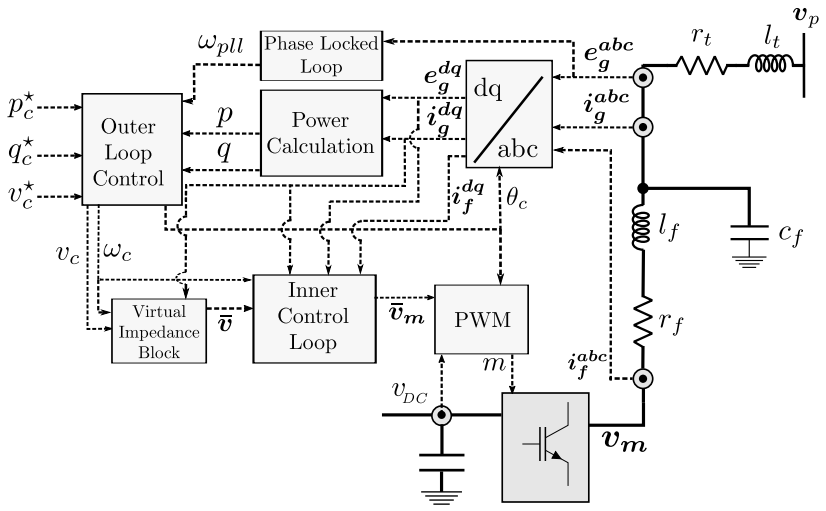

Figure 4.4: Grid-following control structure

$$\dot{i}_f = \frac{\omega_b}{l_f}(v_m - e_g) - \left(\frac{r_f}{l_f}\omega_b + j\omega_b\omega_c\right) i_f \tag{4.8a}$$

$$\dot{i}_g = \frac{\omega_b}{l_t}(e_g - v_p) - \left(\frac{r_t}{l_t}\omega_b + j\omega_b\omega_c\right) i_g \tag{4.8b}$$

$$\dot{e}_g = \frac{\omega_b}{c_f}(i_f - i_g) - j\omega_c\omega_b e_g \tag{4.8c}$$

where i_f is the current through the filter inductance, i_g is the current injected into the grid, e_g is the voltage across the filter capacitance, v_m is the modulated voltage at the terminals of the CIG, v_p is the voltage at the point-of-connection to the grid, ω_c is the frequency of the internal SRF in per-unit (p.u.) and ω_b is the base system frequency. The converter active and reactive power is then calculated from (4.9):

$$p_c = \Re(e_g i_g^\star) \qquad q_c = \Im(e_g i_g^\star) \tag{4.9}$$

where $i_g^\star$ denotes the complex conjugate of the current vector, and $\Re(.)$ and $\Im(.)$ are the real and imaginary part respectively. These active and reactive power measurements, along with the estimated system frequency from the PLL, are then passed into the outer-loop control block.

Phase-lock loop

The purpose of the PLL is to track the frequency and phase of the externally measured grid voltage. It does so by aligning the $d-$axis of the internal SRF with the externally measured

voltage vector, resulting in its $q-$ vector component of the internal SRF being equal to zero. Its dynamics are given by (4.10):

$$\hat{e}_g = e_g e^{-j\theta_{pll}} \tag{4.10a}$$
$$\dot{\theta}_{pll} = \omega_{pll}\omega_b \tag{4.10b}$$
$$\dot{\varepsilon} = \hat{e}_g^q \tag{4.10c}$$
$$\omega_{pll} = \omega_0 + K_p^{pll}\hat{e}_g^q + K_i^{pll}\varepsilon \tag{4.10d}$$

where ε is the integrator state of the PLL, ω_{pll} is the estimated frequency, and K_p^{pll} and K_i^{pll} are the proportional and integral gains respectively of the PI control loop in (4.10d). One difficulty with parameterizing the control gains of a PLL is the requirement that it produces an accurate and stable estimation of the grid-frequency across all grid operating conditions, i.e., a weak and strong grid, while also not being overly sensitive to natural grid-disturbances, e.g., faults. This is one of the reasons why the PLL is often identified as one of the contributors to undesirable oscillatory behavior [21].

Outer-loop control

Once the PLL estimates the grid frequency, ω_{pll} in (4.10d), this estimation is passed to the outer-control loop. This control loop is responsible for determining control set-points to achieve a desired active and reactive power injection. It is typically one of the slower control loops of the CIG and can also contribute to undesirable oscillatory behavior [21]. Within the outer-control loop, the CIG first low-pass filters the measured active and reactive power in (4.11a) and (4.12a) respectively. The filter frequency, ω_z, determines the bandwidth of the outer-loops. In this work, we will consider ω_z as a state within our supervisory controller and adjust it to change the outer-loop control bandwidth of the CIG during sustained abnormal behavior. The specific control structure to achieve this will be introduced in Section 4.2.

$$\dot{\tilde{p}}_c = \omega_z(p_c - \tilde{p}_c) \tag{4.11a}$$
$$\omega_c = \omega_{pll} + R_p(p_c^\star - \tilde{p}_c) \tag{4.11b}$$
$$\dot{\theta}_c = \omega_c\omega_b \tag{4.11c}$$

The output of these low-pass filters, $\tilde{p}$ and $\tilde{q}$, are then used to determine the control set-points ω_c and v_c in (4.11b) and (4.12b) respectively, where R_p and R_q are the active and reactive power droop gains respectively.

$$\dot{\tilde{q}}_c = \omega_z(q_c - \tilde{q}_c) \tag{4.12a}$$

$$v_c = v_c^\star + R_q(q_c^\star - \tilde{q}_c) \tag{4.12b}$$

The angular frequency, ω_c, also determines the angle θ_c, in (4.11c), for the linear transformation, T_{dq} in (4.6).

Virtual Impedance

These outer-loop control set-points are then passed to the virtual impedance control block in Fig. 4.4, with a virtual resistance and inductance, r_v and l_v respectively. This additional degree of freedom is used for active stabilization and disturbance rejection [107].

$$\bar{v}_c^d = v_c - r_v i_g^d + \omega_c l_v i_g^q \tag{4.13a}$$
$$\bar{v}_c^q = -r_v i_g^q - \omega_c l_v i_g^d \tag{4.13b}$$

Additionally, the use of a virtual impedance can increase the apparent X/R ratio of the network and improve the small-signal stability of the system by strengthening the p/f and q/v coupling of the system.

Inner control loop

Finally, a dual-loop PI controller is used in the inner-loop for reference tracking. The output of the virtual impedance control block, $\bar{v}_c$ is first passed to a PI voltage controller in (4.14)

$$\bar{i}_f = K_p^v(\bar{v}_c - e_g) + K_i^v \xi + j\omega_c c_f e_g + K_f^v i_g \tag{4.14a}$$
$$\dot{\xi} = \bar{v}_c - e_g \tag{4.14b}$$

whose output, $\bar{i}_s$, is then passed into another PI control loop, in (4.15), to determine the output voltage reference used for the averaged modulated signal.

$$\bar{v}_m = K_p^i(\bar{i}_f - i_f) + K_i^i \gamma + j\omega_c c_f i_f + K_f^i e_g \tag{4.15a}$$
$$\dot{\gamma} = \bar{i}_f - i_f \tag{4.15b}$$

In both (4.14) and (4.15), the controller gains K_p^v/K_p^i and K_i^v/K_i^i are the proportional and integral gains of the PI loop respectively and K_f^v/K_f^i is a binary feed-forward term.

4.4 Results

To demonstrate the effectiveness of the proposed controller we consider the 3-bus microgrid in Fig. 4.5. This system has a SG, a Gfl converter, an AL and a constant impedance load.

The adversary has control over the active load and designs a state-feedback controller for modulating active and reactive power demand to cause the system to become unstable. The parameters of the synchronous-machine and grid-following converter are from [67] and the details of the AL and the destabilizing adversarial controller can be found in [85]. The steady-state active and reactive power operating conditions are summarized in Table 4.1.

Table 4.1: Steady-state operating conditions.

	P [p.u.]	Q [p.u.]
SG	0.32	0.14
Gf	0.70	0.12
AL	0.05	0.0
rl load	0.97	0.11

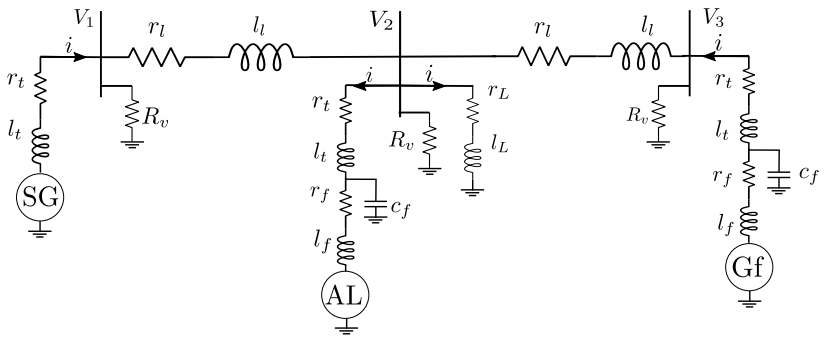

Figure 4.5: Three-bus mixed source microgrid

The proposed defensive controller from Section 4.2, with experimental parameters in Table 4.2, is deployed on the grid-following converter and monitors the integrator state of the PLL.

Table 4.2: Supervisory Controller Parameters.

τ_h	τ_l	c	μ	σ
0.795	0.159	1×10^4	15	2

Fig. 4.6 shows the active power injection from the grid-following converter in the case of no attack and during an attack with and without the proposed supervisory controller. Without the proposed controller, we see that the CIG is exhibiting unstable oscillatory behavior. With the proposed supervisory controller, however, we see that the unstable behavior is mitigated within seconds following its onset.

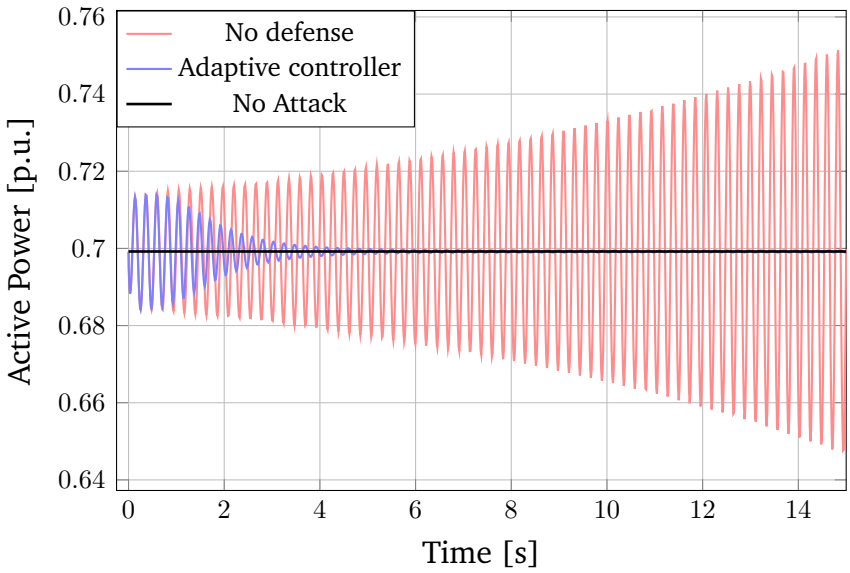

Figure 4.6: Grid-following converter active power

Contrasting the active and reactive power demand from the adversary controlled active load in Fig. 4.7 to the oscillatory active power injection from the grid-following converter in Fig. 4.6, we see that the adversary has exerted minimal observable control effort to destabilize the system. The amplitude of its load modulation is under 2% of the total microgrid load. This level of load modulation is consistent with prior work on adversarial load control for destabilizing electromechanical modes on the transmission grid [14]. Additionally, this load oscillatory amplitude is significantly smaller than the amplitude of the oscillatory behavior in the active power behavior of the CIG in Fig. 4.6. This additional oscillatory active power from the CIG is being absorbed primarily by the constant impedance, due to oscillations in the nodal voltages, and the synchronous machine.

To understand the behavior of the supervisory defensive controller we examine the behavior of both the observer, for estimating the energy of the oscillation, and the filter frequency ω_z. Fig. 4.8 plots the time-series of ε_l, the output of a low-pass filter from (4.5b). Initially, we see relatively large values for ε_l as the amplitude of the oscillations grow in Fig. 4.6. With the inclusion of the proposed controller, we see these oscillations decay until they settle around constant oscillatory amplitude.

This filtered signal, ε_l, in Fig. 4.8 is a stable control signal that is then used to adaptively increase the outer-loop filter frequency, as shown in Fig. 4.9.

The filter-frequency, ω_z, is only marginally increased in this case to mitigate the attack. This helps limit the randomness introduced by the defensive controller and ensures that, even during a sustained adversarial load attack, the CIG exhibits largely deterministic behavior. Additionally, we see that once the oscillatory amplitude in Fig. 4.6 decays, ω_z tends back towards its set-point, $\omega_z^\star$, in Fig. 4.9. Once the adversarial controller is deactivated, ei-

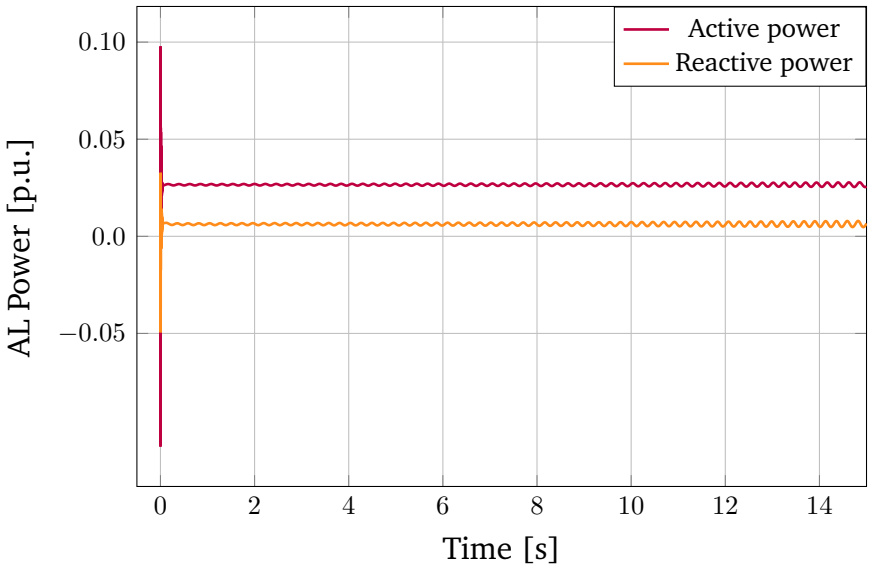

Figure 4.7: Adversary load power

ther by the adversary themselves or a higher-level intrusion detection scheme, the proposed controller ensures that ω_z returns to its normal operating value, $\omega_z^\star$.

In this work, we demonstrated our proposed controller on a simple 3-bus microgrid. Recent analysis has shown how electrically close CIG can adversely interact with each other in larger systems [34]. This presents an alternative attack vector for adversaries to destabilize local CIG. Future work will examine how the proposed controller performs under such an attack.

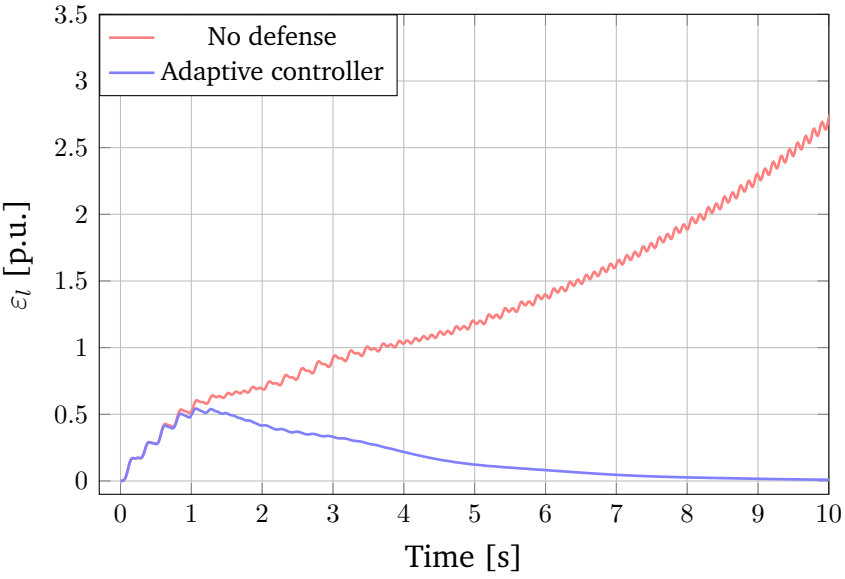

Figure 4.8: ε_l time series during attack

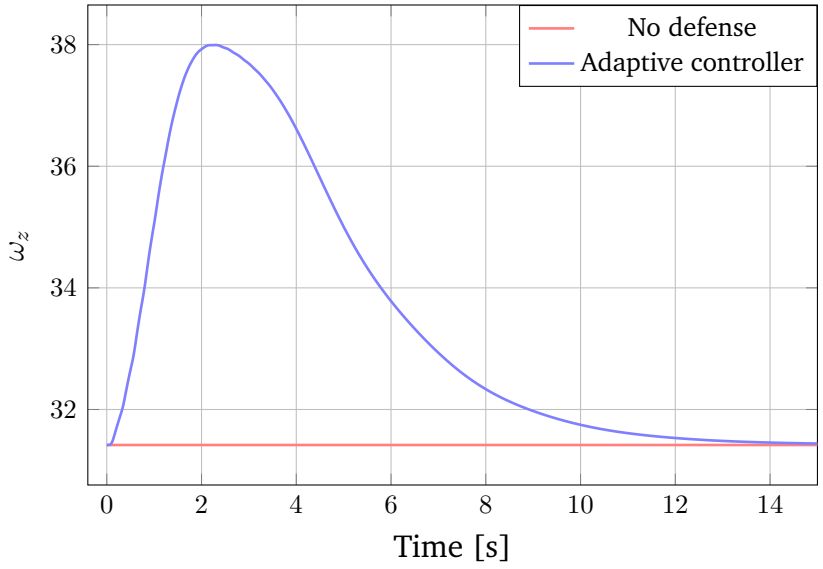

Figure 4.9: Time series of ω_z during attack

4.5 Conclusions

In this work we presented a local supervisory controller designed to be the last line of defense against a destabilizing cyber-physical attack against CIG within a micro-grid. This defensive controller was designed to stochastically increase the outer-loop bandwidth of the CIG to invalidate any deterministic state-space model that an adversary may have used to design their attack. A key design feature of the proposed controller is that is does not impede normal operation of the CIG and is only activated in the event of sustained oscillatory behavior.

With the continual proliferation of microgrids, coupled with the control complexity of the CIG, the attack surface of these systems is increasing [89]. Hardening these systems against adversarial attacks, both direct and indirect, will require a cross-disciplinary approach with multiple fail-safe systems. This work was a first step at designing a last line of defense that would allow the CIG to remain online and delivering its required grid services while protecting itself against a targeted attack. The hope is that this last line of defense would mitigate any adverse physical impacts of the attack, e.g., damaging equipment, as well as allow operators and/or other defensive layers additional time to respond.

Further work is required to further analyze, and test, the proposed controller and its stability properties to guarantee its satisfactory performance. Additionally, we will consider the effectiveness of the proposed controller under different attack models, including attacks that attempt to be robust with respect to uncertainties in the system model. These more sophisticated attacks may require adjusts to the proposed controller, e.g., saturating the value of the filter frequency, ω_z, to ensure that the proposed controller does not increase the bandwidth of the outer-loop such that it adversely interacts with the inner-control loop.

4.6 Appendix A

We assume the adversary has a linear state-space model of the form

$$\Delta\dot{x} = A\Delta x + B\Delta u, \tag{4.16}$$

with $x \in \mathbb{R}^n$, $A \in \mathbb{R}^{n\times n}$, $B \in \mathbb{R}^{n\times m}$ and $u \in \mathbb{R}^m$. To design a destabilizing feedback controller, we first identify a suitable mode of the linearized matrix A to destabilize. Following this, we seek to design a feedback controller that achieves a desired closed-loop unstable eigenvalue $\hat{\lambda}$. In addition to meeting the eigenvalue specification criteria, we seek to design the corresponding eigenvector $\hat{v}$ to minimize the participation of the states of the control group in the unstable mode. To achieve this, we seek to design an eigenvector $\hat{v}$ that maximizes the participation of the target group (relative to the control group) in the unstable mode. We then begin by constructing the corresponding Hautus matrix $S_{\hat{\lambda}}$ given by (4.17)

$$S_{\hat{\lambda}} = [(\hat{\lambda}I - A) \quad B] \tag{4.17}$$

where I is the identity matrix. We then determine the matrix $K_{\hat{\lambda}}$ of the form

$$K_{\hat{\lambda}} = \begin{bmatrix} N_{\hat{\lambda}} \\ M_{\hat{\lambda}} \end{bmatrix}, \tag{4.18}$$

whose columns form a basis for nullspace of $S_{\hat{\lambda}}$. Note that the rows of $K_{\hat{\lambda}} \in \mathbb{R}^{(n+m)\times m}$ are partitioned in a similar manner to the columns of $S_{\hat{\lambda}}$, i.e. $N_{\hat{\lambda}} \in \mathbb{R}^{n\times m}$ and $M_{\hat{\lambda}} \in \mathbb{R}^{m\times m}$. The dimension, m, of the input vector, u, will determine the dimension of the nullspace and consequently the degree of flexibility in designing the eigenvector $\hat{v}$, expressed as

$$\hat{v} = N_{\hat{\lambda}} k \tag{4.19}$$

for some $k \in \mathbb{R}^{m\times 1}$. The i^{th} entry of $\hat{v}$, therefore, is given by

$$\hat{v}_i = \sum_{j=1}^{m} [N_{\hat{\lambda}}]_{i,j} k_j. \tag{4.20}$$

Here, we let $N_{\hat{\lambda}T}$ and $N_{\hat{\lambda}C}$ denote the rows of $N_{\hat{\lambda}}$ whose indices correspond to the states of the target and control group, respectively. The target group represents the states of the devices we wish to destabilize while the control group is the set of states under the control of the adversary. We then seek to determine the optimal design vector $k^\star$ for maximizing the ratio of ℓ_2-norm of the eigenvector entries corresponding to the target states and the ℓ_2-norm of the eigenvector entries corresponding to the control group. Similar to [27], we mathematically express this optimization problem as

$$\begin{aligned} \max_{k} \quad & \frac{k'[N_{\hat{\lambda}T}]' N_{\hat{\lambda}T} k}{k'[N_{\hat{\lambda}C}]' N_{\hat{\lambda}C} k} \\ \text{s.t.} \quad & k'k = 1, \end{aligned} \tag{4.21}$$

where $[.]'$ denotes the transpose operator. Defining the matrices G and H as

$$G = [N_{\hat{\lambda}T}]' N_{\hat{\lambda}T} \quad H = [N_{\hat{\lambda}C}]' N_{\hat{\lambda}C}, \tag{4.22}$$

we rewrite this optimization as

$$\begin{aligned} \max_{k} \quad & \frac{k'Gk}{k'Hk} \\ \text{s.t.} \quad & k'k = 1. \end{aligned} \tag{4.23}$$

Note that we assume that the matrix H is positive definite. Otherwise, we could choose the optimal design vector $k^\star$ such that the control group would have zero participation in the unstable mode, i.e. $N_{\hat{\lambda}C} k^\star = 0$, which would be the best case for the adversary.

Having H as positive definite, we can safely assume that it has a well-defined square root. We now introduce a linear transformation given by

$$k = H^{-1/2}\nu, \tag{4.24}$$

and substitute this into (4.23), which yields

$$\max_{\nu} \frac{\nu'(H^{-1/2})^T G H^{-1/2}\nu}{\nu'\nu}. \tag{4.25}$$

Note that (4.25) takes the form of the Rayleigh quotient and is therefore easily solvable. The optimal design vector $k^\star$ is constructed using the eigenvector ν_{max} corresponding to the largest eigenvalue of (4.25), and is given by

$$k^\star = H^{-1/2}\nu_{max}. \tag{4.26}$$

We then construct the destabilizing feedback matrix F as follows. Let us define the vectors $\hat{w}$ and $\hat{w}$ in (4.27).

$$\hat{w} = M_{\hat{\lambda}}k^\star\,,\ \hat{v} = N_{\hat{\lambda}}k^\star, \tag{4.27}$$

and construct the real matrices W and V of the form

$$W = [Re\{\hat{w}\}\, Im\{\hat{w}\}\, 0\ \ldots\ 0], \tag{4.28a}$$

$$V = [Re\{\hat{v}\}\, Im\{\hat{v}\}\, Re\{v_3\}\, Im\{v_3\}\ \ldots\ v_{n-1}\, v_n], \tag{4.28b}$$

where $[v_3, ...v_{n-1}, v_n]$ are the remaining original eigenvectors from the state-space matrix A given in (4.16). The feedback matrix F is then given by

$$F = WV^{-1}. \tag{4.29}$$

Provided that the columns in (4.28b) are linearly independent, the matrix F given by (4.29) exists and is unique [73].

Chapter 5

An Online Adaptive Damping Controller for Converter-Interfaced Generation

This chapter was co-authored with Daniel Arnold, a research scientist at LBNL, and Prof. Duncan Callaway, Associate Professor of Energy and Resources at the University of California, Berkeley. The text has been reformatted for inclusion in this dissertation.

Abstract

The increasing integration of converter-interfaced generation within large-scale synchronous power systems is presenting both new challenges and opportunities in how we operate these dynamical networks. One of these challenges is designing and parameterizing the digital control loops that dictate the dynamical behavior of these fast-acting resources. Improperly tuned gains, or unexpected controller couplings through the network, can lead to poorly damped oscillations during disturbance conditions and/or decrease the system stability margin. Within this work, we present an approach for adaptively tuning a damping controller to improve the dynamic response of converter-interfaced generation, based only on local measurements. We show that, with low-amplitude probing, we can identify a subset set of observable system modes. We then propose a linear single input single output (SISO) state-feedback controller to improve the damping ratio and stability margin of the system. We show the effectiveness of the proposed controller through both eigenvalue analysis and time-domain simulations. We first demonstrate the proposed approach on a simple 3-bus system followed by a larger test case, the IEEE 14 bus system, with multiple devices simultaneously probing the network.

5.1 Introduction

The increasing integration of CIG into synchronous power systems is changing the dynamical behavior of these systems. In contrast to synchronous machines, whose dynamical response is dominated by their inherent electromechanical physics, the dynamical response

of CIG is almost entirely dependent on fast-acting digital control loops. While these highly configurable resources provide new opportunities for control, they are also introducing new stability challenges that must be addressed [42], including the appearance of new oscillatory modes [34].

Understanding, and mitigating, oscillatory behavior in interconnected power systems is a well-studied and continually evolving area of research [55, 88]. Historically, these oscillatory modes were due to electromechanical interactions in the low frequency range (0.2 - 3 Hz) arising from the coupling of synchronous machines through the network [88]. Recently, however, new oscillatory modes have been observed on the grid as the penetration of CIG increases. Though these modes are poorly understood, they have been attributed to series capacitor sub-synchronous oscillations (SSO), weak grid SSO and inter-CIG interactions [21, 34], and they exhibit a much wider frequency range ($\approx$ 4 - 30 Hz in [21]) compared to electromechanical modes. One of the primary barriers to understanding these modes, and consequently mitigating their effects, is the lack of availability of sufficiently detailed industrial models of CIG[21].

PSSs are control blocks on synchronous machines that are used to damp electromechanical oscillatory modes and increase power transfer. PSSs modulate generator excitation to produce components of electrical torque in phase with rotor speed deviations, thereby improving the damping of the system. In systems dominated by synchronous machines, a PSS can be tuned using a combination of root locus and time domain simulations [7]. Recent efforts have explored the use of PSS-like controls to dampen CIG-induced oscillations. The authors in [70, 95] propose a centralized controller to coordinate distributed devices to improve the damping of observed modes. In [76], the authors propose a coordinated scheme to control both onshore CIG and offshore wind turbines that can be implemented in a locally decentralized architecture. Additionally, the authors in [30] utilize a pole-placement approach to tune the parameters of a damping controller using an assumed model of the rest of the system.

The challenge with these existing approaches is that they either require communication and co-ordination[70, 95], assume a fixed model and operating point of the external system[30] and/or are not scalable to large systems. As discussed in [21], there is little understanding of the cause of these modes, nor does there seem to be a consistent pattern across the system conditions under which they manifest. To overcome some of these limitations, the authors in [92] implement a purely data-driven local adaptive controller. They develop an online algorithm that monitors, detects, and mitigates subsynchronous oscillations using a shunt voltage source converter. While this approach is successful in damping oscillatory behavior across different frequencies in varying system conditions, it requires an additional shunt voltage source-converter and is reactionary, rather than preventative.

Within this work we propose an online adaptive damping controller for CIG to improve system damping. Our proposed controller only uses local (i.e., obtained at the point of common coupling between the controllable CIG and the grid) measurements and adaptively adjusts a linear state-feedback controller to increase the damping of locally observable

modes and system stability margins. The adjustment mechanism is facilitated by low-amplitude probing in the reactive power injection of controllable CIG. One of the primary causes of CIG-induced oscillatory behavior is weak system strength [21, 34], and its time varying nature makes it difficult to identify a fixed set of control gains to maintain system stability under a wide range of operating conditions. The adaptive parameter tuning approach detailed in this work overcomes this drawback by continually updating gains in a PSS-like damping controller as the system strength varies and/or unexpected controller coupling occurs. This approach is purely data-driven and does not require models of the system and/or nearby devices typically used in tuning PSS controls [7]. In so doing, the approach stands to substantially increase the robustness to disturbances in grids with high portions of CIG-based generation. The key contributions of this research are:

- The development of a method for determining a reduced-order model that captures the dominant modes of interaction between the external grid and the controllable CIG.
- The creation of an algorithm for online tuning of a PSS-like controller to improve the damping and stability margin of estimated modes.

Notation: Throughout the paper vectors are represented as bold lower-case symbols, matrices as bold uppercase symbols and learned/estimated quantities are denoted by the hat symbol, e.g., $\hat{x}$.

5.2 CIG Model

We adopt a grid-following inverter, depicted in Fig. 5.1, as the CIG model used in this analysis. This mode of operation is most associated with real-world oscillatory behavior[21] primarily due to the poor performance of the PLL when operating under weak grid conditions. The approached presented, however, is also applicable to other control schemes, e.g., virtual synchronous machines and droop controlled grid forming devices.

The controllers in Fig. 5.1 operate in the dq frame, which is achieved by a linear transformation, T_{dq} in (5.1), from the 3-phase instantaneous voltage and current values.

$$T_{dq} = \frac{2}{3}\begin{bmatrix} cos(\theta_{pll}) & cos(\theta_{pll} - \frac{2\pi}{3}) & cos(\theta_{pll} + \frac{2\pi}{3}) \\ sin(\theta_{pll}) & sin(\theta_{pll} - \frac{2\pi}{3}) & sin(\theta_{pll} + \frac{2\pi}{3}) \end{bmatrix} \tag{5.1}$$

where the angle, θ_{pll}, is a state of the PLL. The PLL determines this angle by aligning the $d-$axis of its internal synchronous rotating reference frame (SRF) with the locally measured grid voltage, i.e., when the $q-$axis voltage in the internal SRF equals zero. This is defined in (5.2)

$$\dot{v}^q_{pll} = \omega_p(v^q_g - v^q_{pll}) \tag{5.2a}$$

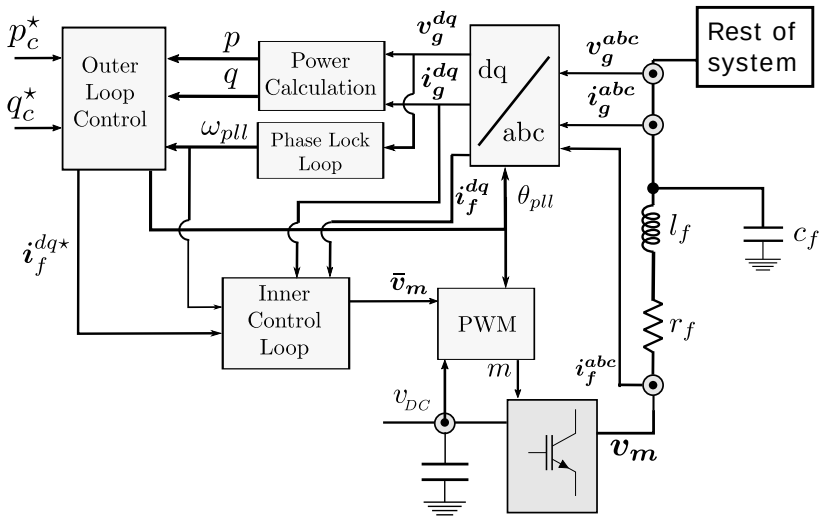

Figure 5.1: Control structure of a grid-following converter

$$\dot{\varepsilon}_{pll} = v_{pll}^q \tag{5.2b}$$
$$\dot{\theta}_{pll} = \omega_n + k_{pll}^p v_{pll}^q + k_{pll}^i \varepsilon_{pll} = \omega_{pll} \tag{5.2c}$$

where v_{pll}^q is a low-pass filtered estimation of the $q-$axis component of the voltage in the internal SRF of the CIG, ε is the integrator states of the PLL, ω_n is the nominal frequency, ω_p is a low-pass filter frequency, and k_{pll}^p and k_{pll}^i are the proportional and integral gain of the PLL respectively. The power calculation block then calculates the active and reactive power, p and q. These are then passed to the outer-control block where they are both low-pass filtered, in (5.3),

$$\dot{\tilde{p}} = \omega_z(p - \tilde{p}) \tag{5.3a}$$
$$\dot{\tilde{q}} = \omega_z(q - \tilde{q}) \tag{5.3b}$$

with a low-pass filter frequency, ω_z. These low-pass filtered measurements, $\tilde{p}$ and $\tilde{q}$, are then used for calculating the current reference set-points, $i_f^{dq\star}$, in (5.4),

$$\dot{\sigma_p} = p^\star - \tilde{p} \tag{5.4a}$$
$$\dot{\sigma_q} = q^\star - \tilde{q} \tag{5.4b}$$
$$i_f^{d\star} = k_{PQ}^p(p^\star - \tilde{p}) + k_{PQ}^i \sigma_p \tag{5.4c}$$
$$i_f^{q\star} = k_{PQ}^p(q^\star - \tilde{q}) + k_{PQ}^i \sigma_q \tag{5.4d}$$

where σ_p and σ_q are the integrator states for the active-power and reactive-power outer-loop respectively, $p^\star$ and $q^\star$ are the active power and reactive power set-points of the CIG

respectively, and k^p_{PQ} and k^i_{PQ} are the proportional and integral gains of the PI control loops respectively. Finally, these current set-points are passed to the inner-control loop that implements a PI structure, in (5.5), for tracking, where γ^{dq} are the integrator states, k^p_c and k^i_c are the proportional and integrator states respectively and k^f_c is a feed-forward term.

$$\dot{\gamma}^{dq} = i_f^{dq} - i_f^{dq\star} \tag{5.5a}$$

$$\bar{v}_m = k^i_c \gamma^{dq} + k^p_c (i_f^{dq} - i_f^{dq\star}) - j\omega_{pll} L_f i_f^{dq} + k^f_c v_g^{dq}. \tag{5.5b}$$

These cascaded control loops are intended to be tuned, and verified, against a model of the system[48] to ensure satisfactory performance. Once in operation, however, they can exhibit undesirable behavior as they unexpectedly interact with other CIG control loops and/or operating conditions vary[34]. This motivates the design of a damping controller than can be adaptively parameterized as a function of the external grid operating conditions.

5.3 Subspace Identification

The dynamical behavior of an interconnected power system is described by a set of nonlinear differential equations of the form (5.6)

$$\dot{\boldsymbol{x}} = \boldsymbol{f}(\boldsymbol{x}, \boldsymbol{u}), \tag{5.6}$$

where $\boldsymbol{x}$ and $\boldsymbol{u}$ correspond to the states and inputs respectively. To examine the small-signal stability of these systems, we linearize this system around an equilibrium point $(\boldsymbol{x}_{\text{eq}}, \boldsymbol{u}_{\text{eq}})$ to obtain a linear system of the form in (5.7):

$$\Delta\dot{\boldsymbol{x}} = \boldsymbol{A}\Delta\boldsymbol{x} + \boldsymbol{B}\Delta\boldsymbol{u}, \tag{5.7}$$

where $\Delta x = x - x_{eq}$, $\Delta u = u - u_{eq}$, $\Delta x \in \mathbb{R}^n$, $A \in \mathbb{R}^{n\times n}$, $B \in \mathbb{R}^{n\times m}$ and $\Delta u \in \mathbb{R}^m$. The eigenvalues of the matrix A in (5.7) can then be computed to understand the stability margin and damping of the modes of the system. This analysis is common for both controller tuning and understanding how different generator compositions, e.g., synchronous machines or CIG, affect the dynamics of the system.

The challenge with performing controller tuning using (5.7) is that it requires a full-order model of the system. To overcome this, prior work used system measurement data to build low-order models of the entire system[41, 50, 51]. These approaches assume access to real-time measurements across the network. In this work, we instead build a reduced-order model that captures the dynamical coupling between the individual CIG of interest and the rest of the system. To estimate this reduced-order model we inject a probing signal into the system and record the response of the local converter control states. Using this input-output data we can then estimate a subset of observable system modes. In

Section 5.4 we discuss how we average across experiments to reject external disturbances and focus on estimating observable modes that the CIG participates in. The participation of a particular state in each mode is estimated from the eigenvectors of the system. Given a linearized model of the form in (5.7), we denote by V and W the right and left eigenvector matrices of matrix A respectively, such that $\Lambda = W\,A\,V$, where Λ is a diagonal matrix whose diagonal entries are the eigenvalues of $\boldsymbol{A}$. Then the participation of state i in mode j can be defined as in (5.8)

$$p_{ij} = \frac{w_{ij}v_{ji}}{w_j^T v_j}, \tag{5.8}$$

where w_{ij} and v_{ji} are the elements of W and V respectively[90].

To estimate the observable modes in which the converter states participate we use subspace identification (SID) methods [65]. SID methods have been empirically shown to accurately estimate the system modes in the context of power system, including for the case of low-amplitude probing[29, 112]. A brief overview of the SID methods is presented below. For a thorough treatment, and implementation details, the reader is referred to Section 10.6 of [65].

Given a set of measurements, $\mathcal{S}$, of inputs, $U := [u(t)\,u(t-1)\,...\,u(0)]$, and observable outputs, $Y := [y(t)\,y(t-1)\,...\,y(0)]$, we seek to estimate a discrete-time $\hat{n}^{th}$-order state space model of the form in (5.9)

$$\hat{x}(t+1) = \hat{A}\hat{x}(t) + \hat{B}u(t) + \boldsymbol{w}(t) \tag{5.9a}$$

$$\hat{y}(t) = \hat{C}\hat{x}(t) + v(t) \tag{5.9b}$$

where $\hat{x} \in \mathbb{R}^{\hat{n}}$ is the state vector of the ROM, $u \in \mathbb{R}^k$ is the user-defined probe input, $\hat{y} \in \mathbb{R}^l$ is estimation of the observable output, y, w are Gaussian processes with zero mean and v are measurement noise.

We use this input-output data to construct the weighted extended observability matrix $\hat{G}$[65]. The order, $\hat{n}$, of the reduced-order model is then determined by looking at these singular values of $\hat{G}$, calculated by singular value decomposition. There exist numerous ways for determining the optimal order, $\hat{n}^\star$, from the singular values of $\hat{G}$. Within this work we use the singular value criterion (SVC) which has shown to result in consistent order estimation across various probing conditions[10]. The SVC minimization is shown in (5.10)

$$\min_n \quad SVC(n) = \sigma_{n+1}^2 + 2nl\frac{log(T)}{T} \tag{5.10}$$

where σ_i denotes the i^{th} largest singular value of $\hat{G}$, l is the dimensionality of y, and T denotes the number of sample data points. Once we have identified the dimensionality, $\hat{n}$, of the reduced order model, we can estimate the matrices A, B and C through simple least-square solutions as presented in [65]. Once a discrete-time state-space model has

been estimated, it can then be converted to a continuous-time model for controller design using a first- or zero-order hold method, depending on the probing control signal applied.

5.4 Method

Estimating a ROM

To build a ROM of the converter, and its dynamic coupling with the grid, we perturb the system using a low-amplitude probing signal to generate the input-output data. In this work, we introduce this probe into the system by modulating the reactive power set-point of the converter. [1] This is analogous to adjusting the voltage set-point of the AVR in a synchronous machine or the outer-control loop in a grid-forming converter. We choose the reactive power channel for our modulation signal for two reasons. First, by choosing to modulate the reactive power rather than the active power, we do not require coordinated control with the DC side, which simplifies the controller. Secondly, given that weak grid conditions have been identified as one of the primary causes of highly oscillatory behavior[21], adding a control signal into the reactive power controller can help stabilize the externally measured voltage during disturbances. The measured outputs we record for estimating the ROM are the local internal controller states of the converter. These inputs and outputs are shown in Fig. 5.2, where the superscript m denotes specific measurements/quantities.

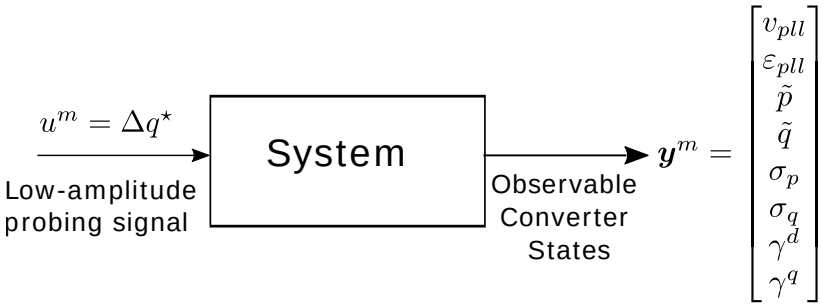

Figure 5.2: Probing the system with observable states

The probing signal we use is generated by taking the sign of a chirp signal in (5.11) with a frequency band $\Omega : \omega_1 \leq \omega \leq \omega_2$ over a certain time period $0 \leq t \leq M$, and scaling it by the probe amplitude, Γ. This frequency band, Ω :, can be determined based on offline analysis and/or based on real-world observed oscillatory behavior [21]. We then sample the output at a rate of 500 Hz. This sampling frequency is below the internal sampling frequency of the converter and does not require the use of an anti-aliasing filter, assuming oscillations of interest are less than 100 Hz (this was the case for the real-world observedCIG oscillations [21]).

[1] In this case the input, u, is a scalar and will be denoted by a non-bold lowercase letter moving forward.

$$u(t) = \Gamma.\text{sgn}\left(\sin\left(\omega_1 t + \frac{(\omega_2 - \omega_1)t^2}{2M}\right)\right) \tag{5.11}$$

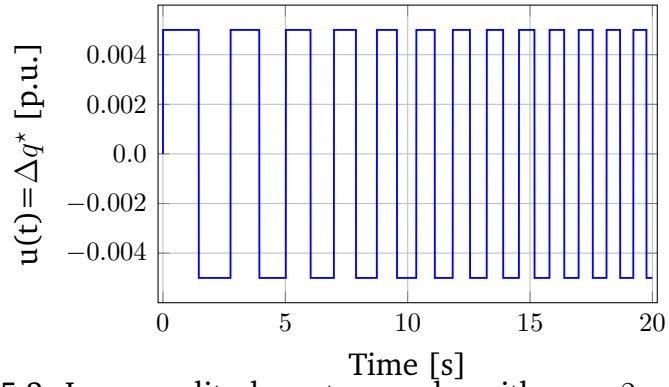

Figure 5.3: Low-amplitude system probe with $\omega_1 = 2$ and $\omega_2 = 6$

This deterministic probing signal has numerous advantages over both random white noise and sinusoidal signals for system identification[65]. One of these advantages, relative to random white noise, is the ability to perform repeated perturbing experiments and average the output over these experiments. This averaging attenuates the impact of measurement error and external disturbances, e.g., natural load variations and/or nearby controllers simultaneously perturbing the system. This helps ensure that the set of estimated modes are modes that the CIG participates in.

To average across multiple experiments, we must first remove signal offsets. We do this by assuming that, during each probing experiment, the system was in equilibrium about some operating point, $\bar{y}^m$, for a corresponding input $\bar{u}$, calculated by (5.12), where the superscript m denotes individual measurements. We then remove this offset in (5.13).

$$\bar{u} = \frac{1}{N}\sum_{t=1}^{N} u^m(t) \tag{5.12a}$$

$$\bar{y}_i^m = \frac{1}{N}\sum_{t=1}^{N} y_i^m(t) \quad \forall y_i^m \in y^m \tag{5.12b}$$

$$u(t) = u^m(t) - \bar{u} \qquad y(t) = y^m(t) - \bar{y}^m \tag{5.13}$$

Once we have removed these offsets, we can then average across K experiments, each of length M, by (5.14).

$$\bar{y}_i(t) = \frac{1}{K}\sum_{k=0}^{K-1} y_i(t + kM) \quad 1 \le t \le M \quad \forall y_i \in y \tag{5.14}$$

Once we have collected our set of experiment input data $U := [u(t),\, u(t-1) \ldots u(0)]$, and observable outputs, $Y := [\bar{y}(t),\, \bar{y}(t-1) \ldots \bar{y}(0)]$, we estimate a ROM using the approach described in Section 5.3. This estimation is performed using the Julia toolbox `ControlSystemIdentification.jl` [15].

Controller Design

Given a reduced-order model of the form in (5.9), we then want to design a damping controller to improve the damping of the model. We do this by placing a PSS in feedback with the reduced-order model, as shown in Fig. 5.4, and optimizing over its parameters. This controller, mathematically expressed in (5.15), is comprised of a stabilizing gain, k, followed by a wash-out filter to remove low-frequency behavior and any DC-offsets. Finally, a pair of lead-lag compensators are used to tune the phase response. The use of a double lead-lag compensators allows for phase compensation of more than 90 degrees. Commonly, the input to a PSS is a scalar quantity, e.g., the deviation in rotor speed [17]. In this work, however, we will give the PSS access to two controller states of the converter, namely $\tilde{q}$, the filtered reactive power and ε, the integrator state of the PLL. These states were chosen based on the discussion presented in [21] and offline participation factor analysis of theCIG against an infinite bus. The vector $k \in \mathbb{R}^8$ will then have two non-zero entries $k_{\tilde{q}}$ and k_{ε}, i.e., $k = [0 \ldots . k_{\tilde{q}} \ldots 0 \ldots k_{\varepsilon}]^T$.

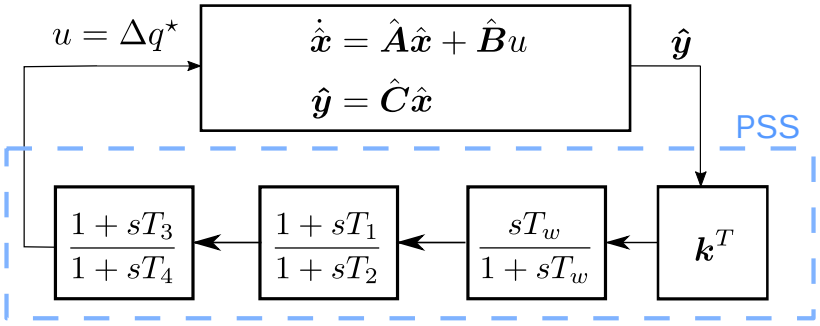

Figure 5.4: Placing a PSS in feedback with the ROM

$$\dot{v}_1 = -(k^T\hat{y} + v_1)/T_w \tag{5.15a}$$

$$\dot{v}_2 = ((1 - \frac{T_1}{T_2})(k^T\hat{y} + v_1) - v_2)/T_2 \tag{5.15b}$$

$$\dot{v}_3 = ((1 - \frac{T_3}{T_4})(v_2 + (\frac{T_1}{T_2}(k^T\hat{y} + v_1))) - v_3)/T_4 \tag{5.15c}$$

$$u = v_3 + \frac{T_3}{T_4}(v_2 + \frac{T_1}{T_2}(k^T\hat{y} + v_1)) \tag{5.15d}$$

Putting a PSS in feedback with our estimated ROM gives us a closed-loop system of the form in (5.16)

$$x_{cl} = A_{cl} x_{cl} \tag{5.16}$$

where

$$x_{cl} = \begin{bmatrix} \dot{\hat{x}} \\ \dot{x}_{pss} \end{bmatrix} \quad A_{cl} = \begin{bmatrix} \hat{A} + \hat{B} D_{pss} \hat{C} & \hat{B} C_{pss} \\ B_{pss} \hat{C} & A_{pss} \end{bmatrix} \tag{5.17}$$

The matrices A_{pss}, B_{pss}, C_{pss}, and D_{pss} come from expressing (5.15) in a state-space formulation. The goals of the state-feedback damping controller are: 1) to improve the damping of the modes of the closed-loop system in Fig. 5.4, whose damping coefficient is less than a specified critical threshold, ζ_c (see Fig. 5.5), and 2) to improve the stability of the reduced-order model by shifting the real parts of its eigenvalues further into the left-half plane. Given a pair of complex eigenvalues $\lambda_i = \sigma_i \pm j\omega_i$, their damping co-efficient, ζ_i, is given by (5.18).

$$\zeta_i = \frac{-\sigma_i}{\sqrt{\sigma_i^2 + \omega_i^2}} \tag{5.18}$$

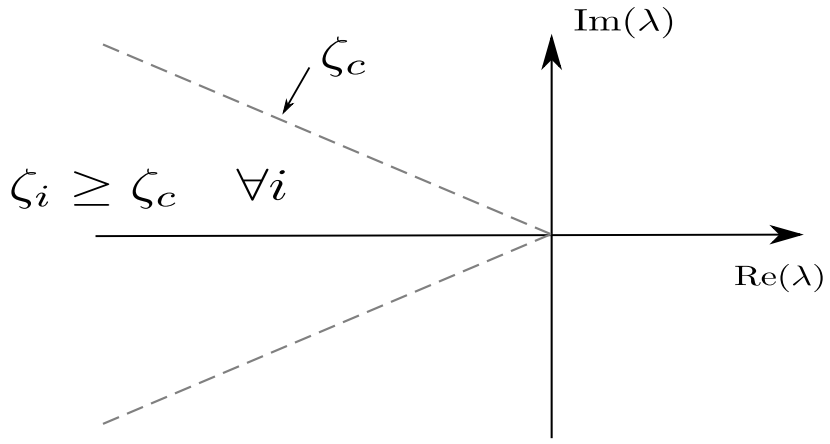

Figure 5.5: Critical damping co-efficient

This optimization of the parameters of the PSS in (5.15) is mathematically represented in (5.19) where $k = [0....k_{\tilde{q}} \dots 0 \dots k_{\varepsilon}]^T$, λ_i are the eigenvalues of the closed-loop system in (5.16), η is a normalization constant and β is a weighting factor to re-scale the damping coefficient.

$$\min_{\substack{k_{\tilde{q}}, k_{\varepsilon}, T_w, \\ T_1, T_2}} \quad \beta \sum_{\zeta_j \le \zeta_c} \alpha_j [\zeta_c - \zeta_j]^2 + \sum_{j=1}^{n} \alpha_j \, \mathrm{Re}(\lambda_j) \tag{5.19a}$$

$$
\begin{aligned}
s.t. \quad & A_{cl} v_i = \lambda_i v_i \quad \forall i && \text{(5.19b)}\\
& \mathrm{Re}(\lambda_i) < 0 \quad \forall i && \text{(5.19c)}\\
& k_{\tilde{q}}^{min} \leq k_{\tilde{q}} \leq k_{\tilde{q}}^{max} && \text{(5.19d)}\\
& k_{\varepsilon}^{min} \leq k_{\varepsilon} \leq k_{\varepsilon}^{max} && \text{(5.19e)}\\
& T_1^{min} \leq T_w \leq T_w^{max} && \text{(5.19f)}\\
& T_{1,2}^{min} \leq T_1 \leq T_{1,2}^{max} && \text{(5.19g)}\\
& T_{1,2}^{min} \leq T_2 \leq T_{1,2}^{max} && \text{(5.19h)}\\
& T_3 = T_1 && \text{(5.19i)}\\
& T_4 = T_2 && \text{(5.19j)}\\
& \alpha_j = \sum^{\{i | x_i \in \tilde{x}\}} p_{ij} && \text{(5.19k)}
\end{aligned}
$$

We solve the non-convex optimization problem in (5.19) using particle swarm optimization using the particle swarm optimization (PSO) hyper-parameters from [99] and parameter limits listed in Appendix 5.7. We weight each term in the objective in (5.19a) as a function of the total participation of the states of the reduced-order model in mode j, given by (5.19k). This weighting encourages the optimization formulation to focus on improving the damping and stability for the modes of the reduced order model rather than a trivial solution where the modes associated with the PSS have large negative real parts but have minimal effect on the modes of the reduced-order model.[2] After solving (5.19), the resultant PSS can be placed into operation and, as a final check, its performance can be validated by repeating the probing and confirming an improved dynamical response.

The output of PSS is a change in the reactive power set-point of theCIG plant that gets incorporated into the control loops by (5.20). This allows the proposed controller to operate independently of the DC-side controller and Periodic re-tuning of the PSS can be achieved by disabling the PSS and repeating the tuning presented in this paper. Alternatively, closed-loop identification offers a means for potentially re-tuning the controller without disabling the PSS [36]. Future work will examine this open question.

$$
i_f^{q\star} = k_{PQ}^{p}(q^{\star} + \Delta q^{\star} - \tilde{q}) + k_{PQ}^{i}\sigma_q \qquad \text{(5.20)}
$$

5.5 Results

We first present a detailed demonstration of the proposed approach on a three-bus system. This model contains a grid-following converter, from Section 5.2, a load and a synchronous machine. The generator is a Marconato model with a Type II AVR and a Type I turbine

[2]The constraint in (5.19c) can be modified to $Re(\lambda_i) < \epsilon$ where $\epsilon < 0$ is small. In this particular application, both formulations produced similar results.

governor [71]. We also model network dynamics, whose exclusion has been shown to have a significant effect on controller coupling dynamics [69],

Following this, we then demonstrate the approach on the IEEE 14 bus system with multiple CIG units simultaneously perturbing the system to build their own respective ROM. We also include random load perturbations. We show how, even in the presence of unknown and/or stochastic disturbances, our proposed approach improves the overall stability of the system. All simulations are carried out using `PowerSimulationsDynamics.jl` [58].

3 bus system

We excite the system, with ω_1=10 and ω_1=15, using the excitation signal in Fig 5.3 to obtain our input-output data. Fig. 5.6 shows the probe and a subset of the recorded states, $\tilde{p}$ and $\tilde{q}$, during the first 5 seconds of the experiment. Using all the recorded experiment data we build the extended observability matrix. The optimal model order, $n^\star$ is then determined by solving the optimization from (5.10). The value of this optimization, for varying model-orders, is shown in Fig. 5.7.

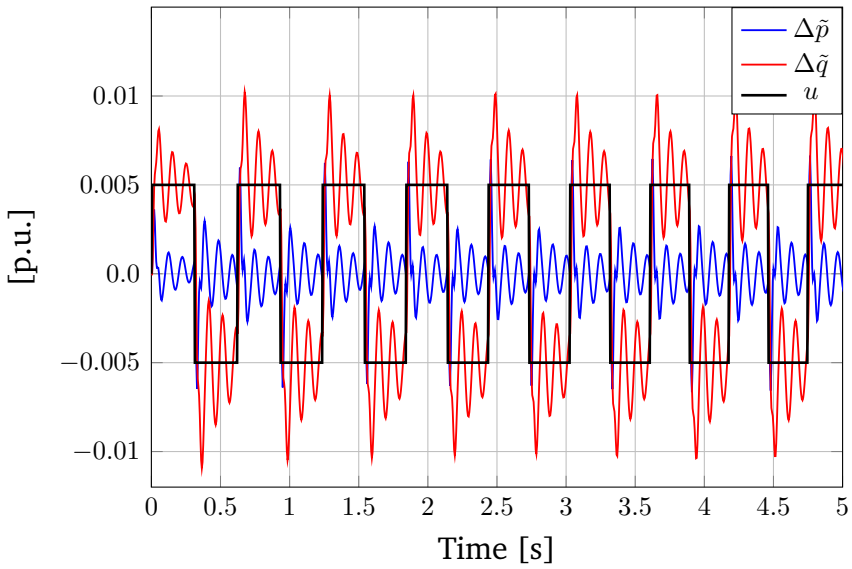

Figure 5.6: Probe input and subset of recorded controller states for the 3-bus case

In this case, the estimated optimal model order obtained from using the SVC method from [10] is 2. To understand this ROM, we compare the estimated modes of the ROM with those of the full-order model in Fig. 5.8. The color of each of the markers in Fig. 5.8 represent the summation of the participation of the converter states in that mode. For a 2^{nd}-order model, we see that the subspace identification method is able to accurately estimate the highly oscillatory mode in which the grid-following converter participates. There are modes in Fig. 5.8 very close to real axis that are not estimated by our ROM. These

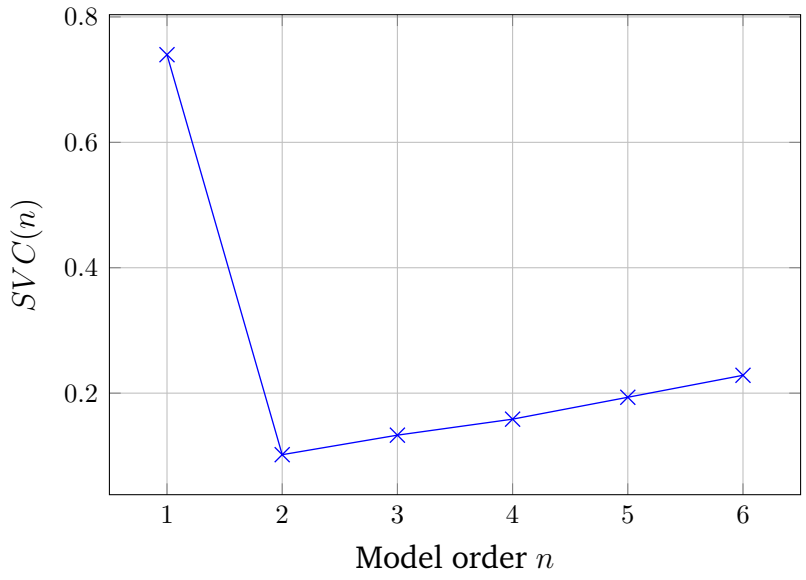

Figure 5.7: Determining the optimal order of the ROM for the CIG in the 3-bus case

Table 5.1: PSS Parameters for the 3 bus system

$k_{\tilde{q}}[p.u.]$	$k_{\varepsilon}[p.u.]$	T_w [s]	T_1 [s]	T_2 [s]
-0.5	-0.487	1.0	0.026	0.01

modes map to the integrator states of the inner-loop in (5.5a). Analysis shows that there was minimal excitation of these states by the probe employed because of good reference tracking by the PI control loop. Therefore, they were not identified as the *dominant* system modes by the subspace algorithm. In the event of oscillatory interactions among inner-loop controllers [106], this is expected to change as these modes become sufficiently excited to be included in the ROM.

After we have estimated a ROM, we then optimize the parameters of the PSS using (5.19). The resultant values are shown in Table 5.1.

To understand the performance of the proposed controller, we first look at the eigenspectrum of the linearized state-space model with and without the parameterized controller in Fig 5.9. We see that the proposed approach successfully improves the damping of the system by moving the pair of poorly-damped eigenvalues further into the left-half plane, and the damping of these modes improves from 0.06 to 0.2. Additionally, the tuned controller did not noticeably move any of the other system modes, shown in gray. Overall, the stability margin of the estimated modes are significantly improved by the inclusion of the proposed controller.

Next, we consider the time-domain response of the converter to a step-change in the

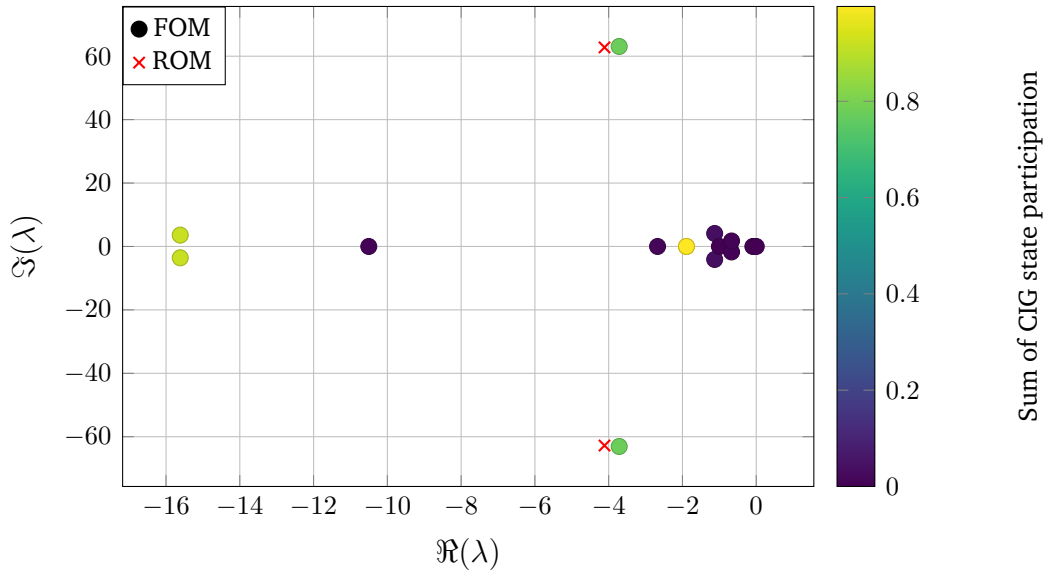

Figure 5.8: Zoomed-in eigenvalue spectrum of full- and reduced-order model for the 3-bus case

system load. Fig 5.10 show the active and reactive power injection from the converter respectively. For the case of active power, we see an initial spike response followed by a significantly smoother and better damped response as the stabilizing signal of the PSS takes effect. Similarly, the reactive power exhibits a much better damped response. After the initial spike, the reactive power is significantly more damped, and the amplitude of the first swing is reduced.

14 bus system

Next, we test the proposed controller on a modified version of the IEEE 14 bus system, shown in Fig. 5.11. We replaced the machines at bus 3 and bus 6 with grid-following CIG and re-distributed the generation across all generation sources on the network. On bus 6 we replaced one machine with two grid-following CIG to demonstrate the effectiveness of the approach even when two CIG units at the same bus have their probing periods partially overlap. Each CIG perturbs the network with the parameters in Table 5.5 and repeats its probing sequence 3 times. We then average over these experiments using (5.12) and (5.14) and each CIG independently builds a ROM with their own experiment input-output data. Using these estimated ROMs, each CIG then optimizes the parameters of its own damping controller using (5.19). The estimated model order and optimized PSS parameters for each CIG is shown in Table 5.2. In each case the estimated eigenvalues, and optimized PSS parameters, were similar. No information is shared among the converters or with any other devices on the system.

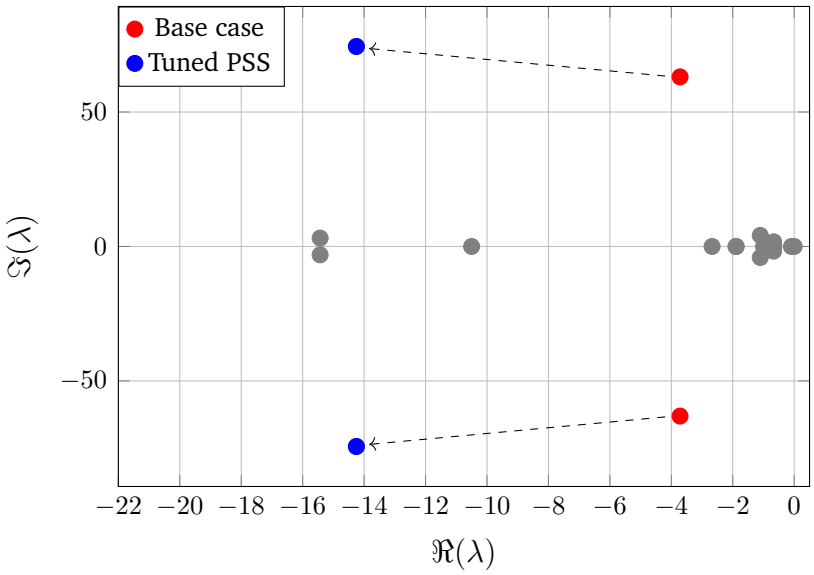

Figure 5.9: Effect of tuned controller on eigenvalues for the 3-bus system

Table 5.2: PSS Parameters for the 14 bus system

	$\hat{n}$	$k_{\tilde{q}}[p.u.]$	$k_{\varepsilon}[p.u.]$	T_w [s]	T_1 [s]	T_2 [s]
Gfl-3	2	-0.5	0.5	1.0	0.0247	0.01
Gfl-6a	2	-0.5	0.5	0.2	0.0249	0.01
Gfl-6b	2	-0.5	0.5	1.0	0.023	0.01

Fig. 5.12 shows the time-domain response of the three CIG units load step change at bus 13. For each CIG, we see a significant improvement in the dynamical response with a much shorter settling time. This shows that, for this case, there was no adverse interactions from each CIG independently parameterizing its own local damping controller.

In the case of the reactive power, in Fig. 5.13, we see a greater improvement in the dynamical response. In each case, the overshoot is reduced, and the settling time is greatly improved.

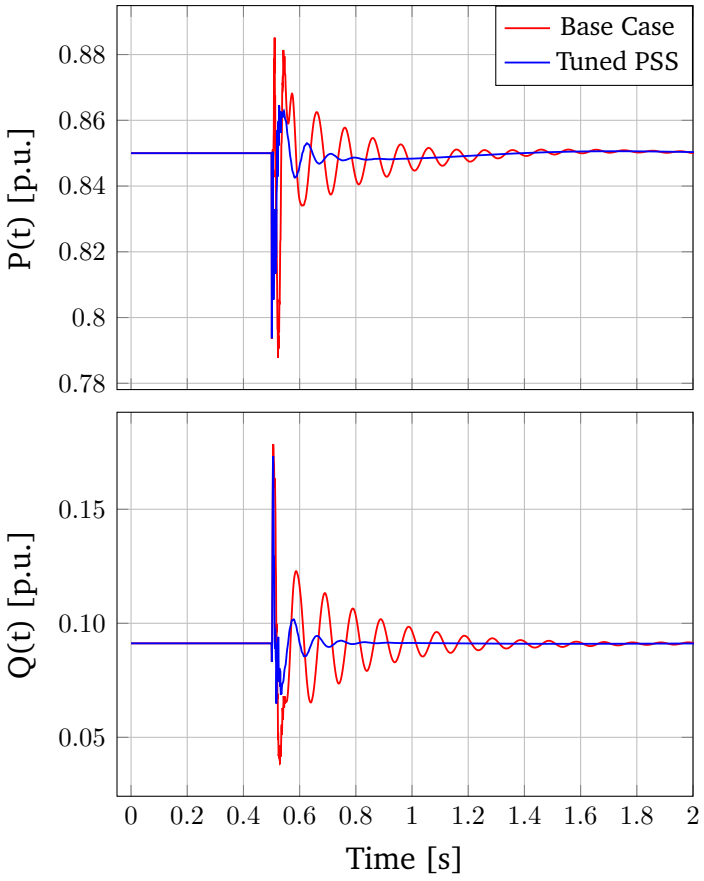

Figure 5.10: CIG active and reactive power for the 3-bus case following a load step change

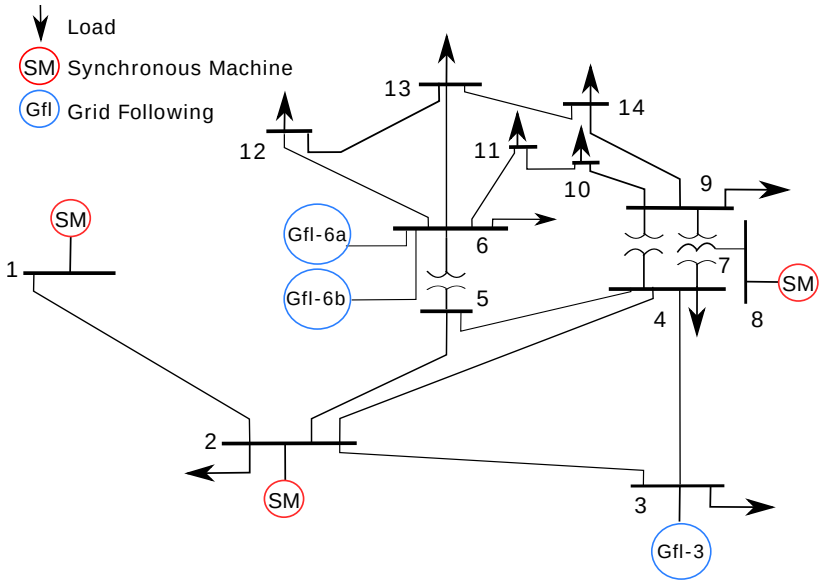

Figure 5.11: Modified 14 bus system

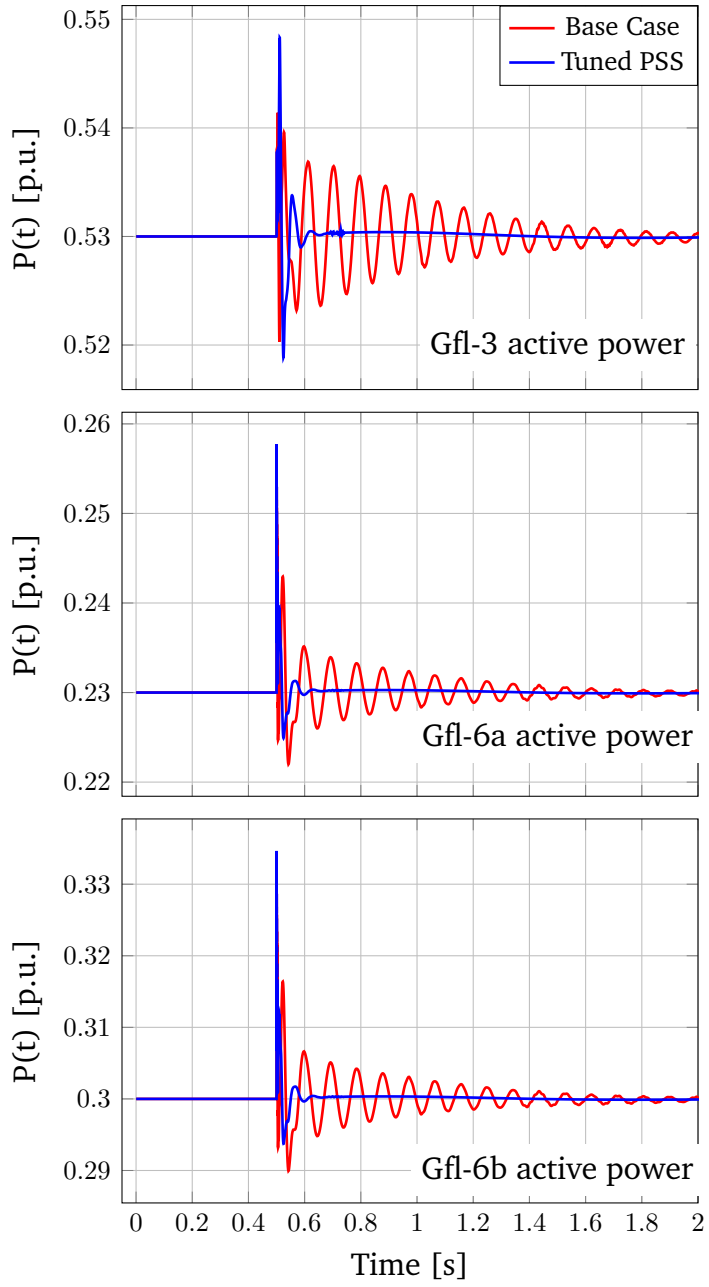

Figure 5.12: CIG active power response subject to disturbance for the 14-bus case

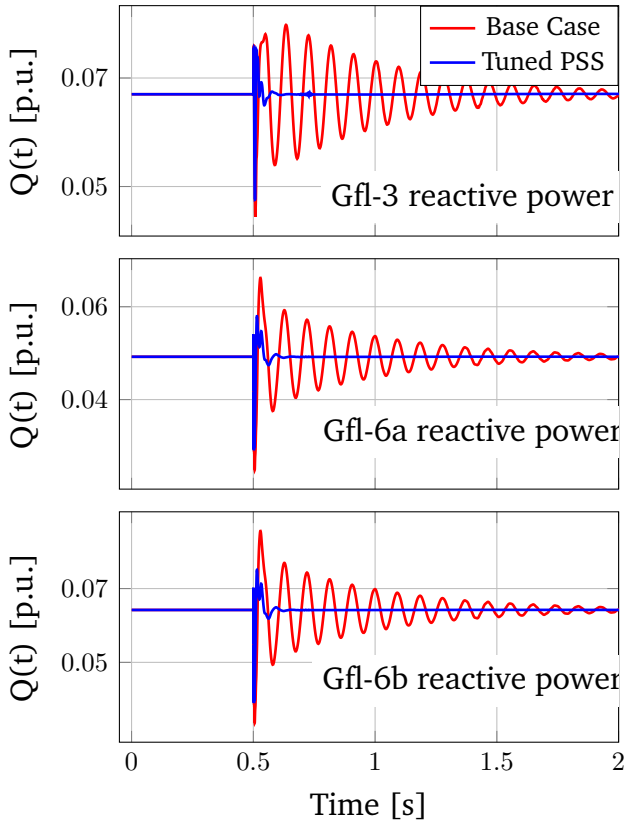

Figure 5.13: CIG reactive power response subject to disturbance for the 14-bus case

5.6 Conclusions

In this work, we presented a methodology for parameterizing a damping controller for grid-following CIG to improve the damping and stability margin of the system, particularly during weak grid conditions. We first demonstrated that, even for the case of simultaneous perturbations and/or ambient perturbation, each CIG was able to estimate a reduced-order dynamical model that captures its dominant dynamical interactions with the external grid. Following this, we developed an optimization formulation that incorporated participation factors to encourage the optimization algorithm to focus on moving the modes of the ROM, and consequently, improving the dynamical response when the controller was made operational in the physical system.

While the idea of a damping controller for CIG is itself not novel, the proposed approach of adaptively parameterizing such a controller using only locally observed states is. The proposed methodology requires no communication and can be carried out with low-amplitude probing. While this paper did consider the performance of the controller across various use cases, there is a significant amount of work to further understand these types of approaches.

Specifically, future work will include determining robust upper- and lower-limits for the parameters in (5.19) as well as a robust control approach where the uncertainty in the estimated reduced order model is explicitly considered. Additionally, the concept of closed-loop identifiability [36] will be considered as a means for re-parameterizing the damping controller for the case where the system may otherwise be unstable for open-loop probing as used in this paper. This is necessary as, after the PSS is parameterized, the system conditions may change such that the CIG would not be stable without the optimized PSS. Closed-loop identifiability allows us to re-probe the system without having to disable the PSS.

5.7 Appendix

Weighted Extended Observability Matrix

We define the vectors $y_r(t)$ and $u_r(t)$

$$y_r(t) = \begin{bmatrix} y(t) \\ y(t+1) \\ \vdots \\ y(t+r-1) \end{bmatrix} \quad u_r(t) = \begin{bmatrix} u(t) \\ u(t+1) \\ \vdots \\ u(t+r-1) \end{bmatrix} \tag{5.21}$$

where r is the prediction horizon, specified by the user. A larger value of r generally leads to better estimation performance[64].

Assuming we have input-output measurements for $t = 1, ..., N + r - 1$ we then define the matrices Y and U, using the notation from (5.21), in (5.22).

$$Y = [y_r(1) \quad y_r(2) \quad \dots y_r(N)] \tag{5.22a}$$
$$U = [u_r(1) \quad u_r(2) \quad \dots u_r(N)] \tag{5.22b}$$

We define the matrix $\Pi^{\perp}_{U^T}$ in (5.23). This matrix performs a projection onto the nullspace of U.

$$\Pi^{\perp}_{U^T} = I - U^T(UU^T)^{-1}U \tag{5.23}$$

Next we define the vector φ_s as (5.24)

$$\varphi_s(t) = \Big[y(t-1)\dots y(t-s_1)u(t-1)\dots u(t-s_2)\Big]^T \tag{5.24}$$

and the matrix Φ

$$\Phi = [\varphi_s(1) \quad \varphi_s(2) \quad \dots \quad \varphi_s(N)] \tag{5.25}$$

The weighted extended observabiltiy matrix is then given by

$$\hat{G} = \frac{1}{N} W_1 Y \Pi^{\perp}_{U^T} \Phi^T W_2 \tag{5.26}$$

with weighting matrices W_1 and W_2. In this work we use the MOESP weighting matrices[100].

$$\varphi_s(t) = \begin{bmatrix} y(t-1) \\ \vdots \\ y(t-s_1) \\ u(t-1) \\ \vdots \\ u(t-s_2) \end{bmatrix} \tag{5.27}$$

Experiment Parameters

Table 5.3: PSO Hyperparameters

Swarm size	ω	c1	c2
500	0.7298	1.49618	1.49618

Table 5.4: PSS Paramerter Values

$k_{\tilde{q}/\varepsilon}^{min}$	$k_{\tilde{q}/\varepsilon}^{max}$	T_w^{min}	T_w^{max}	$T_{1,2}^{min}$	$T_{1,2}^{max}$
-0.5	0.5	0.5	1.0	0.01	0.5

Table 5.5: IEEE 14 Bus Probe Parameters

	Γ [p.u.]	ω_1	ω_2	M [s]
Gfl-3	0.005	11.0	14.6	20
Gfl-3	0.005	10.6	13.9	20
Gfl-3	0.005	13.6	16.2	20

Chapter 6

Continuous-Time Echo State Networks for Predicting Power System Dynamics

This chapter was co-authored with Jose Daniel Lara and Rodrigo Henriquez-Auba, both PhD students at UC Berkeley at the time, Matthew Bossart, a PhD student at CU Boulder, Ranjan Anantharaman, then a PhD student at MIT, Chris Rackauckas, Director of Modeling and Simulation at Julia Computing, Bri-Mathias Hodge, chief scientist in the Distribution Edge Group in the Grid Planning and Analysis Center at NREL, and Prof. Duncan Callaway, Associate Professor of Energy and Resources at the University of California, Berkeley. The text was previously published in Electric Power Systems Research Journal (2022); see [86] for the full citation. The text has been reformatted for inclusion in this dissertation.

Abstract

With the growing penetration of converter-interfaced generation in power systems, the dynamical behavior of these systems is rapidly evolving. One of the challenges with converter-interfaced generation is the increased number of equations, as well as the required numerical timestep, involved in simulating these systems. Within this work, we explore the use of continuous-time echo state networks as a means to cheaply, and accurately, predict the dynamic response of power systems subject to a disturbance for varying system parameters. We show an application for predicting frequency dynamics following a loss of generation for varying penetrations of grid-following and grid-forming converters. We demonstrate that, after training on 20 solutions of the full-order system, we achieve a median nadir prediction error of 0.17 mHz with 95% of all nadir prediction errors within ± 4 mHz. We conclude with some discussion on how this approach can be used for parameter sensitivity analysis and within optimization algorithms to rapidly predict the dynamical behavior of the system.

6.1 Introduction

The increasing integration of CIG into large-scale synchronous power systems is forcing a re-examination of simulation practices to assess stability and reliability. Historically, large-scale power systems analysis was primarily focused on eletromechanical phenomena, arising from synchronous machines and their associated controls. However, the introduction of CIG, whose control loops act on the timescale of microseconds to milliseconds, is altering the dynamical behavior of power systems and is forcing examination of both electromagnetic and eletromechanical phenomena. These changes are leading to questions about the validity of several simplifications that have enabled computationally tractable large-scale system time domain simulations [42].

One of these key simplifications has been representing high-frequency dynamics, e.g., network dynamics, by either steady-state models or simplified dynamic models [42]. With increasing penetration of CIG, however, these simplifications have been shown to lead to incorrect conclusions about the small-signal stability of an operating point [69, 44] and/or lead to incorrect time-domain behavior following a disturbance [20]. This has led to some system operators recently introducing more stringent requirements for models of CIG to enable detailed electromagnetic studies [31].

These electromagnetic studies can be very computationally intensive, and potentially prohibitively time-consuming. The inclusion of both the dynamics of slow-acting synchronous machine and fast-acting CIG results in a *stiff* system. These systems require implicit differential equations solvers and, typically, very small simulation timesteps during a disturbance to accurately solve. This challenge in numerically solving the system is compounded by the increase in the number of equations to solve as large capacity synchronous generators are replaced by tens, or hundreds, of smaller capacity CIG plants. Therefore, not only are these systems computationally more expensive to simulate for a fixed number of differential equations, but the number of equations is also significantly larger, assuming all dynamics are modeled.

This paper explores the application of SciML to accelerate power systems simulations. SciML is a growing area of research that attempts to blend principles of scientific computing and machine learning [9]. One research area of SciML is computational acceleration using *surrogates*. A surrogate is an accurate approximation of the corresponding physics-based model trained using a data-driven approach. The training data come from recording the output of a full-order physics-based simulation across a subset of operating conditions. Once a surrogate has been trained to fit the training data, it can then be used in place of the full-order physics-based model. This reduces computational burden and can facilitate further analysis, e.g., sensitivity analysis or optimization.

The application of SciML techniques to model the dynamical behavior of power systems has been gaining interest in recent years, particularly the application of physics informed neural networks (PINNs) [72, 94]. In this paper, we will explore the application of continuous time echo-state networks (CTESNs) [4] for learning a surrogate to predict the time-domain solution of a power system for varying system parameters.

We begin with a discussion of the challenges that stiff systems present for some popular SciML surrogates, e.g., PINNs and long short-term memory (LSTM) networks. We then present a detailed introduction to CTESNs and how they bypass these stiffness-related challenges. Following this, we demonstrate an application for accelerating power system dynamic simulations through the use case of predicting frequency dynamics for varying compositions of CIG. We show that, after training on 20 solutions of the full-order system, we achieve a median nadir prediction error of 0.17 mHz with 95% of all nadir prediction errors within ± 4 mHz across the parameter space. Finally, we conclude with a discussion on the potential of CTESNs for power systems analysis and propose future research directions.

The main contributions of this paper are:

- An exploration of CTESNs as a new approach to accelerating parameter-sensitivity time domain simulations for power systems.
- An empirical examination of how the accuracy of CTESNs depends on the number of true solutions used during the training phase.
- An applied example where we use CTESNs to predict frequency dynamics following a large loss of generation with varying relative compositions of CIG (i.e., grid-forming vs grid-following).

6.2 Surrogates for Power System Simulation

The general process for training a surrogate is shown in Fig. 6.1. The parameter space of interest is sparsely sampled and the solution of the full-order model is obtained for each of these samples. These solutions form the training data from which the surrogate learns the parameter sensitivity of the solution. Once a surrogate has been trained, it can then be used to probe the parameter space at a much finer granularity with significantly less computational overhead, while maintaining a sufficient level of accuracy.

One surrogate model that has gained significant interest in recent years is a PINN [83]. A PINN is a continuous time function that predicts the solution of a physical system. Its loss function typically has two terms. The first of these terms penalizes the neural network for predicting values that do not match measured, or simulated, data. The second term in the loss function typically encodes known, or approximate, physical equations governing the behavior of the underlying physical system. An example of this in the context of power systems is penalizing the neural network for predicting voltage magnitudes and angles that do not satisfy the algebraic network power flow equations. PINNs have shown promise in predicting the solution of synchronous machines [94].

Another data-driven approach to learning the solution to a system of equations are LSTM networks. These neural networks are a type of recurrent neural network (RNN) where connections between nodes form a directed graph along a temporal sequence. This allows RNNs to learn to exhibit temporal dynamic behavior, and consequently, are suitable

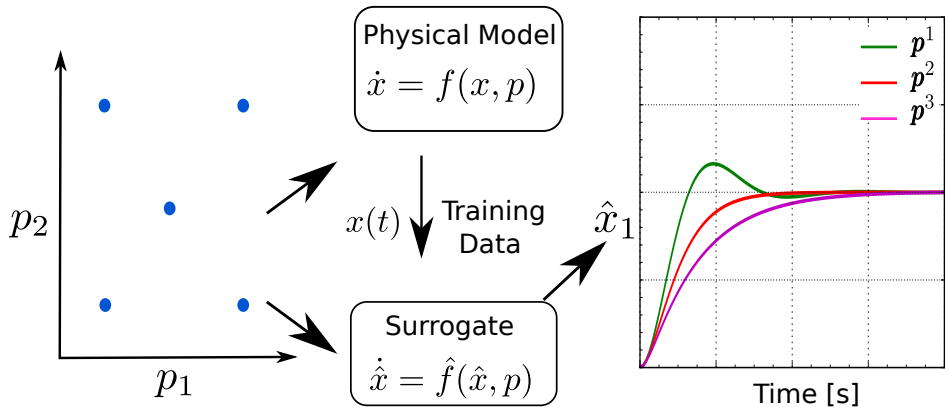

Figure 6.1: Surrogate for computational acceleration.

for learning the solution to a dynamical system. Like PINNs, LSTM networks have been successfully shown to be able to learn the solution of a synchronous machine [62, 94].

Both PINNs and LSTM networks have, however, been shown to be very difficult to fit to stiff systems [4, 105]. With the continual addition of CIG to our power systems, fast power system dynamics can no longer universally be well approximated by their steady-state algebraic equations [42]. Stiff systems are difficult for gradient-based surrogate training techniques for the same reason they are very difficult for explicit numerical solvers; they require a very small numerical step. For gradient-based optimization techniques, this numerical step is the learning rate of the optimizer.

CTESNs

Echo state networks (ESNs), like LSTM networks, are a type of RNN. However, they differ in that the weights of both the input matrix, $\boldsymbol{W}_{in}$, and the weights of the reservoir, $\boldsymbol{A}$, in (6.1) are randomly assigned and fixed throughout the training. Therefore, the *training* of an echo-state network (ESN) simplifies to learning the weights of the output layer, $\boldsymbol{W}_{out}$, in (6.2).

$$\boldsymbol{r}_{n+1} = f(\boldsymbol{A}\boldsymbol{r}_n + \boldsymbol{W}_{in}\boldsymbol{x}_n) \tag{6.1}$$

$$\hat{\boldsymbol{x}}_n = g(\boldsymbol{W}_{out}\boldsymbol{r}_n) \tag{6.2}$$

Typically the function $g(\cdot)$ is the identify function. The process for learning the weights of the readout layer then reduces to a least-squares problem, thereby, significantly simplifying the training of these networks. Consequently, ESNs avoid the challenges of gradient-based optimization for learning stiff systems. ESNs typically have a large recurrent layer, as shown in Fig 6.2, that results in a high-dimensional state space of rich dynamics. It is this wide spectrum of heterogeneous dynamics that allow ESNs to achieve excellent performance

in predicting time series behavior. ESNs have been used to predict chaotic systems [61], energy consumption and wind power generation [46].

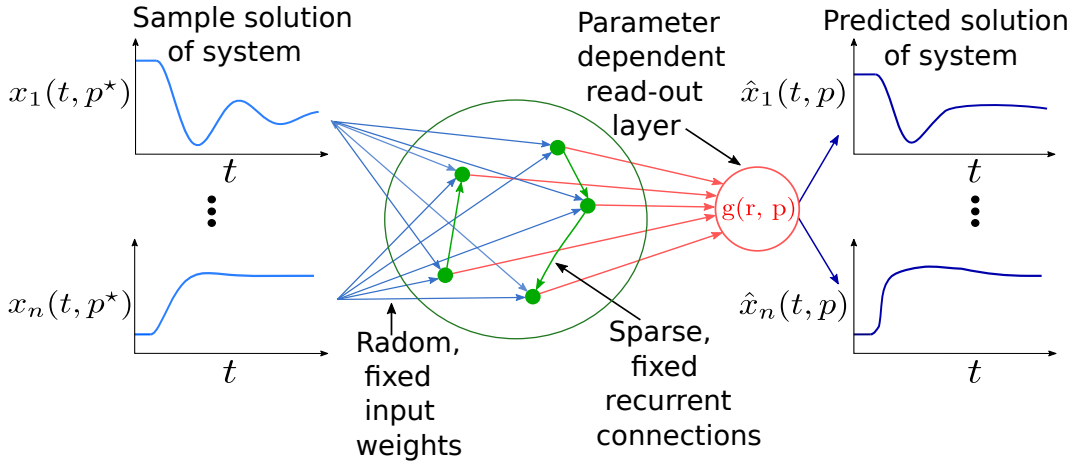

Figure 6.2: General structure of ESNs

Typically, ESNs are trained against fixed timestep interval data. This, however, can present challenges for learning stiff systems where a high number of samples may be required during disturbances to appropriately sample the fast dynamics. To overcome this issue, the authors in [4] proposed the use of CTESNs. These networks sample the true solution at the same non-uniform time intervals as was required to accurately solve the system using an adaptive implicit ODE solver.

To train a CTESN, we first begin with a sample solution of the true physical non-linear system that we term a *nominal* solution. We denote this nominal solution with parameters $\boldsymbol{p}^\star$, and pre-defined disturbance $w^\star$, as $\boldsymbol{x}(\boldsymbol{p}^\star, w^\star, t)$. We then use this nominal solution to drive the dynamics of the high dimensional reservoir

$$\dot{\boldsymbol{r}}(t) = f(\boldsymbol{A}\boldsymbol{r}(t) + \boldsymbol{W}_{in}\boldsymbol{x}(\boldsymbol{p}^\star, w^\star, t)) \tag{6.3}$$

where $\boldsymbol{A}$ is a fixed sparse random matrix $\in \mathbb{R}^{N\times N}$, $\boldsymbol{W}_{in}$ is a fixed dense random matrix $\in \mathbb{R}^{N\times M}$, $\boldsymbol{x}(\boldsymbol{p}^\star, w^\star, t) \in \mathbb{R}^M$ and $f(\cdot)$ is a non-linear function, e.g., $\tanh(\cdot)$. Because the reservoir in (6.3) is a non-stiff system, it is computationally cheap to simulate.

Once we have simulated the reservoir, we then want to learn a parameter-dependent mapping from this solution, $\boldsymbol{r}(t)$, to a predicted solution of the true system, $\hat{\boldsymbol{x}}(\boldsymbol{p}, w^\star, t)$. Typically, this is a linear-projection estimated by least squares. In our work however, we adopt a non-linear projection, the radial basis function (RBF), from [79]. radial basis functions (RBFs) are a method of interpolating unstructured data in high-dimensional spaces. The interpolant takes the form of a weighted sum of radial basis functions $\phi||.||$, e.g., Gaussian, linear or cubic, and frequently has some low order polynomials. Given n pairs of training data, $(\boldsymbol{x}, \boldsymbol{y})$, over which we fit an RBF, we estimate $\hat{\boldsymbol{y}}$ at a test datapoint, $\boldsymbol{x}^\star$, by (6.4)

$$\hat{\boldsymbol{y}} = \text{RBF}(\boldsymbol{x}^\star) = \sum_{i=1}^{n} \lambda_i \phi(||\boldsymbol{x}^\star - \boldsymbol{x}_i||) + \sum_{j=1}^{m} \gamma_j p_j(\boldsymbol{x}^\star) \tag{6.4}$$

where the weights $\boldsymbol{\lambda}$ and $\boldsymbol{\gamma}$ are learned during training. We use two RBF functions in this work. The first of these, rbf_β in (6.5a), takes as input the parameters we want to vary within our simulation, $\boldsymbol{p}$, and outputs a vector of weights, $\boldsymbol{\beta}(\boldsymbol{p})$. These weights then parameterize a second RBF, rbf_x in (6.5b), that maps from the pre-simulated reservoir, $\boldsymbol{r}(t)$, to the physical time series we want to predict, $\hat{\boldsymbol{x}}(t)$.

$$\boldsymbol{\beta}(\boldsymbol{p}) = \text{RBF}_\beta(\boldsymbol{p}) \tag{6.5a}$$

$$\hat{\boldsymbol{x}}(\boldsymbol{p}, w^\star, t) = \text{RBF}_x(\boldsymbol{\beta}(\boldsymbol{p}), \boldsymbol{r}(t)) \tag{6.5b}$$

We train this model by first sampling the boundary points of our multi-dimensional parameter space of interest. We then sample the remaining training points using Latin hypercube sampling, a low-discrepancy sequence, to generate a set of sample parameter vectors, $\boldsymbol{P} = [\boldsymbol{p}^1\, \boldsymbol{p}^2\, \ldots \boldsymbol{p}^n]$. Then, $\forall \boldsymbol{p}^i \in \boldsymbol{P}$, we simulate the full order model of the power system and calculate the parameter dependent rbf_x weights, $\boldsymbol{\beta}(\boldsymbol{p})$, that map the reservoir states, $\boldsymbol{r}(t)$, to states of the physical system, $\boldsymbol{x}(t)$. Once we have a set of training weights, $\boldsymbol{\beta}(\boldsymbol{p})$ $\forall \boldsymbol{p}^i \in \boldsymbol{P}$, we fit the radial basis function interpolation in (6.5a) to estimate these weights for parameters outside our training set. All RBF functions are fit using the Julia package `Surrogates.jl`[1].

After a CTESN has been trained, predicting system behavior for different parameters consists of a simple evaluation of (6.5a) to determine the parameter dependent weights, $\boldsymbol{\beta}(\boldsymbol{p})$, followed by a matrix multiplication of these weights by the precomputed interpolation matrix of rbf_x. The dominate operation in this workflow is a simple matrix multiplication that scales $\mathcal{O}(N)$. This is significantly cheaper that the cost of a general implicit ODE solver that generally scales up to $\mathcal{O}(N^3)$.

6.3 Methodology

The use case we consider within this work is predicting the frequency of the system following a large loss of generation for varying penetrations of both grid-following and grid-forming converters. The inclusion of these devices, and their relative penetrations, impacts key metrics of interest following large disturbances, e.g., the frequency nadir and rate of change of frequency (RoCoF).

Power System Models

The main power system considered for analysis is a modified version of the IEEE 14 bus system, shown in Fig 6.3. Generation capacity and active power set-points are adjusted to

[1] https://github.com/Surrogates.jl

distribute active power generation more evenly among the units. An additional thermal unit is added to bus two that provides 4% of the systems total active power generation. The disturbance considered for all experiments is a trip of this generating unit.

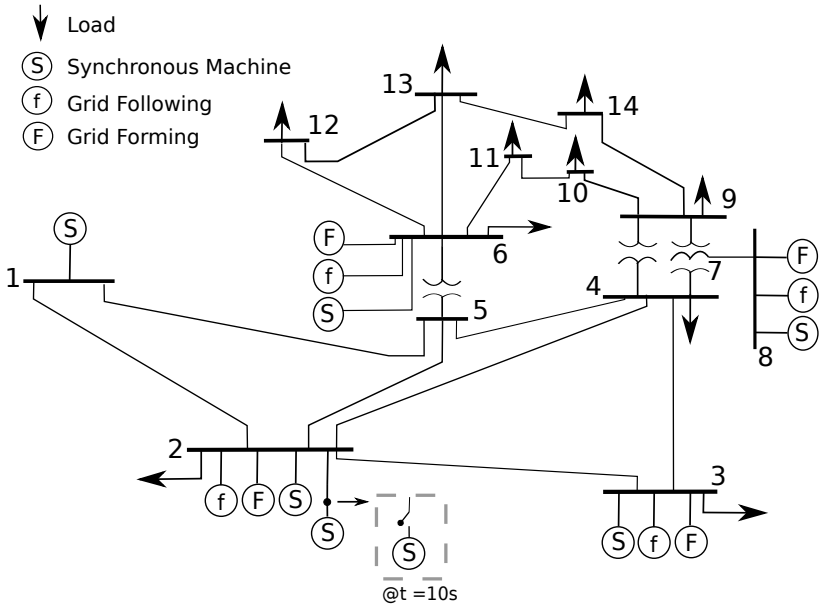

Figure 6.3: Modified IEEE 14 bus model.

To understand the impact of increasing penetration of CIG, we add both a grid-forming and grid-following converter to bus 2, 3, 6 and 8, as shown in Fig 6.3. All generation resources have an active power set-point of 0.8 p.u. with respect to their own capacity. For each simulation we change the penetration of CIG by changing the installed capacity for every generation resource on the network. Therefore, in addition to changing the active power injection from synchronous units, we also change the total system inertia for each simulation.

All synchronous machines are thermal units with a Type I turbine governor, with an active power droop of 5%, and a Type II AVR [71]. The grid-forming converters, from [69], are operating in droop mode, with an active droop of 5%. The grid-following inverters, taken from [53], are injecting fixed P and Q into the network and we model both network current dynamics and voltage dynamics for nodes with non-zero capacitance. This results in a system with $x \in \mathbb{R}^{243}$ with an associated stiffness ratio of the system on the order of 10^6.

Additionally, to demonstrate the scalability of the proposed approach, we will also examine how both the CTESN relative computation time and accuracy scale for increasing system size in Section 6.4. These systems are constructed by connecting copies of the IEEE-9 bus system. All simulations are carried out using the Julia package `PowerSimula-`

`tionDynamics.jl` [58, 59] using `Differentialequations. jl` [80] and all code for the experiments described here can be found at [33].

Training the CTESN

To generate training data, we simulate the network subject to a loss of generation at $t = 10$s. We vary the system operating conditions by changing 1) the % of generation that are CIG $\in [10,\ 80]$ and 2) the % of the CIG that are operating in grid-forming mode $\in [10,\ 40]$. The system is solved using the adaptive-stepping implicit IDA solver in Sundials [45]. The timesteps at which IDA solves the system determines the non-uniform sampling interval for training a CTESN. The input matrix, $\boldsymbol{W}_{in}$, is a random matrix whose entries are drawn from $x \sim \mathcal{N}(0, 1)$. The reservoir matrix, $\boldsymbol{A}$, is a Erdős–Renyi random graph with the total number of connections equaling the dimensional of the matrix. For rbf_x we use a linear RBF function while for rbf_β we use a cubic RBF function.

For this application, we train a CTESN to predict all line currents, nodal voltages for nodes with non-zero capacitance and the frequency of all synchronous machines on the network. To ensure that the reservoir is sufficiently excited by the solution of the true system, we normalize all state variables of the *nominal* solution, by subtracting their respective mean and dividing by the standard deviation, prior to feeding it as an input into the differential equations describing the evolution of the reservoir.

Within this work, we sample the parameter space and simulate the full-order physical system for the primary purpose of generate training data. In practice, depending on the application, the user/operator may follow such an approach. Alternatively, a CTESN can viewed as a valuable secondary use of the enormous amount of data that operators are generating daily through contingency analysis. In such cases, a CTESN can be trained in parallel until it is deemed to have met some accuracy requirements, from which time onward it can accelerate the exploration of contingencies.

6.4 Results

Accuracy of the Surrogate

We first begin by examining the accuracy of a CTESN. We sample from the parameter space using a Sobol sequence to generate a test size of 200. Fig. 6.4 shows a histogram of the errors between the true frequency nadir from the full-order system and the predicted frequency nadir from the CTESN for each individual test for different training sizes. In this context, training size refers to the number of time-domain solutions of the full-order we use for training the CTESN.

For the case of a training size of 20, 95% of all the errors are $\leq \pm$ 4 mHz. This empirical level of accuracy in Fig. 6.4 supports the idea that these surrogate approaches can be used to understand parameter sensitivities and/or within optimization algorithms to ensure

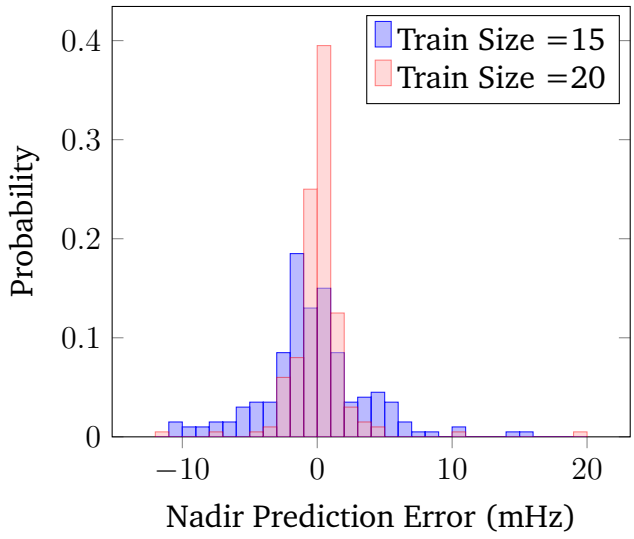

Figure 6.4: Empirical probability distribution of worse-case CTESN frequency nadir prediction error for varying training size.

satisfactory system frequency bounds. Furthermore, as previously noted, these training samples were randomly generated using Latin hypercube sampling. With more intelligent sampling of the parameters space there exists the possibility for equivalent, or improved, accuracy with reduced training samples.

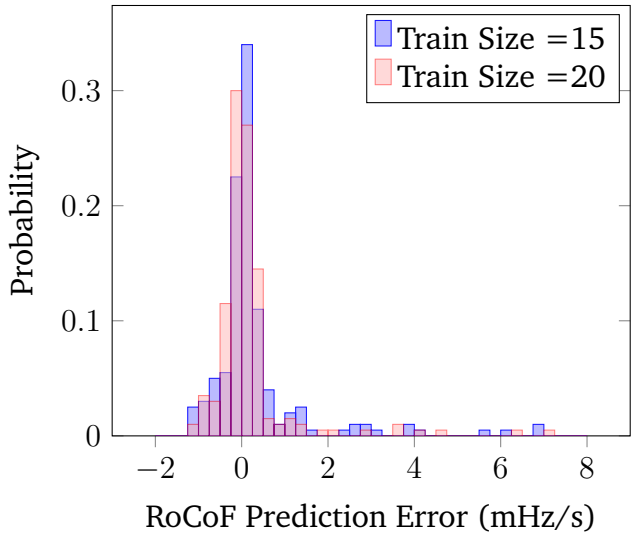

Figure 6.5: Empirical probability distribution of worse-case CTESN RoCoF prediction error for varying training size.

Another metric receiving increasing interest is the maximum RoCoF following a loss of generation. Fig. 6.5 shows a histogram of the errors between the largest negative RoCoF from the full-order system and the predicted largest negative RoCoF from the CTESN for each individual test. For both cases, the RoCoF was not a state variable but was estimated by calculating the maximum change in frequency over a time period of 0.1 s. Given this, the error distribution is less sensitive to training size, as expected.

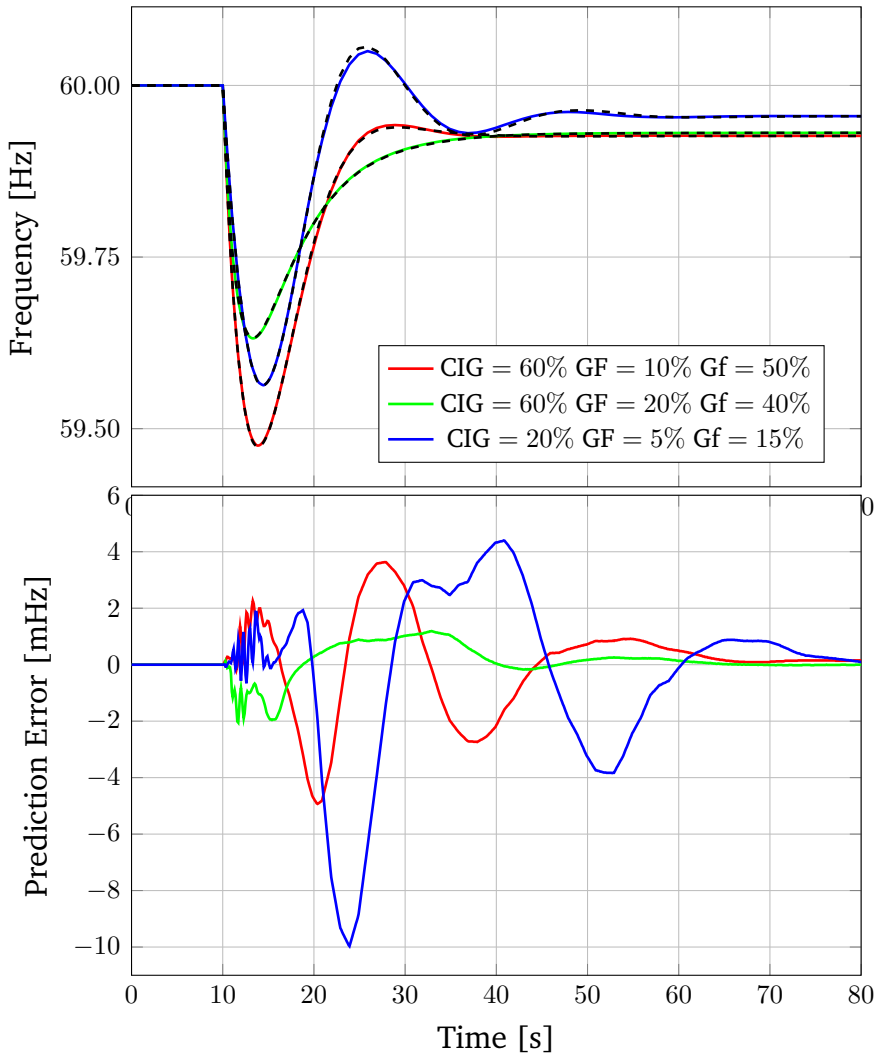

Figure 6.6: CTESN predicted frequency (solid lines) vs true solution (dashed black lines) and prediction error.

Fig. 6.6 compares three frequency traces from the synchronous machine at Bus 1 for three different generation composition mixes. In the first subplot, the CTESN predicted frequency traces are overlaid with the true solution, the dashed black line, and the prediction

error for each case is shown in the second subplot. Across all cases, the CTESN accurately predicts the dynamical behavior of the system, with a maximum prediction error of ≈ 10 mHz. This plot shows the capability of the CTESN to predict metrics such as the nadir and RoCoF, while also providing an estimation of the settling time and how damped the system response is.

Power System Dynamic Behavior

Once a CTESN is trained we can use it to rapidly predict the time series response for any parameter set within the upper- and lower-bounds specified during training. Fig. 6.7 shows the predicted frequency nadir by conducting a parameter sweep across the parameter range with a parameter granularity of 0.5%. This type of analysis can help system operators understand the required relative composition of grid-forming CIG to satisfy frequency containment requirements following the largest loss of generation. As expected, we see that for a fixed % of CIG, increasing the % of these resources that are grid-forming leads to a better frequency nadir.

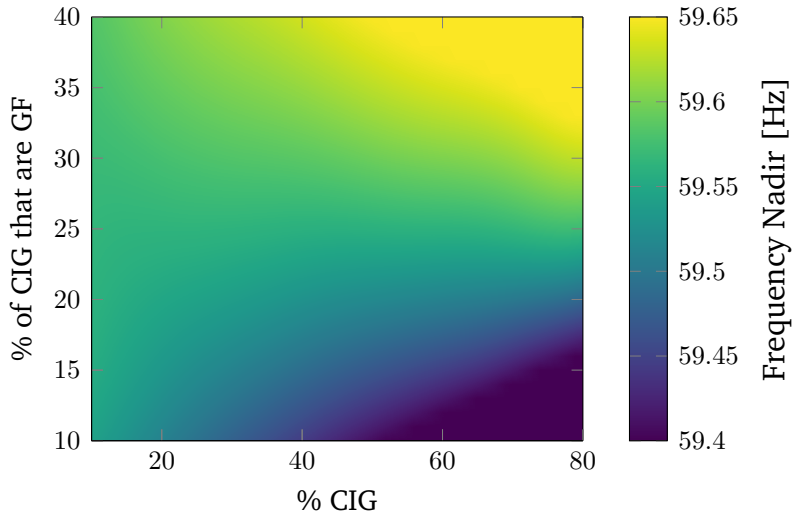

Figure 6.7: CTESN predicted frequency nadir.

Similarly, we can look at both the maximum RoCoF and frequency settling time, shown in Fig. 6.8 and Fig. 6.9 respectively, across the parameter range. We define the settling time as the time when the mean frequency across all machines enters, and stays within, a band of $\pm 20mHz$ Hz of its final settling frequency. We see in Fig. 6.9 that the % of CIG that is grid-forming has a significant impact on the frequency settling time.

To further examine how the response of the system changes we consider three distinct operating conditions, and their associated frequency dynamics, in Fig 6.6. We see that as we vary the % of CIG, the shape of the response can move from a 2^{nd}-order response to more

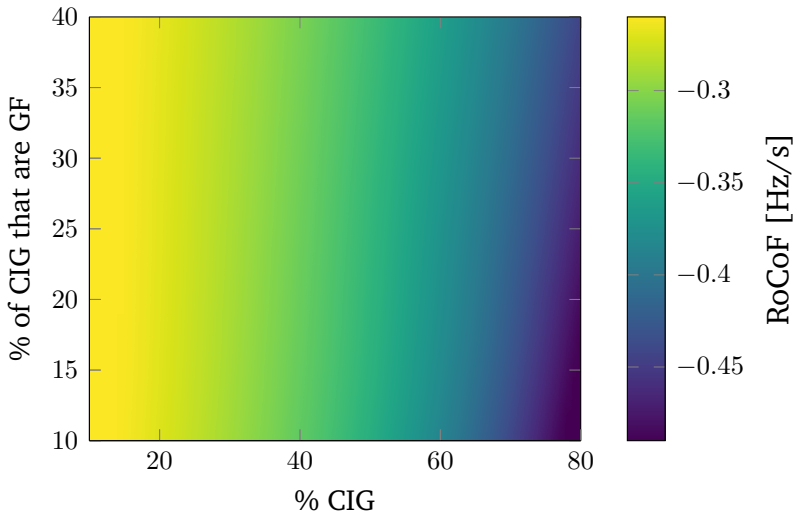

Figure 6.8: CTESN predicted largest RoCoF.

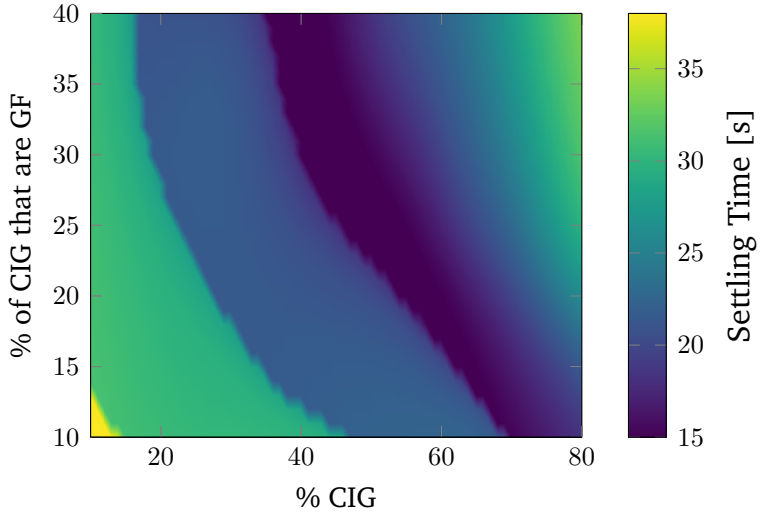

Figure 6.9: CTESN predicted frequency settling time.

of a 1^{st}-order response, in agreement with recent work [52]. Understanding the shifting behavior of the system with increased deployment of CIG will be critical for understanding and optimizing the deployment of these resources in large-scale networks.

Scalability and Computation Time

To benchmark the relative computation times, we consider systems of increasing sizes, all constructed using the WSCC 9-bus system as a modular building block and compare the computation time for both the CTESN and the full-order physical model. For each system size in Table 6.2, a CTESN was trained using 20 time-domain solutions of the full-order power system model with different CIG compositions. All computational benchmarking was carried out on a rack server with an Intel Xeon Processor E5-2623 v3.

Table 6.1 shows the total training time for each system. This time excludes the data generation, i.e., simulating the full-order physical model, as this is dependent on the specific simulation environment used, (e.g. PSCAD, etc). For a given training size, the primary factors influencing the training time are the number of time-steps required by the adaptive ODE solver to solve the system as well the number of variables that we want to predict. For larger systems, parallelization of components of the training process could reduce training times.

Table 6.1: CTESN Training Times

	18 Bus	36 Bus	72 Bus	144 Bus
Train Time [2]	52 s	186 s	201 s	626 s

The mean execution times, which included initializing and solving/predicting the time-domain solution across 20 simulations of each system, are shown in Table 6.2.

Table 6.2: Mean model execution times

System Size	CTESN	Full-order Model	Improvement ($\times$ times)
18 Bus	0.312 s	0.849 s	2.71
36 Bus	0.797 s	4.37 s	5.47
72 Bus	1.492 s	29.19 s	19.56
144 Bus	2.9 s	109.83 s	37.83

We see that, as expected, for increasing system size the computation acceleration achieved by the CTESN continues to improve. In each case the CTESN predicted the frequency of all synchronous machines, as well as nodal voltage with non-zero capacitance and line currents. Fig 6.10 shows a box plot of the CTESN prediction RMSE across 50 runs of the 144 Bus system, each for varying CIG penetration levels. For each prediction of the 144 Bus system, the CTESN is predicting a total of 467 state variables. Fig 6.10 shows that, even as we increase system size, the CTESN can predict all variables of interest with low error.

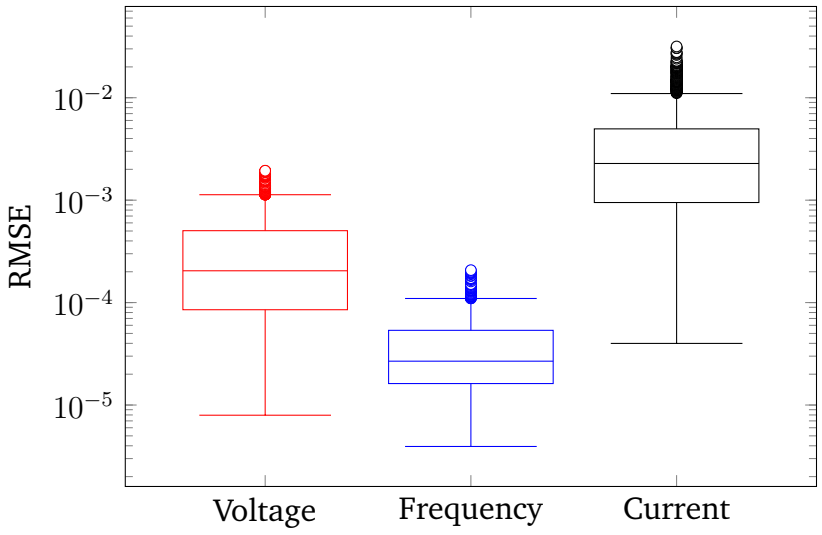

Figure 6.10: Box plot of prediction RMSE trained on 25 solutions for the 144 bus test case system.

6.5 Conclusions

This work examines the application of CTESNs for accelerating parameter sensitivity analysis for power system time domain simulations. The results suggest that there may be suitable candidate use cases for CTESNs, depending on the accuracy requirements in question. One avenue that the current implementation of CTESNs may open is rapid predictions of system dynamics subject to a pre-defined set of disturbances. This can allow for inclusion of frequency and/or voltage constraints within market optimization algorithms e.g., procuring reactive power support and/or frequency containment reserves. Furthermore, CTESNs can be used for planning purposes, e.g., understanding shifting system dynamics, and controller gain tuning. The ability to sparsely sample parameter spaces and build accurate approximate models can lead to more targeted exploration using the full-order model.

The use of CTESNs for developing surrogates for *stiff*-systems is a nascent area of research [4] and there is a significant amount of further work required to characterize the suitability of this approach for power system analysis. While the use case presented here was focused on learning the solution at the transmission grid level, there is no reason why CTESNs cannot be used for many other applications in power systems, e.g., for learning the solution of distribution systems and/or networked microgrids. Additionally, there is recent work that attempts to develop reusable component level surrogates based on CTESNs [5]. For power system applications, this could open further acceleration techniques beyond those presented within this paper. Most notably, this could include using surrogates as modular building blocks that can be mixed with physics-based models to understand the

response of the system to discontinuities not seen during the training phase, e.g., network topology changes and/or tripping of different resources.

Future works includes more intelligent sampling of the parameter space to minimize training requirements as well as exploring the idea of surrogates as modular building blocks for dynamical simulations. Additionally, some way of characterizing the accuracy of the surrogate, without the explicit use of a test set, would give users a greater confidence in integrating these surrogates into their workflow.

Chapter 7

Conclusion

This dissertation sought to develop new approaches for addressing the increased control and simulation complexity of systems with high penetration of IBRs. We showed how the stability and dynamical response of IBRs can be improved by the development of supplementary control loops that would not impede the current normal operation of these devices. Chapter 2 showed how, for the case of a cascaded PI inner-loop controller, we can neglect the DC-side dynamics without any loss in accuracy in capturing the interaction of the IBR with the grid. We also demonstrated that there is potential for a modest reduction in the required DC-side capacitor with the inclusion of a feedforwad predictive term.

In Chapter 3 and 4 we demonstrated how these multi-layered digital control loops that determine the dynamics of IBRs can increase the cyber-physical attack surface of these complex systems. We proposed an online adaptive controller that would introduce a minimal amount of stochastic behavior into the inverter control logic to break any adverse controller coupling, intentional or unintentional, through the network. Finally, on the topic of control, we demonstrated how we can use subspace identification to help periodically parameterize a power oscillation damping controller for IBRs in Chapter 5. The proposed method used repeated short duration low amplitude probing to excite the modes of interaction between the local grid and the IBR. This data is then used in controller design before, finally, the parameterized controllers are tested against the real system. This type of controller is not intended to replace rigorous offline engineering control development but rather improve the performance of these controllers should they experience unforeseen operating conditions.

Power system stability and control is a very exciting and active research right now with entirely new control strategies being proposed based on nonlinear phenomena such as coupled oscillators [49, 43, 91] and higher-order multi-input multi-output based grid-forming converters [18]. Additionally, understanding the system needs and where these advanced control functionalities are needed is a critical and open-area of research [78, 109].

In Chapter 6 we turned out attention to the issue of time-domain simulations. We showed how some emerging tools from the field of SciML can help provide a way to re-use

existing simulation data as well as identify regions of the parameter space that would be good candidates for further exploration. We find that the use of CTESNs can achieve $37\times$ acceleration of time-domain simulations for the test cases considered, with the relative acceleration increasing for large system sizes. This approach can be readily integrated into system operators workflows and help identify contingencies or operating conditions that need further investigation.

Future work will continue to focus on the use of SciML for accelerating power system time-domain simulations. Specifically, we are interested in developing ROMs that can capture the aggregate behavior of active distribution networks and/or parts of the transmission grid. We are working towards extensions of the work in Chapter 6 to develop composable dynamics models, similar to the work in other domains [5], that can open up more opportunities for computational acceleration for large-scale systems. We believe this work is critical as we see increasing controllability at the edge of the grid.

The field of SciML is a rapidly growing area of research with tools for learning differential equations describing the aggregate behavior of a set of heterogeneous dynamical devices [19, 81], solving partial differential equations [63], system identification [93] and other applications in power systems [104]. Continual research and development in this area is critical to continue to equip system operators with the tools they need to operate our power systems.

Bibliography

[1] *1,200 MW Fault Induced Solar Photovoltaic Resource Interruption Disturbance Report: Southern California 8/16/2016 Event*. Tech. rep. NERC, June 2017 (cit. on p. 3).

[2] Samrat Acharya, Yury Dvorkin, and Ramesh Karri. "Public Plug-in Electric Vehicles + Grid Data: Is a New Cyberattack Vector Viable?" In: *IEEE Transactions on Smart Grid* 11.6 (2020), pp. 5099–5113. DOI: 10.1109/TSG.2020.2994177 (cit. on pp. 21, 36, 38).

[3] Sajjad Amini, Fabio Pasqualetti, and Hamed Mohsenian-Rad. "Dynamic load altering attacks against power system stability: Attack models and protection schemes". In: *IEEE Transactions on Smart Grid* 9.4 (2016), pp. 2862–2872 (cit. on p. 21).

[4] Ranjan Anantharaman et al. "Accelerating Simulation of Stiff Nonlinear Systems using Continuous-Time Echo State Networks". In: *arXiv preprint arXiv:2010.04004* (2020) (cit. on pp. 75, 77, 78, 87).

[5] Ranjan Anantharaman et al. "Composable and Reusable Neural Surrogates to Predict System Response of Causal Model Components". In: *AAAI 2022 Workshop on AI for Design and Manufacturing (ADAM)*. 2021 (cit. on pp. 87, 90).

[6] AN Andry, EY Shapiro, and JC Chung. "Eigenstructure assignment for linear systems". In: *IEEE transactions on aerospace and electronic systems* 5 (1983), pp. 711–729 (cit. on pp. 23, 24).

[7] Saeed Arabi and Zhihong Feng. "Small-Signal Stability Study for ERCOT". In: *Powertech Labs Inc.(PLI), Report No.: PL-00323-5* (2014) (cit. on pp. 53, 54).

[8] Daniel Arnold et al. "Adaptive Control of Distributed Energy Resources for Distribution Grid Voltage Stability". In: *IEEE Transactions on Power Systems* (2022), pp. 1–1. DOI: 10.1109/TPWRS.2022.3157558 (cit. on pp. 37, 39).

[9] Nathan Baker et al. *Workshop report on basic research needs for scientific machine learning: Core technologies for artificial intelligence*. Tech. rep. USDOE Office of Science (SC), Washington, DC (United States), 2019 (cit. on p. 75).

[10] Dietmar Bauer. "Order estimation for subspace methods". In: *Automatica* 37.10 (2001), pp. 1561–1573 (cit. on pp. 57, 63).

[11] Damon Bazargan, Behrooz Bahrani, and Shaahin Filizadeh. "Reduced capacitance battery storage DC-link voltage regulation and dynamic improvement using a feed-forward control strategy". In: *IEEE Transactions on Energy Conversion* 33.4 (2018), pp. 1659–1668 (cit. on pp. 7, 8, 12, 13).

[12] Damon Bazargan, Shaahin Filizadeh, and Ani M Gole. "Stability analysis of converter-connected battery energy storage systems in the grid". In: *IEEE Transactions on Sustainable Energy* 5.4 (2014), pp. 1204–1212 (cit. on pp. 7, 8, 9, 12, 13, 14, 17).

[13] Nathaniel Bottrell, Milan Prodanovic, and Timothy C Green. "Dynamic stability of a microgrid with an active load". In: *IEEE Transactions on Power Electronics* 28.11 (2013), pp. 5107–5119 (cit. on pp. 25, 36).

[14] Hilary E. Brown and Christopher L. Demarco. "Risk of Cyber-Physical Attack via Load With Emulated Inertia Control". In: *IEEE Transactions on Smart Grid* 9.6 (2018), pp. 5854–5866. DOI: 10.1109/TSG.2017.2697823 (cit. on pp. 21, 28, 36, 38, 46).

[15] Fredrik Bagge Carlson. *ControlSystemIdentification*. original-date: 2019-01-25T11:54:06Z. May 2022. URL: https://github.com/baggepinnen/ControlSystemIdentification.jl (visited on 05/09/2022) (cit. on p. 60).

[16] Chen Chen, Jianhui Wang, Feng Qiu, and Dongbo Zhao. "Resilient distribution system by microgrids formation after natural disasters". In: *IEEE Transactions on Smart Grid* 7.2 (2015), pp. 958–966 (cit. on p. 7).

[17] Dong Chen, Yizhe Xu, and Alex Q Huang. "Integration of DC microgrids as virtual synchronous machines into the AC grid". In: *IEEE Transactions on Industrial Electronics* 64.9 (2017), pp. 7455–7466 (cit. on p. 60).

[18] Meng Chen, Dao Zhou, and Frede Blaabjerg. "Multivariable Grid-Forming Converters with Direct States Control". In: *2022 IEEE Energy Conversion Congress and Exposition (ECCE)*. IEEE. 2022, pp. 1–7 (cit. on p. 89).

[19] Ricky TQ Chen, Yulia Rubanova, Jesse Bettencourt, and David K Duvenaud. "Neural ordinary differential equations". In: *Advances in neural information processing systems* 31 (2018) (cit. on p. 90).

[20] Yunzhi Cheng et al. "ERCOT PSCAD Model Review Platform Development and Performance Comparison with PSS/e Model". In: *2020 IEEE Power & Energy Society General Meeting (PESGM)*. IEEE. 2020, pp. 1–5 (cit. on p. 75).

[21] Yunzhi Cheng et al. "Real-World Subsynchronous Oscillation Events in Power Grids with High Penetrations of Inverter-Based Resources". In: *IEEE Transactions on Power Systems* (2022), pp. 1–1. DOI: 10.1109/TPWRS.2022.3161418 (cit. on pp. 3, 36, 39, 41, 43, 53, 54, 58, 60).

[22] Julie A Cohn. *The grid: biography of an American technology*. MIT press, 2017 (cit. on p. 1).

[23] Salvatore D'Arco, Jon Are Suul, and Olav B Fosso. "Small-signal modelling and parametric sensitivity of a virtual synchronous machine". In: *2014 Power Systems Computation Conference*. IEEE. 2014, pp. 1–9 (cit. on pp. 10, 15, 17).

[24] Salvatore D'Arco, Jon Are Suul, and Olav B Fosso. "A Virtual Synchronous Machine implementation for distributed control of power converters in SmartGrids". In: *Electric Power Systems Research* 122 (2015), pp. 180–197 (cit. on p. 25).

[25] Salvatore D'Arco, Jon Are Suul, and Olav B Fosso. "Small-signal modeling and parametric sensitivity of a virtual synchronous machine in islanded operation". In: *International Journal of Electrical Power & Energy Systems* 72 (2015), pp. 3–15 (cit. on p. 7).

[26] C.L. DeMarco, J.V. Sariashkar, and F. Alvarado. "The potential for malicious control in a competitive power systems environment". In: *Proceeding of the 1996 IEEE International Conference on Control Applications IEEE International Conference on Control Applications held together with IEEE International Symposium on Intelligent Contro*. 1996, pp. 462–467. DOI: 10.1109/CCA.1996.558870 (cit. on p. 36).

[27] Christopher L DeMarco. "Design of predatory generation control in electric power systems". In: *Proceedings of the Thirty-First Hawaii International Conference on System Sciences*. Vol. 3. IEEE. 1998, pp. 32–38 (cit. on pp. 21, 22, 23, 28, 36, 38, 50).

[28] Christopher L DeMarco, JV Sariashkar, and Fernando Alvarado. "The potential for malicious control in a competitive power systems environment". In: *Proceeding of the 1996 IEEE International Conference on Control Applications IEEE International Conference on Control Applications held together with IEEE International Symposium on Intelligent Contro*. IEEE. 1996, pp. 462–467 (cit. on pp. 21, 28).

[29] Luke Dosiek et al. "Mode shape estimation algorithms under ambient conditions: A comparative review". In: *IEEE Transactions on Power Systems* 28.2 (2012), pp. 779–787 (cit. on p. 57).

[30] Mohammad Ebrahimi, S Ali Khajehoddin, and Masoud Karimi-Ghartemani. "An improved damping method for virtual synchronous machines". In: *IEEE Transactions on Sustainable Energy* 10.3 (2019), pp. 1491–1500 (cit. on p. 53).

[31] *Electromagnetic Transient Modeling Requirements*. Tech. rep. California ISO, Apr. 2021 (cit. on p. 75).

[32] Mohamed E Elkhatib, Wei Du, and Robert H Lasseter. "Evaluation of Inverter-based Grid Frequency Support using Frequency-Watt and Grid-Forming PV Inverters". In: *2018 IEEE Power & Energy Society General Meeting (PESGM)*. IEEE. 2018, pp. 1–5 (cit. on p. 7).

[33] Energy Modeling, Analysis and Control Group. Apr. 16, 2022. URL: https://github.com/Energy-MAC (cit. on p. 81).

[34] Lingling Fan. "Inter-IBR Oscillation Modes". In: *IEEE Transactions on Power Systems* 37.1 (2022), pp. 824–827. DOI: 10.1109/TPWRS.2021.3124667 (cit. on pp. 47, 53, 54, 56).

[35] Pablo Korth Pereira Ferraz, Robert Schmidt, Delf Kober, and Julia Kowal. "A high frequency model for predicting the behavior of lithium-ion batteries connected to fast switching power electronics". In: *Journal of Energy Storage* 18 (2018), pp. 40–49 (cit. on pp. 8, 13).

[36] Urban Forssell and Lennart Ljung. "Closed-loop identification revisited". In: *Automatica* 35.7 (1999), pp. 1215–1241 (cit. on pp. 62, 71).

[37] Bon-Gwan Gu and Kwanghee Nam. "A DC-link capacitor minimization method through direct capacitor current control". In: *IEEE Transactions on Industry Applications* 42.2 (2006), pp. 573–581 (cit. on p. 12).

[38] Eman Hammad et al. "A Class of Switching Exploits Based on Inter-Area Oscillations". In: *IEEE Transactions on Smart Grid* 9.5 (2018), pp. 4659–4668. DOI: 10.1109/TSG.2017.2666046 (cit. on pp. 21, 36, 38).

[39] Eman Hammad et al. "Tuning out of phase: Resonance attacks". In: *2015 IEEE International Conference on Smart Grid Communications (SmartGridComm)*. IEEE. 2015, pp. 491–496 (cit. on pp. 21, 36, 38).

[40] PJ Hart et al. "Modeling of second-life batteries for use in a CERTS microgrid". In: *2014 Power and Energy Conference at Illinois (PECI)*. IEEE. 2014, pp. 1–8 (cit. on pp. 13, 15, 17, 19).

[41] AMER Hasanovic, Ali Feliachi, NB Bhatt, and AG DeGroff. "Practical robust PSS design through identification of low-order transfer functions". In: *IEEE Transactions on Power systems* 19.3 (2004), pp. 1492–1500 (cit. on p. 56).

[42] Nikos Hatziargyriou et al. "Definition and Classification of Power System Stability – Revisited & Extended". In: *IEEE Transactions on Power Systems* 36.4 (2021), pp. 3271–3281. DOI: 10.1109/TPWRS.2020.3041774 (cit. on pp. 3, 4, 36, 53, 75, 77).

[43] Xiuqiang He, Verena Häberle, Irina Subotić, and Florian Dörfler. "Nonlinear Stability of Complex Droop Control in Converter-Based Power Systems". In: *IEEE Control Systems Letters* (2023) (cit. on p. 89).

[44] Rodrigo Henriquez-Auba, Jose D. Lara, Ciaran Roberts, and Duncan S. Callaway. "Grid Forming Inverter Small Signal Stability: Examining Role of Line and Voltage Dynamics". In: *IECON 2020 The 46th Annual Conference of the IEEE Industrial Electronics Society*. 2020, pp. 4063–4068. DOI: 10.1109/IECON43393.2020.9255030 (cit. on p. 75).

[45] Alan C Hindmarsh et al. "SUNDIALS: Suite of nonlinear and differential/algebraic equation solvers". In: *ACM Transactions on Mathematical Software (TOMS)* 31.3 (2005), pp. 363–396 (cit. on p. 81).

[46] Huanling Hu, Lin Wang, and Sheng-Xiang Lv. "Forecasting energy consumption and wind power generation using deep echo state network". In: *Renewable Energy* 154 (2020), pp. 598–613 (cit. on p. 78).

[47] P-H Huang and Y-Y Hsu. "Eigenstructure assignment in a longitudinal power system via excitation control". In: *IEEE transactions on Power Systems* 5.1 (1990), pp. 96–102 (cit. on p. 21).

[48] "IEEE Standard for Interconnection and Interoperability of Inverter-Based Resources (IBRs) Interconnecting with Associated Transmission Electric Power Systems". In: *IEEE Std 2800-2022* (2022), pp. 1–180. DOI: 10.1109/IEEESTD.2022.9762253 (cit. on pp. 3, 56).

[49] Brian B Johnson, Sairaj V Dhople, Abdullah O Hamadeh, and Philip T Krein. "Synchronization of parallel single-phase inverters with virtual oscillator control". In: *IEEE Transactions on Power Electronics* 29.11 (2013), pp. 6124–6138 (cit. on p. 89).

[50] I Kamwa, G Trudel, and L Gerin-Lajoie. "Low-order black-box models for control system design in large power systems". In: *Proceedings of Power Industry Computer Applications Conference*. IEEE. 1995, pp. 190–198 (cit. on p. 56).

[51] Innocent Kamwa and Luc Gerin-Lajoie. "State-space system identification-toward MIMO models for modal analysis and optimization of bulk power systems". In: *IEEE Transactions on Power Systems* 15.1 (2000), pp. 326–335 (cit. on p. 56).

[52] Rick Wallace Kenyon, Amirhossein Sajadi, and Bri-Mathias Hodge. "Frequency Dynamics with Grid Forming Inverters: A New Stability Paradigm". In: *arXiv preprint arXiv:2102.12332* (2021) (cit. on p. 85).

[53] Rick Wallace Kenyon, Amirhossein Sajadi, Andy Hoke, and Bri-Mathias Hodge. "Open-Source PSCAD Grid-Following and Grid-Forming Inverters and A Benchmark for Zero-Inertia Power System Simulations". In: *2021 IEEE Kansas Power and Energy Conference (KPEC)*. IEEE. 2021, pp. 1–6 (cit. on p. 80).

[54] Md Tanvir Arafat Khan, Aranya Chakrabortty, Iqbal Husain, and Rafael Cisneros. "Coordinated control of energy storage in networked microgrids under unpredicted load demands". In: *2019 American Control Conference (ACC)*. IEEE. 2019, pp. 1573–1578 (cit. on p. 7).

[55] Meir Klein, Graham J Rogers, and Prabha Kundur. "A fundamental study of inter-area oscillations in power systems". In: *IEEE Transactions on power systems* 6.3 (1991), pp. 914–921 (cit. on p. 53).

[56] Petar Kokotović, Hassan K Khalil, and John O'reilly. *Singular perturbation methods in control: analysis and design*. SIAM, 1999 (cit. on p. 2).

[57] Niraj Kshatriya, Udaya D Annakkage, F Michael Hughes, and Aniruddha M Gole. "Optimized partial eigenstructure assignment-based design of a combined PSS and active damping controller for a DFIG". In: *IEEE Transactions on Power Systems* 25.2 (2009), pp. 866–876 (cit. on p. 22).

[58] José Daniel Lara et al. *NREL-SIIP/PowerSimulationsDynamics.jl: v0.7.0*. Version v0.7.0. Sept. 2021. DOI: 10.5281/zenodo.5525487. URL: https://doi.org/10.5281/zenodo.5525487 (cit. on pp. 63, 81).

[59] José Daniel Lara et al. "PowerSystems.jl — A power system data management package for large scale modeling". In: *SoftwareX* 15 (July 2021). DOI: https://doi.org/10.1016/j.softx.2021.100747 (cit. on p. 81).

[60] Wook-Jin Lee and Seung-Ki Sul. "DC-link voltage stabilization for reduced DC-link capacitor inverter". In: *IEEE Transactions on Industry Applications* 50.1 (2013), pp. 404–414 (cit. on p. 7).

[61] Decai Li, Min Han, and Jun Wang. "Chaotic time series prediction based on a novel robust echo state network". In: *IEEE Transactions on Neural Networks and Learning Systems* 23.5 (2012), pp. 787–799 (cit. on p. 78).

[62] Jiaming Li, Meng Yue, Yue Zhao, and Guang Lin. "Machine-Learning-Based Online Transient Analysis via Iterative Computation of Generator Dynamics". In: *2020 IEEE International Conference on Communications, Control, and Computing Technologies for Smart Grids (SmartGridComm)*. IEEE. 2020, pp. 1–6 (cit. on p. 77).

[63] Zongyi Li et al. "Fourier neural operator for parametric partial differential equations". In: *arXiv preprint arXiv:2010.08895* (2020) (cit. on p. 90).

[64] Lennart Ljung. "Aspects and experiences of user choices in subspace identification methods". In: *IFAC Proceedings Volumes* 36.16 (2003), pp. 1765–1770 (cit. on p. 71).

[65] Lennart Ljung. "System identification". In: *Signal analysis and prediction*. Springer, 1998, pp. 163–173 (cit. on pp. 57, 59).

[66] U. Markovic, J. Vorwerk, P. Aristidou, and G. Hug. "Stability Analysis of Converter Control Modes in Low-Inertia Power Systems". In: *IEEE Innovative Smart Grid Technologies - Europe (ISGT-Europe)*. Oct. 2018 (cit. on pp. 10, 11, 25).

[67] Uros Markovic. "Towards reliable operation of converter-dominated power systems: Dynamics, optimization and control". en. PhD thesis. Zurich: ETH Zurich, 2020. DOI: 10.3929/ethz-b-000432013 (cit. on p. 45).

[68] Uros Markovic et al. "Understanding Small-Signal Stability of Low-Inertia Systems". In: *IEEE Transactions on Power Systems* 36.5 (2021), pp. 3997–4017. DOI: 10.1109/TPWRS.2021.3061434 (cit. on pp. 3, 7, 11, 25, 36).

[69] Uros Markovic et al. "Understanding Small-Signal Stability of Low-Inertia Systems". In: *IEEE Transactions on Power Systems* 36.5 (2021), pp. 3997–4017. DOI: 10.1109/TPWRS.2021.3061434 (cit. on pp. 63, 75, 80).

[70] Juan Manuel Mauricio and Andres E Leon. "Improving small-signal stability of power systems with significant converter-interfaced generation". In: *IEEE Transactions on Power Systems* 35.4 (2020), pp. 2904–2914 (cit. on p. 53).

[71] Federico Milano. *Power system modelling and scripting*. Springer Science & Business Media, 2010 (cit. on pp. 63, 80).

[72] George S. Misyris, Andreas Venzke, and Spyros Chatzivasileiadis. "Physics-Informed Neural Networks for Power Systems". In: *2020 IEEE Power & Energy Society General Meeting (PESGM)*. 2020, pp. 1–5. DOI: 10.1109/PESGM41954.2020.9282004 (cit. on p. 75).

[73] B. Moore. "On the flexibility offered by state feedback in multivariable systems beyond closed loop eigenvalue assignment". In: *IEEE Transactions on Automatic Control* 21.5 (1976), pp. 689–692. DOI: 10.1109/TAC.1976.1101355 (cit. on pp. 34, 51).

[74] R. Ofir, U. Markovic, P. Aristidou, and G.Hug. "Droop vs. Virtual Inertia: Comparison from the Perspective of Converter Operation Mode". In: *IEEE International Energy Conference (ENERGYCON)*. June 2018 (cit. on pp. 10, 11).

[75] Hugo N Villegas Pico and Brian B Johnson. "Transient stability assessment of multi-machine multi-converter power systems". In: *IEEE Transactions on Power Systems* 34.5 (2019), pp. 3504–3514 (cit. on p. 15).

[76] Yousef Pipelzadeh, Nilanjan Ray Chaudhuri, Balarko Chaudhuri, and Tim C Green. "Coordinated control of offshore wind farm and onshore HVDC converter for effective power oscillation damping". In: *IEEE Transactions on Power Systems* 32.3 (2016), pp. 1860–1872 (cit. on p. 53).

[77] Nagaraju Pogaku, Milan Prodanovic, and Timothy C Green. "Modeling, analysis and testing of autonomous operation of an inverter-based microgrid". In: *IEEE Transactions on power electronics* 22.2 (2007), pp. 613–625 (cit. on p. 25).

[78] Bala Kameshwar Poolla, Dominic Groß, and Florian Dörfler. "Placement and implementation of grid-forming and grid-following virtual inertia and fast frequency response". In: *IEEE Transactions on Power Systems* 34.4 (2019), pp. 3035–3046 (cit. on p. 89).

[79] Chris Rackauckas et al. "Composing Modeling and Simulation with Machine Learning in Julia". In: *arXiv preprint arXiv:2105.05946* (2021) (cit. on p. 78).

[80] Christopher Rackauckas and Qing Nie. "Differentialequations.jl–a performant and feature-rich ecosystem for solving differential equations in julia". In: *Journal of Open Research Software* 5.1 (2017) (cit. on p. 81).

[81] Christopher Rackauckas et al. "Universal differential equations for scientific machine learning". In: *arXiv preprint arXiv:2001.04385* (2020) (cit. on p. 90).

[82] Ahmad Rahmoun et al. "Mathematical modeling and dynamic behavior of a Lithium-Ion battery system for microgrid application". In: *2016 IEEE International Energy Conference (ENERGYCON)*. IEEE. 2016, pp. 1–6 (cit. on pp. 13, 15, 19).

[83] Maziar Raissi, Paris Perdikaris, and George E Karniadakis. "Physics-informed neural networks: A deep learning framework for solving forward and inverse problems involving nonlinear partial differential equations". In: *Journal of Computational Physics* 378 (2019), pp. 686–707 (cit. on p. 76).

[84] Ciaran Roberts, Duncan Callaway, and Daniel Arnold. "Outer-loop Adaptive Control of Converter-Interfaced Generation for Cyber-Physical Security". In: (2023) (cit. on p. 35).

[85] Ciaran Roberts, Uros Markovic, Daniel Arnold, and Duncan S. Callaway. "Malicious Control of an Active Load in an Islanded Mixed-Source Microgrid". In: *2021 IEEE Madrid PowerTech*. 2021, pp. 1–6. DOI: 10.1109/PowerTech46648.2021.9495077 (cit. on pp. 20, 36, 37, 38, 39, 45).

[86] Ciaran Roberts et al. "Continuous-time echo state networks for predicting power system dynamics". In: *Electric Power Systems Research* 212 (2022), p. 108562 (cit. on p. 74).

[87] Ciaran Roberts et al. "Grid-coupled dynamic response of battery-driven voltage source converters". In: *2020 IEEE international conference on communications, control, and computing technologies for smart grids (SmartGridComm)*. IEEE. 2020, pp. 1–6 (cit. on p. 6).

[88] Graham Rogers. *Power system oscillations*. Springer Science & Business Media, 2012 (cit. on p. 53).

[89] Subham Sahoo, Tomislav Dragičević, and Frede Blaabjerg. "Cyber Security in Control of Grid-Tied Power Electronic Converters—Challenges and Vulnerabilities". In: *IEEE Journal of Emerging and Selected Topics in Power Electronics* 9.5 (2021), pp. 5326–5340. DOI: 10.1109/JESTPE.2019.2953480 (cit. on pp. 36, 49).

[90] Peter W Sauer and Mangalore Anantha Pai. *Power system dynamics and stability*. Vol. 101. Wiley Online Library, 1998 (cit. on pp. 22, 57).

[91] Gab-Su Seo et al. "Dispatchable virtual oscillator control for decentralized inverter-dominated power systems: Analysis and experiments". In: *2019 IEEE Applied Power Electronics Conference and Exposition (APEC)*. IEEE. 2019, pp. 561–566 (cit. on p. 89).

[92] Jan Shair et al. "Adaptive damping control of subsynchronous oscillation in DFIG-based wind farms connected to series-compensated network". In: *IEEE Transactions on Power Delivery* (2021) (cit. on p. 53).

[93] Simon Stock et al. "Bayesian Physics-Informed Neural Networks for Robust System Identification of Power Systems". In: *arXiv preprint arXiv:2212.11911* (2022) (cit. on p. 90).

[94] Nikolay Stulov et al. "Learning model of generator from terminal data". In: *Electric Power Systems Research* 189 (2020), p. 106742 (cit. on pp. 75, 76, 77).

[95] Ke Tang and Ganesh K Venayagamoorthy. "Damping inter-area oscillations using virtual generator based power system stabilizer". In: *Electric Power Systems Research* 129 (2015), pp. 126–141 (cit. on p. 53).

[96] Ekaterina Telegina. "Impact of rotational inertia changes on power system stability". In: *MSc., Swiss Federal Institute of Technology, Zurich* (2015) (cit. on p. 25).

[97] Masatoshi Uno and Koji Tanaka. "Influence of high-frequency charge–discharge cycling induced by cell voltage equalizers on the life performance of lithium-ion cells". In: *IEEE Transactions on Vehicular Technology* 60.4 (2011), pp. 1505–1515 (cit. on p. 13).

[98] Lukas Unruh, Anuradha Kariyawasam, Suren Dadallage, and Andrew Isaacs. *Hawaiian Electric Island-Wide PSCAD Studies (Stage 2 System Impact Study)*. Tech. rep. Electranix, June 2021 (cit. on p. 3).

[99] Frans Van den Bergh and Andries P Engelbrecht. "A study of particle swarm optimization particle trajectories". In: *Information sciences* 176.8 (2006), pp. 937–971 (cit. on p. 62).

[100] Michel Verhaegen. "Identification of the deterministic part of MIMO state space models given in innovations form from input-output data". In: *Automatica* 30.1 (1994), pp. 61–74 (cit. on p. 72).

[101] Wladislaw Waag, Stefan Käbitz, and Dirk Uwe Sauer. "Experimental investigation of the lithium-ion battery impedance characteristic at various conditions and aging states and its influence on the application". In: *Applied Energy* 102 (2013), pp. 885–897 (cit. on p. 13).

[102] Chengshan Wang, Xialin Li, Li Guo, and Yun Wei Li. "A nonlinear-disturbance-observer-based DC-bus voltage control for a hybrid AC/DC microgrid". In: *IEEE Transactions on Power Electronics* 29.11 (2014), pp. 6162–6177 (cit. on p. 14).

[103] Huai Wang, Marco Liserre, and Frede Blaabjerg. "Toward reliable power electronics: Challenges, design tools, and opportunities". In: *IEEE Industrial Electronics Magazine* 7.2 (2013), pp. 17–26 (cit. on p. 7).

[104] Jiawei Wang et al. "On machine learning-based techniques for future sustainable and resilient energy systems". In: *IEEE Transactions on Sustainable Energy* (2022) (cit. on p. 90).

[105] Sifan Wang, Yujun Teng, and Paris Perdikaris. "Understanding and mitigating gradient pathologies in physics-informed neural networks". In: *arXiv preprint arXiv:2001.04536* (2020) (cit. on p. 77).

[106] Xiongfei Wang, Frede Blaabjerg, and Weimin Wu. "Modeling and analysis of harmonic stability in an AC power-electronics-based power system". In: *IEEE Transactions on Power Electronics* 29.12 (2014), pp. 6421–6432 (cit. on p. 64).

[107] Xiongfei Wang, Yun Wei Li, Frede Blaabjerg, and Poh Chiang Loh. "Virtual-Impedance-Based Control for Voltage-Source and Current-Source Converters". In: *IEEE Transactions on Power Electronics* 30.12 (2015), pp. 7019–7037. DOI: 10.1109/TPEL.2014.2382565 (cit. on p. 44).

[108] Yongdong Wu et al. "Resonance attacks on load frequency control of smart grids". In: *IEEE Transactions on Smart Grid* 9.5 (2017), pp. 4490–4502 (cit. on pp. 21, 36).

[109] Chaoran Yang, Linbin Huang, Huanhai Xin, and Ping Ju. "Placing grid-forming converters to enhance small signal stability of PLL-integrated power systems". In: *IEEE Transactions on Power Systems* 36.4 (2020), pp. 3563–3573 (cit. on p. 89).

[110] Shaoyong Yang et al. "An industry-based survey of reliability in power electronic converters". In: *IEEE transactions on Industry Applications* 47.3 (2011), pp. 1441–1451 (cit. on pp. 7, 16).

[111] Amirnaser Yazdani and Reza Iravani. *Voltage-sourced converters in power systems: modeling, control, and applications*. John Wiley & Sons, 2010 (cit. on p. 14).

[112] Junbo Zhang, Chao Lu, and Yingduo Han. "MIMO identification of power system with low level probing tests: Applicability comparison of subspace methods". In: *IEEE Transactions on Power Systems* 28.3 (2013), pp. 2907–2917 (cit. on p. 57).

[113] Lingyin Zhao and Jinrong Qian. "DC-DC power conversions and system design considerations for battery operated system". In: *Texas Instruments* (2006) (cit. on p. 13).